National Technical University of Athens
School of Mechanical Engineering
Sector of Fluid Mechanics

"Simulation of sound propagation in the atmosphere using the Parabolic Equation method and application to the prediction of wind turbine noise"

A Master's Thesis by
Christine Kappatou

Supervised by
Vasilis. A. Riziotis (Associate Professor)

Co-supervised by
John. M. Prospathopoulos (Teaching and Research Associate)

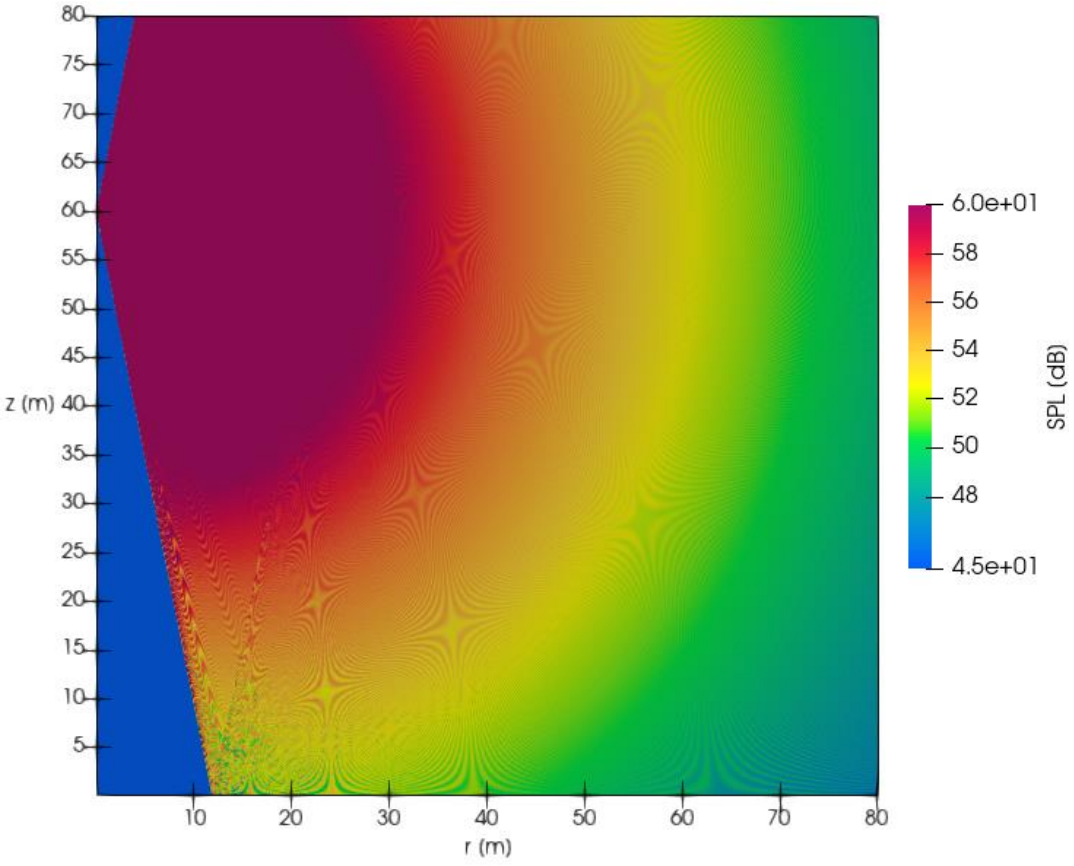

Athens

October 2021

Special Thanks to:

Teaching and Research Associate *Dr. John. M. Prospathopoulos* for the constant guidance, consulting and patience and, generally, for *being there*. I cannot imagine completing this study without his help and I consider it as a product of collaborative work.

Associate Professor *Vasilis. A. Riziotis* for bringing into my attention the work of Dr. Prospathopoulos and for devoting time to help me find the subject that best fitted my interests and knowledge.

John S. Kosmatos, MS, my uncle, whose viewpoints on wind turbine technology have always been a source of inspiration and constructive debate.

Solemn declaration about plagiarism and copyrights:

I have read and comprehended the rules considering plagiarism and correct citation of the used sources, described in the guide for Diploma Theses writing. I declare that, as far as I am concerned, the contents of the present Diploma Thesis are the outcome of my own work and that every source I have used is properly referenced to.

The views and conclusions included in the present Diploma Thesis belong only to its author and do not represent the official statements of the Faculty of Mechanical Engineering or the National Technical University of Athens in general.

Signed by:

Christine Kappatou

Υπεύθυνη δήλωση για λογοκλοπή και για κλοπή πνευματικής ιδιοκτησίας:

Έχω διαβάσει και κατανοήσει τους κανόνες για τη λογοκλοπή και τον τρόπο σωστής αναφοράς των πηγών που περιέχονται στον οδηγό συγγραφής Διπλωματικών Εργασιών. Δηλώνω ότι, από όσα γνωρίζω, το περιεχόμενο της παρούσας Διπλωματικής Εργασίας είναι προϊόν δικής μου εργασίας και υπάρχουν αναφορές σε όλες τις πηγές που χρησιμοποίησα.

Οι απόψεις και τα συμπεράσματα που περιέχονται σε αυτή τη Διπλωματική Εργασία είναι του συγγραφέα και δεν πρέπει να ερμηνευθεί ότι αντιπροσωπεύουν τις επίσημες θέσεις της Σχολής Μηχανολόγων Μηχανικών ή του Εθνικού Μετσόβιου Πολυτεχνείου.

Ονοματεπώνυμο:

Χριστίνα Καππάτου

Abstract

The increasing energy needs of the contemporary world have rendered renewable energy sources a condition for sustainable future. Wind energy, in particular, has turned out to be one of the most efficient and cost-effective options, the employment of which gets more widely-spread every year. However, it does not come without any environmental consequences, with noise pollution being among the most alarming ones. The present study aims for the prediction of wind turbine noise immission under neutral or stable atmospheric conditions and over flat terrain. Sound propagation is simulated by the development of a code that calculates the solution to the Parabolic Equation, assuming a monopole point source. The solution independency of the grid density and the dimensions of the computational domain and the absorbing layer is also investigated. The method reliability is validated by comparing the results to other numerical predictions and experimental measurements. Finally, the specific case of wind turbine noise propagation is assessed by applying experimental data to the developed code. The results are compared to in-situ measurements.

Περίληψη

Οι ολοένα αυξανόμενες ενεργειακές ανάγκες του σύγχρονου κόσμου έχουν καταστήσει τις ανανεώσιμες πηγές ενέργειας προϋπόθεση για βιώσιμο μέλλον. Η αιολική ενέργεια, ειδικότερα, έχει αποδειχθεί μια από τις πιο αποτελεσματικές και οικονομικές επιλογές, η αξιοποίηση της οποίας γίνεται όλο και πιο διαδεδομένη κάθε χρόνο. Ωστόσο, δεν είναι αμιγής περιβαλλοντικών επιπτώσεων, με την ηχορύπανση να είναι μια από τις πιο ανησυχητικές. Η παρούσα εργασία στοχεύει στην πρόλεξη της διάδοσης του θορύβου από ανεμογεννήτρια υπό ουδέτερες ή σταθερές ατμοσφαιρικές συνθήκες και κατά μήκος επίπεδης τοπογραφίας. Η διάδοση του ήχου προσεγγίζεται με την ανάπτυξη κώδικα που υπολογίζει τη λύση της Παραβολικής Εξίσωσης, υποθέτοντας μονοπολική σημειακή πηγή. Επίσης διερευνάται η ανεξαρτησία της λύσης από την πυκνότητα πλέγματος, καθώς και τις διαστάσεις του υπολογιστικού χωρίου και του απορροφητικού στρώματος. Η αξιοπιστία της μεθόδου πιστοποιείται μέσω σύγκρισης των αποτελεσμάτων με άλλες αριθμητικές προλέξεις και πειραματικές μετρήσεις. Τέλος, η ειδική περίπτωση της διάδοσης θορύβου από ανεμογεννήτρια εκτιμάται εφαρμόζοντας πειραματικά δεδομένα στον προκύπτοντα κώδικα. Τα αποτελέσματα συγκρίνονται με επί τόπου μετρήσεις.

Contents

1. Introduction

1.1. Technological problem analysis……...……..pg.1
1.2. Literature review of noise propagation methods…….....…..pg.2

2. The Parabolic Equation method

2.1. Mathematical formulation……...…pg.6
2.2. Numerical Simulation
i. PE discretization……..……...pg.10
ii. Boundary conditions…….……pg.14
iii. Atmospheric absorption and other propagation losses……..…pg.17
iv. Simulation of acoustic source……...pg.19
2.3. Numerical parameters study
i. Grid density……...…….……pg.20
ii. Top grid surface height and absorbing layer thickness…….....…..pg.23
iii. Comparison to narrow-angle approximation results……..pg.29

3. Results

3.1. Method validation
i. Comparison with the analytical solution and with predictions of other methods…...pg.31
ii. Comparison with predictions for the Rock Springs experiment……....pg.36
iii. Comparison with predictions for the Radlett experiment…….....pg.43
3.2. Application on the prediction of wind turbine noise immission
i. The Tammhausen experiment……...…….pg.50
ii. The Lyse experiment……..……..pg.53
iii. The Høvsøre experiment……..…pg.55

4. Conclusions and future work

4.1. Conclusions……..pg.58
4.2. Suggestions for future work……..pg.59

References…….pg.60

1.Introduction

1.1. Technological problem analysis

Overpopulation and fast economic growth around the globe have been changing drastically the energy requirements over the past few decades. As a result, fossil fuels, widely used in the past to cover such needs, are now being depleted in alarming rates, only to leave behind the devastating effects of climate change on both humans and nature.

Renewable energy sources seem to be the only way to a sustainable future, with wind turbines standing among the most prominent options. Indicatively, there are currently 743 GW of installed wind capacity worldwide, 93 GW of which were added by China and U.S. just in 2020 [1]. However, wind power stations are often claimed to cause discomfort or even deterioration of everyday life to the local residents and fauna.

The construction of a wind park often leaves behind a deforested land, prone to soil erosion, causing significant habitat loss, if not properly restored [2]. Furthermore, air-collision of birds and bats with the moving rotor blades contributes to rise in their mortality rates. Shifting to issues that affect humans directly, the interference of the wind turbine with the electromagnetic signals is among common complains of the locals. To their disturbance also constitutes the visual impact, attributed not only to the intimidating physique of the wind turbine, often ill-assorted to the adjacent landscape, but also to the flickering effect caused by the passing of the sunlight through the rotating blades, creating a repeatedly occurring shadow. Last but not least, the noise produced by a wind turbine is often reported by the locals as a source of nuisance [3]. Such annoyance can have various indirect health effects, including migraines, dizziness, tinnitus, stress, rise in blood pressure and sleep disturbance [4]. It can also be associated with increased stress levels of the fenced animals that live nearby, as long as with communication disturbance among wild species, due to sound masking or hearing impairments [2].

The effects of noise disturbance on the local residents and fauna, along with the financial damage entailed by a possible operation interruption of a wind farm due to above-limit measured noise levels in residential areas, call for the development of numerical models that provide safe estimations of wind turbine noise generation and propagation. The aim of the present study is the development of a fast and reliable numerical tool, capable of simulating noise propagation in the atmospheric environment and, therefore, permitting the accurate estimation of noise levels at critical distances around a wind turbine.

1.2. Noise propagation methods: A literature Review

During the past decades, a number of computational methods have been developed for the numerical simulation of atmospheric noise propagation. Among the most common ones lie the Parabolic Equation, the Ray Theory, the Wavenumber Integration and the Normal Modes methods that have been developed for underwater acoustics models. Furthermore, during the last two decades, due to the increase in computer capacity, sound propagation can be calculated through the solution of the Linearized Euler Equations by use of finite differences or finite volumes. A brief description of the principles, the developed models and the applications of each method follows, along with the choice finally applied in this study.

The **Parabolic Equation (PE) method** is used for the computation of the sound field produced by a monopole source in a refracting atmosphere and above the ground surface. Assuming waves travelling only in the positive direction and, thus, negligible back-scattering, this is achieved through the solution of a parabolic equation. This method ignores contributions to the field of sound waves with large elevation angles. Hence, there is a maximum for elevation angle values, beyond which its accuracy is put into question [15, App.G, "Parabolic Equation (PE) method", pg. 163-180].

Although the method is now widely used in atmospheric acoustics, it was introduced as an underwater model by Hardin and Tappert [6, Ch.6: "Parabolic Equations", pg. 457–529] for the development a full-wave alternative to ray-tracing methods [17]. The necessary adaptations for the prediction of atmospheric noise propagation were made by Gilbert and White [16], who developed a wide-angle PE model that can be applied to the case of flat, locally reacting ground surfaces. Furthermore, in [17], they used the latter model, called "Crank-Nicholson PE method" [15, App.G, "Parabolic Equation (PE) method", pg. 163-180], to study the refractive effects of atmospheric profiles to sound propagation over flat, open, finite-impedance ground.

A variation of the PE was developed by Di and Gilbert, called the "Green Function PE method", also an axisymmetric approximation [40]. Albeit less accurate than the CNPE in cases of wide-angle propagation and large sound speed profiles, the CFPE method is faster, due to the larger extrapolation steps used in the parabolic direction [15, App. H, "Green's Function Parabolic Equation (GFPE) method", pg. 181-202]. Another interesting feature of this method, developed by Di and Gilbert [18] is that it can be extended to three-dimensional problems.

Barlas et al. employed the PE method [19] to predict the noise propagation from a wind turbine, having estimated the flow field, by use of a model that employs the Large Eddy Simulation and Actuator Disc methods. In [20] they used a two-dimensional PE method, coupled with an analytical wake model and Large Eddy Simulation and Actuator Disc methods for the assessment of the effects of wake-induced velocity and turbulence on the sound that propagates from a wind turbine.

Lee et al. [21] developed a PE tool for wind turbine noise propagation, aiming at the expression of the effects of wind and temperature profiles on sound propagation and, hence, on the perceived sound in the far field. As an input for sound propagation prediction with evolving wake flows, the model used CFD-calculated evolving wake flows. However, it underestimated far-field noise levels in the upwind direction[*], as a result of ignoring the turbulence scattering effect.

According to **Ray Theory**, sound propagates along rays, normal to surfaces on which the phase of the acoustic waves remains constant, called wave fronts [5]. Each ray follows a trajectory, calculated through the ray tracing technique, that involves the integration of the trajectory differential equations in some time interval. The rays that start from the source and reach the receiver are called "eigenrays". The contribution of each eigenray to the total sound pressure level is calculated by subtracting the losses along the trajectory from the sound power level of the source. This provides the amplitude of the complex pressure field, whilst the phase is estimated from the integration time along the eigenray. The total sound pressure field, perceived by the receiver is then calculated as a superposition of the components from the total number of eigenrays [41].

A serious flaw of this theory is the underprediction of the sound pressure level in the case of upwind sound propagation. To this contributes the occurrence of the "shadow zones", in which the pressure field is calculated

[*] as defined in [21], par. III. C

as identically zero [6, Ch.3: "Ray Methods", pg. 155–232]. In reality, however, the diffraction of sound on obstacles can be the cause of some level of sound pressure. Berry and Daigle overcame that problem [7], by formulating the diffraction theory in terms of a residue series and then extending the solution to the general case of a finite impedance by removing restrictive approximations and retaining higher-order terms. The geometrical theory, that considers reflections from a curved surface, was used for the calculation of the sound field above the shadow boundary.

This approach was used by L' Espérance et al. [8] for the development of a tool for outdoor sound propagation assessment that took under consideration the fact that acoustical rays appear as circular arcs for a linear sound speed profile, as was proved by Hidaka [9]. The common energy loss mechanisms of geometrical spreading, atmospheric absorption, ground effect and atmospheric refraction were also considered by this model.

Another drawback of the ray theory is that accuracy can be achieved principally for high frequencies [5, 6]. However, Raspet et al. [10] showed that, in long distances from the source, ground absorption cancels out the effects of lower frequencies, that do not fit the ray tracing accuracy criteria, set by Brekhovskikh in [11].

Ray theory was applied in the work of Prospathopoulos and Voutsinas for the investigation of wind turbine and wind park noise propagation, taking atmospheric absorption, wave refraction and diffraction as well as atmospheric turbulence into account [12]. They have examined how noise emissions from isolated wind turbines and from wind parks are affected by parameters such as ground impedance, temperature, humidity, turbulence, and wind velocity [13]. In addition to that, they have developed a ray-tracing model, that uses axisymmetric calculations for the estimation of the sound pressure field around an isolated source, to determine appropriate sound speed profiles for near ground propagation, taking into account sound energy losses from ground and atmospheric absorption as well as atmospheric turbulence [14].

The **Wavenumber Integration** and the **Normal Modes** methods are both numerical implementations of the Integral Transform Technique. The latter is widely used in boundary value problems, regarding environments where the boundary conditions and the coefficient of the Helmholtz equation are both independent of any number of space coordinates. Application of integral transforms, i.e., Fourier transforms, or separation of variables to these cases can lead to dimension reduction of the wave equation and the boundary conditions [6, Ch.2: "Wave Propagation Theory", pg. 65–153]. The sound pressure is expressed as a wavenumber integral of the solutions of the reduced wave equation that is evaluated differently in each method. Namely, in the wavenumber integration method, numerical quadrature calculations are employed (often the Fast Fourier Transforms, hence the term FFP -Fast Field Programs- for that approach), while in the normal mode method, a complex contour integration is implemented to reduce the integral representation to a sum of residues. [6, Ch.4: "Wavenumber Integration Techniques", pg. 233-335].

The FFP method, originally developed for underwater acoustics by Pekeris [22] and seismic propagation in few-layer waveguides by Jardetzky [23] and Ewing et al. [24], was first applied to atmospheric sound propagation by Lee et al. [25] for the case of complex impedance ground. The numerical overflow problems that emerged for high frequencies and multiple layers were eliminated by the new formulation, developed by Lee et al. [26], involving the calculation of the equivalent impedance for each layer, starting from the top and bottom ones and moving successively towards the source.

Wilson [27] developed a three-dimensional FFP method, similar to the one of Li et al. [28], but used the theoretical basis applied by Nijs and Wapenaar in [29], differing only in that he expressed the wave equation of a moving medium in terms of velocity potential, instead of acoustic pressure and particle velocity, simplifying it significantly. The global matrix methods suggested by Schmidt and Tango [30] facilitated considerably the numerical calculations.

The normal modes method was employed by Raspet et al. [31] for the prediction of low-frequency sound propagation in a downward refracting atmosphere and across a complex impedance ground surface, since the ray tracing approaches give unsatisfactory results in such conditions. The proof of the intense dependency of sound propagation in a downward refracting atmosphere on the interaction between the finite-impedance ground surface and the refracted sound was the outcome of this study.

Keith, Daigle and Stinson, in the framework of "Health Canada's Community Noise and Health Study" assessed the wind turbine infrasound and low frequency levels near 1238 dwellings. The FFP was one of the methods they used to estimate wind turbine noise propagation and it proved to give satisfactory results for large distances, large wind turbine numbers and in the case where specific meteorological classes are used to replace on-site meteorological data, given that infrasound approaches perceptible levels [32].

Prospathopoulos et al. [33] proposed an axisymmetric model for wind turbine noise propagation along complex terrain, called "NOISEPRO". This code consists of the model "KRAKEN", that is based upon the normal modes method for the low-frequency domain, and the model "AERAS" that uses a ray tracing technique for the high-frequency domain. At the same time, it takes under consideration the mean wind velocity vertical profile, the ground surface variations and the range dependence on the medium characteristics. The results for high-frequency noise propagation proved compatible to the measurements, in contrast to the ones for low-frequency noise propagation, that, in most cases, deviated significantly, proving that the normal modes method failed to predict credibly the ground effect.

The **Linearized Euler Equations (LEEs)**, obtained by applying basic aeroacoustics assumptions to the Euler Equations [34] is a more advanced and, yet, computationally more demanding method for sound propagation simulation. The equation set is solved using the finite volumes or finite differences method [35]. In the latter case, and when time-domain solutions are required, the method is called "Finite Difference Time Domain method", or "FDTD method" and, during the past three decades, it has been acknowledged for its ability to include into calculations complicated wave effects such as scattering, reflection or diffraction near bodies of random shape. Additionally, it can predict complex medium effects, with convection, refraction and turbulent or non-turbulent scattering being among the most common ones [36]. These merits were taken advantage of by Van Renterghem et al. [37], along with the virtues of the PE method, namely small computational time and accurate predictions of sound propagation to a distant receiver, for the development of a hybrid model that calculates the sound propagation in situations where the source is close to several obstacles. The FDTD part of this model was responsible for calculations near the complex source and the PE part for propagation to a distant receiver, across a flat terrain.

An adaptive FDTD model was developed by Shiguang and Jin Liu [38] for the calculation of sound propagation in three-dimensional outdoor scenes. The atmospheric inhomogeneity and ground effects on the pressure field were considered. The results were realistic and computationally cost-effective. However, there is still a significant precomputational cost, while the fact that the PE method assumes a single propagation direction hinders the predictions in the case of multiple sources.

The effects of topography and atmosphere on sound propagation were also studied by Blumrich and Heimann [39]. In their study, they developed a sound propagation model along with a flow model, both based on the solution of the LEEs for the prediction of sound propagation in a three-dimensionally inhomogeneous atmosphere and across a rigid, partly reflective or fully absorptive terrain. Comparison of the model results to analytical predictions and measurements proves it to be a reliable tool. Nevertheless, it entails time-consuming calculations, especially in the case where finite ground impedance modelling is required.

The present study aims for the development of an efficient model, suitable for the simulation of noise propagation in the atmospheric environment and able to focus on wind turbine noise immission. This can be achieved in the cases of flat or smooth terrain, where the crosswind propagation effect can be neglected, allowing for the adoption of an axisymmetric approach. As such, the Parabolic Equation (PE) method was selected. Indeed, a parabolic approach complies favorably with either flat or smooth terrain cases, where no back-scattering propagation occurs. Furthermore, the PE calculations are performed in the frequency domain, thus permitting the investigation of the pressure field only for frequencies of interest. In the low-frequency domain, such a consideration allows for the employment of coarse grids, reducing significantly the computational cost. Finally, the wide-angle approximation, adopted in the present work, removes any angular limitations of the PE method and renders it adequate for the simulation of wind turbine-originated sound propagation.

Knowing the method to be employed determines the course of the study that is described in the three remaining chapters of this dissertation. In Chapter 2 the narrow and wide-angle parabolic equations are derived from the

two-dimensional Helmholtz equation. The resulting system of equations, along with the initial and boundary conditions, are then discretized numerically for the model development. This is followed by the investigation of the solution independency of the grid density as well as the dimensions of the computational domain and the absorbing layer. In Chapter 3, the code credibility gets validated by comparing the results to ones from other theoretical predictions, using the same initial conditions. Then, the model is applied to actual wind turbine cases, using data from onsite measurements. Conclusions and future work suggestions can be found in Chapter 4.

2. The Parabolic Equation (PE) method

In the present chapter the mathematical equations and their discretization, along with the boundary conditions required for the calculation of the pressure field are presented. The simulation also includes the modelling of the atmospheric absorption, the ground effect and the noise source. A study of numerical parameters, namely grid density as well as computational domain and absorbing layer dimensions, is finally conducted.

2.1. Mathematical formulation

For the mathematical setup, the Crank-Nicholson Parabolic Equation (CNPE) method is followed, as described by Salomons [15, App.G, "Parabolic Equation (PE) method", pg. 163-180]. Since it is an axisymmetric approximation, the three-dimensional Helmholtz equation reduces to its two-dimensional form:

$$\frac{\partial^2 q}{\partial r^2}+\frac{\partial^2 q}{\partial z^2}+k^2\cdot q=0, \qquad \textbf{(2.1)}$$

where the r-z coordinates are shown in Fig.2.1 and the wave number k is equal to ω/c, with ω being the angular frequency and c the sound speed. The quantity q(r, z) has the following relation with the complex pressure amplitude, p(r, z):

$$q=p\cdot\sqrt{r} \qquad \textbf{(2.2)}$$

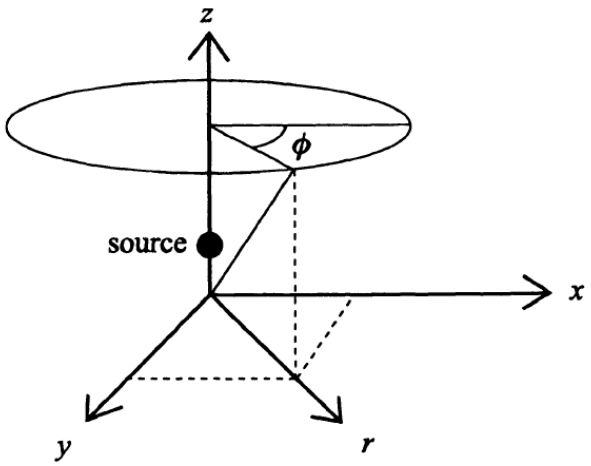

Fig.2.1: The cylindrical rzφ coordinated for the axisymmetric approach (sound field variation with the azimuthal angle, φ, is neglected). Source: [15, App.E, "Basic acoustic equations for a layered refracting atmosphere", pg. 139-151].

The solution of the PE can vary, depending on whether a narrow-angle or a wide-angle approximation is considered. The PE, as modified for each approach, is derived in the next two paragraphs.

For the **Narrow-angle Approximation**, valid only for angles up to about 10°, the solution of eq.**(2.1)** is set as follows:

$$q(r, z)=\psi(r,z)\cdot e^{i\cdot k_0\cdot r}, \qquad \textbf{(2.3)}$$

where k_0 is the value of the wave number k(z) at the ground surface.

Substitution of **(2.3)** into **(2.1)** yields:

$$\frac{\partial^2\psi}{\partial r^2}+2\cdot i\cdot k_0\cdot\frac{\partial\psi}{\partial r}+\frac{\partial^2\psi}{\partial z^2}+\left(k^2-k_0^2\right)\cdot\psi=0 \qquad \textbf{(2.4)}$$

However, in most cases, ψ varies slowly with r, therefore, the first term of the left-hand side of **(2.4)**, being considerably smaller than the other two, can be neglected.

Additionally, one can substitute the difference $\left(k^2-k_0^2\right)$, with the quantity δk^2.

Given the last two remarks, eq. **(2.4)** can be written as:

$$2\cdot i\cdot k_0\cdot\frac{\partial\psi}{\partial r}+\frac{\partial^2\psi}{\partial z^2}+\delta k^2\cdot\psi=0, \qquad \textbf{(2.5)}$$

which is called "the **narrow-angle parabolic equation**".

It is interesting to note here that there is an alternative to the derivation of eq. **(2.5)**. That is, by introducing the operator:

$$H_2(z)=k^2(z)+\frac{\partial^2}{\partial z^2}, \qquad \textbf{(2.6)}$$

one can write equation **(2.1)** as:

$$\frac{\partial^2 q}{\partial r^2}+H_2(z)\cdot q=0 \qquad \textbf{(2.7)}$$

However, from **(2.6)** it is also true that:

$$H_2(z)=[k^2(z)-k_0^2]+k_0^2+\frac{\partial^2}{\partial z^2}\xrightarrow{\delta k^2=k(z)^2+k_0^2} H_2(z)=\delta k^2+k_0^2+\frac{\partial^2}{\partial z^2} \qquad \textbf{(2.8)}$$

Introducing the operator s as:

$$s=\frac{\delta k^2+\frac{\partial^2}{\partial z^2}}{k_0^2}, \qquad \textbf{(2.9)}$$

(2.8) can be written as:

$$H_2(z)=k_0^2\cdot(1+s) \qquad \textbf{(2.10)}$$

Taking **(2.10)** one step further, one can write:

$$H_2(z)=\left(k_0\cdot\sqrt{1+s}\right)^2 \qquad \textbf{(2.11)}$$

Substituting the quantity $k_0 \cdot \sqrt{1+s}$ with the operator $H_1(z)$, **(2.11)** becomes:

$$H_2(z)=H_1^2(z) \qquad \textbf{(2.12)}^*$$

Equation **(2.7)** can, now, be written as:

$$[\frac{\partial}{\partial r} - i \cdot H_1(z)] \cdot [\frac{\partial}{\partial r} + i \cdot H_1(z)] \cdot q = 0 \qquad \textbf{(2.13)}^\dagger$$

The first term of the left-hand side of eq. **(2.13)** expresses waves that travel in the positive r direction, while the second term, expresses waves traveling in the negative direction. However, in this study, the source is considered to be at r=0 and the receiver at r>0. Hence only the waves that travel towards the positive r direction are of interest. Neglecting any back-scattering, eq. **(2.13)** reduces to:

$$\frac{\partial q}{\partial r} - i \cdot H_1(z) \cdot q = 0 \qquad \textbf{(2.14)}$$

Neglecting any term of order greater than two in the expansion of the operator $\sqrt{1+s}$, $H_1(z)$ can be written as:

$$H_1(z) = k_0 \cdot (1+\frac{1}{2}s) \qquad \textbf{(2.15)}$$

Substitution of **(2.9)** and **(2.15)** into **(2.14)**, gives:

$$\frac{\partial q}{\partial r} - i \cdot k_0 \cdot q - i \cdot \frac{\delta k^2 + \frac{\partial^2}{\partial z^2}}{2 \cdot k_0} \cdot q = 0 \qquad \textbf{(2.16)}$$

A final substitution of eq. **(2.3)** into eq. **(2.16)** yields the final form of the narrow-angle parabolic equation **(2.5)**:

$$2 \cdot i \cdot k_0 \cdot \frac{\partial \psi}{\partial r} + \frac{\partial^2 \psi}{\partial z^2} + \delta k^2 \cdot \psi = 0$$

This calculation route can be followed for the **Wide-Angle Approximation** as well. The same steps can be taken, until equation **(2.15)** in which, this time, a more accurate expansion of the square-root operator is used:

$$H_1(z) = k_0 \cdot \frac{1+\frac{3}{4} \cdot s}{1+\frac{1}{4} \cdot s}, \qquad \textbf{(2.17)}$$

---

*The square-root of the differential operator (1+s) is defined by the expansion: $\sqrt{1+s}=1+\frac{1}{2}s-\frac{1}{2}s^2+\ldots$, just like the expansion of a common square-root function. Therefore, the operator $\sqrt{1+s}$ behaves as a square-root function and equations like **(2.12)** hold true.

† The difference of squares in **(2.13)** is valid assuming that $H_1 \cdot \frac{\partial}{\partial r} = \frac{\partial}{\partial r} \cdot H_1$, which is true only for the case of layered atmosphere, where k=k(z), which is considered here. For a range dependent wave number, i.e. k=k(r,z), assuming commutation between the two operators is an approximation.

where $\frac{1}{1+\frac{1}{4}\cdot s}$ is the inverse of the operator $1+\frac{1}{4}\cdot s$.

Substitution of **(2.17)** in **(2.14)**, yields:

$$\frac{\partial q}{\partial r} - i\cdot k_0 \cdot \frac{1+\frac{3}{4}\cdot s}{1+\frac{1}{4}\cdot s}\cdot q=0 \qquad \textbf{(2.18)}$$

Considering, finally, eq. **(2.3)**, one can write the wide-angle parabolic equation as:

$$\frac{\partial \psi}{\partial r} - i\cdot k_0 \cdot \frac{\frac{1}{2}\cdot s}{1+\frac{1}{4}\cdot s}\cdot \psi=0 \qquad \textbf{(2.19)}$$

2.2. Numerical Simulation

i. PE discretization

The finite-differences method is employed for the solution of the narrow-angle and wide-angle parabolic equations derived in the sections above.

Solution of the Narrow-angle PE

Defining the parameters α and β as: $\alpha=\frac{i}{2\cdot k_a}$ and $\beta=\frac{i\cdot\delta k^2}{2\cdot k_a}$ respectively and substituting them in eq. **(2.5)**, one gets:

$$\frac{\partial\psi}{\partial r}=\alpha\cdot\frac{\partial^2\psi}{\partial z^2}+\beta\cdot\psi \qquad \textbf{(2.20)}$$

The grid used for the field computation is an rz plane and is depicted in Fig.2.2. It is divided in sections of Δr length horizontally and of Δz height vertically. As will be proven in Sec.2.3.i, accurate results can be obtained for Δr and Δz equal to λ/10 or less, where λ is an average wavelength. It is also evident from Fig.2.2 that the ground surface is placed at z=0, while the total height of the grid is finite and equal to z_M. The area between z_t and z_M at the top serves as an absorbing layer and will be further analyzed in Sec.2.3.ii. The grid spacings are at heights:

$$z_j=j\cdot\Delta z,\ j=1,\ 2,\ 3,\ \ldots,\ M \qquad \textbf{(2.21)}$$

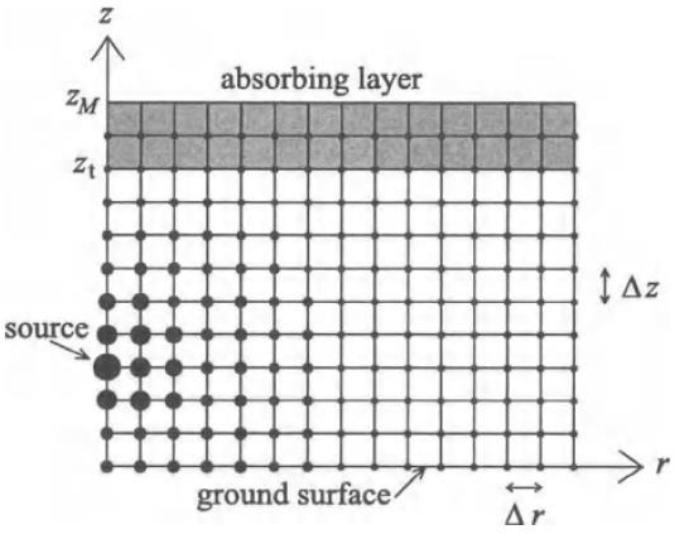

Fig.2.2: The employed grid in the r-z plane. The ground surface is at z=0, the top of the grid at $z=z_M$ and the absorbing layer covers the region $z_t \le z \le z_M$.

The field ψ that is to be calculated is denoted at range r as a vector: $\vec{\psi}(r)$, the elements of which are symbolized as: $\psi_j=\psi(r, z_j)$.

For the discretization of the second-order term in eq.**(2.20)**, the central difference formula is used as follows:

$$\left(\frac{\partial^2\psi}{\partial z^2}\right)_{z_j}=\frac{\psi_{j+1}-2\cdot\psi_j+\psi_{j-1}}{(\Delta z)^2} \qquad \textbf{(2.22)}$$

With the aid of eq.**(2.22)**, **(2.20)** can be written as:

$$\frac{\partial}{\partial r}\begin{pmatrix}\psi_1\\ \psi_2\\ \psi_3\\ \vdots\\ \psi_{M-1}\\ \psi_M\end{pmatrix}=\left[\gamma\begin{pmatrix}-2 & 1 & & & & \\ 1 & -2 & 1 & & & \\ & 1 & -2 & 1 & & \\ & & \ddots & \ddots & \ddots & \\ & & & 1 & -2 & 1\\ & & & & 1 & -2\end{pmatrix}+\begin{pmatrix}\beta_1 & & & & \\ & \beta_2 & & & \\ & & \beta_3 & & \\ & & & \ddots & \\ & & & & \beta_{M-1} & \\ & & & & & \beta_M\end{pmatrix}\right]\cdot\begin{pmatrix}\psi_1\\ \psi_2\\ \psi_3\\ \vdots\\ \psi_{M-1}\\ \psi_M\end{pmatrix}+\gamma\begin{pmatrix}\psi_0\\ 0\\ 0\\ \vdots\\ 0\\ \psi_{M+1}\end{pmatrix}, \qquad \textbf{(2.23)}$$

where $\gamma=\frac{\alpha}{(\Delta z)^2}$ and $\beta_j=\beta(z_j)$.

A closer observation of eq.**(2.23)** leads to the conclusion that the last vector of the right-hand side replaces the two terms that are missing from the first and the last row of the tridiagonal matrix. Its elements ψ_0 and ψ_{M+1}, represent the field for $z_0=0$, i.e. ground level, and $z_{M+1}=(M+1)\cdot\Delta z$, i.e, top of the grid, respectively, where the boundary conditions, set in Sec.2.2.ii are satisfied.

That said, ψ_0 is calculated from the relationship:

$$\psi_0=\sigma_1\psi_1+\sigma_2\psi_2, \qquad \textbf{(2.24)}$$

where coefficients σ_1 and σ_2 depend on the ground impedance.

On the other hand, ψ_{M+1} is given by the relation:

$$\psi_{M+1}=\tau_1\psi_M+\tau_2\psi_{M-1}, \qquad \textbf{(2.25)}$$

where coefficients τ_1 and τ_2 can be similarly derived as σ_1 and σ_2, as will be proven in the next section.

All in all, the vector equation **(2.23)** is a set of M equations, each one of them relating an element $\frac{\partial\psi_j}{\partial r}$ to the elements ψ_{j-1}, $\psi_j$and ψ_{j+1}.

Introducing a tridiagonal matrix, $\overleftrightarrow{T}$, defined as:

$$\overleftrightarrow{T}=\begin{pmatrix}-2+\sigma_1 & 1+\sigma_2 & & & & \\ 1 & -2 & 1 & & & \\ & 1 & -2 & 1 & & \\ & & \ddots & \ddots & \ddots & \\ & & & 1 & -2 & 1\\ & & & & 1+\tau_2 & -2+\tau_1\end{pmatrix} \qquad \textbf{(2.26)}$$

and a diagonal matrix, $\overleftrightarrow{D}$, defined as:

$$\overleftrightarrow{D}=\begin{pmatrix}\beta_1 & & & & & \\ & \beta_2 & & & & \\ & & \beta_3 & & & \\ & & & \ddots & & \\ & & & & \beta_{M-1} & \\ & & & & & \beta_M\end{pmatrix}, \qquad \textbf{(2.27)}$$

equation **(2.23)** can be written as:

$$\frac{\partial \vec{\psi}}{\partial r} = (\gamma \cdot \overleftrightarrow{T} + \overleftrightarrow{D}) \cdot \vec{\psi} \qquad \textbf{(2.28)}$$

Integration of equation **(2.28)** from r to r+Δr, yields:

$$\vec{\psi}(r + \Delta r) - \vec{\psi}(r) = (\gamma \cdot \overleftrightarrow{T} + \overleftrightarrow{D}) \cdot \int_{r}^{r+\Delta r} \vec{\psi} \cdot dr \qquad \textbf{(2.29)}$$

For the approach of the integral on the right-hand side of eq.**(2.29)**, the Crank-Nicholson approximation is used, according to which:

$$\int_{r}^{r+\Delta r} \vec{\psi} \cdot dr \cong \frac{1}{2} \cdot [\vec{\psi}(r + \Delta r) + \vec{\psi}(r)] \cdot \Delta r \qquad \textbf{(2.30)}$$

Substitution of **(2.30)** into **(2.29)** gives:

$$\vec{\psi}(r + \Delta r) - \vec{\psi}(r) = (\gamma \cdot \overleftrightarrow{T} + \overleftrightarrow{D}) \cdot \frac{1}{2} \cdot [\vec{\psi}(r + \Delta r) + \vec{\psi}(r)] \cdot \Delta r \Rightarrow [1 - \frac{1}{2} \cdot (\gamma \cdot \overleftrightarrow{T} + \overleftrightarrow{D})] \cdot \vec{\psi}(r + \Delta r) = [1 + \frac{1}{2} \cdot (\gamma \cdot \overleftrightarrow{T} + \overleftrightarrow{D})] \cdot \vec{\psi}(r)$$

Defining the above tridiagonal matrices in brackets as:

$$\overleftrightarrow{M}_1 = [\overleftrightarrow{I} + \frac{1}{2} \cdot \Delta r \cdot (\gamma \cdot \overleftrightarrow{T} + \overleftrightarrow{D})] \qquad \textbf{(2.31)}$$

and

$$\overleftrightarrow{M}_2 = [\overleftrightarrow{I} - \frac{1}{2} \cdot \Delta r \cdot (\gamma \cdot \overleftrightarrow{T} + \overleftrightarrow{D})] \qquad \textbf{(2.32)}$$

one receives the final discretized form of the above narrow-angle parabolic equation:

$$\overleftrightarrow{M}_2 \cdot \vec{\psi}(r + \Delta r) = \overleftrightarrow{M}_1 \cdot \vec{\psi}(r) \qquad \textbf{(2.33)}$$

The step-wise solution of the PE, from $\vec{\psi}(r)$ to $\vec{\psi}(r + \Delta r)$, is reduced to the solution of the set of M linear equations presented in eq. **(2.33)** for the M unknowns $\vec{\psi}_j(r+\Delta r)$. Given that M_1 and M_2 are tridiagonal matrices, this can be achieved through the Thomas algorithm [43].

Solution of the Wide-Angle PE

Dividing equation **(2.5)** with the quantity $(2 \cdot i \cdot k_0)$ and substituting the operator s, as defined in eq. **(2.9)**, one can bring the narrow-angle parabolic equation to the following form:

$$\frac{\partial \psi}{\partial r} - \frac{1}{2} \cdot i \cdot k_0 \cdot s \cdot \psi = 0 \qquad \textbf{(2.34)}$$

Comparison of the latter equation with the wide-angle parabolic equation **(2.19)** reveals that the only difference between them is the factor: $(1+\frac{1}{4}\cdot s)$ on the left-hand side.

Another comparison between the two forms of the narrow-angle PE **(2.5)** and **(2.28)** shows that $(\gamma\cdot\overleftrightarrow{T}+\overleftrightarrow{D})$ is the finite difference matrix form of the operator $\frac{1}{2}\cdot i\cdot k_0\cdot s$, meaning that the operator s corresponds to the matrix: $\frac{2}{i\cdot k_0}\cdot(\gamma\cdot\overleftrightarrow{T}+\overleftrightarrow{D})$.

Therefore, the matrix for the wide-angle PE operator $(1+\frac{1}{4}\cdot s)$ is: $[1+\frac{(\gamma\cdot\overleftrightarrow{T}+\overleftrightarrow{D})}{2\cdot i\cdot k_0}]$.

All of the above considered, the wide-angle parabolic equation **(2.19)** can be written in the form of eq. **(2.33)**, with matrices $\overleftrightarrow{M}_i$ this time equal to:

$$\overleftrightarrow{M}_1=[\overleftrightarrow{I}+\frac{1}{2}\cdot\Delta r\cdot(\gamma\cdot\overleftrightarrow{T}+\overleftrightarrow{D})]+\frac{(\gamma\cdot\overleftrightarrow{T}+\overleftrightarrow{D})}{2\cdot i\cdot k_0} \qquad \textbf{(2.35)}$$

and

$$\overleftrightarrow{M}_2=[\overleftrightarrow{I}-\frac{1}{2}\cdot\Delta r\cdot(\gamma\cdot\overleftrightarrow{T}+\overleftrightarrow{D})]+\frac{(\gamma\cdot\overleftrightarrow{T}+\overleftrightarrow{D})}{2\cdot i\cdot k_0} \qquad \textbf{(2.36)}$$

respectively.

ii. Boundary conditions

Boundary condition at the ground surface

Assuming a non-rigid, locally reacting ground surface, the complex pressure amplitude, p_c, and the normal component of the complex velocity amplitude in the negative z-direction, $v_{c,z}$, must be continuous at z=0. Mathematically, this can be expressed as:

$$\left(\frac{p_c}{v_{c,z}}\right)_{z=-\varepsilon} = \left(\frac{p_c}{v_{c,z}}\right)_{z=+\varepsilon}, \quad \textbf{(2.37)}$$

where $\varepsilon>0$ and $\varepsilon\rightarrow 0$.

The right-hand side of **(2.37)** is the impedance of the ground surface and is equal to $Z\rho c$, where Z is the normalized impedance of the ground surface and $\rho\cdot c$ the air impedance, evaluated just above the ground surface. Therefore, **(2.37)** can be written as:

$$\left(\frac{p_c}{v_{c,z}}\right)_{z=0} = Z\rho c \quad \textbf{(2.38)}$$

Writing the pressure and velocity fields respectively as:

$$p=\mathrm{Re}\{p_c\cdot e^{-i\omega t}\} \quad \textbf{(2.39)}$$

$$\vec{v}= \mathrm{Re}\ \{\vec{v}_c\cdot e^{-i\omega t}\}, \quad \textbf{(2.40)}$$

the linear acoustic equation for momentum conservation can be expressed in the following simplified form:

$$v_{c,z}= -\frac{1}{i\cdot\omega\cdot\rho}\cdot\frac{\partial p_c}{\partial z} \quad \textbf{(2.41)}$$

The first-order finite-difference approximation of the partial derivative of the complex pressure amplitude shown in **(2.41)** is:

$$\frac{\partial p_c}{\partial z} = \frac{p_1-p_0}{\Delta z}, \quad \textbf{(2.42)}$$

where $p_j=p_c(z_j)$.

Substitution of **(2.42)** and **(2.38)** in **(2.41)** yields:

$$p_0=\frac{1}{1-\frac{i\cdot k_0\cdot\Delta z}{Z}}\cdot p_1, \quad \textbf{(2.43)}$$

where $k_0=\frac{\omega}{c_0}$ is the wave number at the ground surface.

Nevertheless, one must bear in mind that the wide-angle parabolic equation requires a second-order approximation of $\frac{\partial p_c}{\partial z}$ for accurate results. In that case, the following expression can be used instead of eq. **(2.42)**:

$$\frac{\partial p_c}{\partial z} = \frac{-\frac{3}{2}p_0 + 2p_1 - \frac{1}{2}p_2}{\Delta z}, \quad \textbf{(2.44)}$$

Now, substituting **(2.44)** and **(2.38)** in **(2.41)**, one gets:

$$p_0 = \frac{4 \cdot p_1 - p_2}{3 - \frac{2 \cdot i \cdot k_0 \cdot \Delta z}{Z}}, \quad \textbf{(2.45)}$$

Some important notes regarding the calculation of this section are:

- Since **(2.2)** and **(2.3)** hold true, equations **(2.43)** and **(2.45)** can be rewritten by replacing p_j with ψ_j. Therefore, by comparison with eq. **(2.24)**, one can deduce that:

→ $\sigma_1 = \frac{1}{1 - \frac{i \cdot k_0 \cdot \Delta z}{Z}}$ and $\sigma_2 = 0$ for the case, where the first-order approximation of $\frac{\partial p_c}{\partial z}$ is used, while

→ $\sigma_1 = \frac{4}{3 - \frac{2 \cdot i \cdot k_0 \cdot \Delta z}{Z}}$ and $\sigma_2 = -\frac{1}{3 - \frac{2 \cdot i \cdot k_0 \cdot \Delta z}{Z}}$ for the case, where the first-order approximation of $\frac{\partial p_c}{\partial z}$ is used.

- The normalized impedance, Z, is assumed constant within a range step and, unless otherwise mentioned, is usually calculated from the expression used by Delany and Bazley [42]:

$$Z = 1 + 9.08 \cdot \left(\frac{1000 \cdot f}{\sigma}\right)^{-0.75} + i \cdot 11.9 \cdot \left(\frac{1000 \cdot f}{\sigma}\right)^{-0.73}, \quad \textbf{(2.46)}$$

where f is the sound frequency and σ is an indicative parameter for the ground absorbing capacity, called "flow resistivity".

Boundary condition at the top of the grid

The top of the surface is where $z = z_M$. This time, the normalized impedance of air is used (Z=1), instead of the ground impedance. Following a procedure similar to the one described in the previous paragraph, one gets:

$$p_{M+1} = \frac{4 \cdot p_M - p_{M-1}}{3 + 2 \cdot i \cdot k_0 \cdot \Delta z} \quad \textbf{(2.47)}$$

A comparison with equation **(2.25)** yields:

→ $\tau_1 = \frac{1}{1 - i \cdot k_0 \cdot \Delta z}$ and $\tau_2 = 0$ for the case, where the first-order approximation of $\frac{\partial p_c}{\partial z}$ is used and

→ $\tau_1 = \frac{4}{3 - 2 \cdot i \cdot k_0 \cdot \Delta z}$ and $\tau_1 = -\frac{1}{3 - 2 \cdot i \cdot k_0 \cdot \Delta z}$ for the case, where the first-order approximation of $\frac{\partial p_c}{\partial z}$ is used.

Top surface absorbing layer

To avoid partial reflections of plane waves to the $z<z_M$ region, an absorbing layer from $z=z_t$ to $z=z_M$ (Fig. 2.2) must be added to the top of the grid. This is possible if an imaginary term is added to the wave number k(z), in the region $z_t \leq z \leq z_M$. This aims for a gradual wave attenuation in the absorbing layer. According to numerical tests, an efficient choice for this term is $i \cdot A_t \cdot \frac{(z-z_t)^2}{(z_M-z_t)^2}$, where A_t here takes the value of 1, 0.5, 0.4 and 0.2 at the frequencies 1000, 500, 125 and 30 Hz respectively, while for the intermediate ones, it is estimated through linear interpolation.

Important notes for this paragraph are:

- Salomons [15, App.G, "Parabolic Equation (PE) method", pg. 163-180] suggests that a safe value for the absorbing layer thickness is 50 times the wavelength of the used frequency. This is further examined in Sec. 2.3.ii, where numerical calculations are conducted under different values for the absorbing layer thickness.
- The top of the grid should be adequately high so that the absorbing layer will n ot influence the sound field. So, as will be shown during the rest of the calculations course, $z_M$will be equal to at least 1000 vertical grid spacings, complying to Salomons' instructions.
- The wave number, k(z), is calculated from the relation:

$$k(z)=\frac{\omega}{c(z)} \tag{2.48}$$

Unless otherwise stated, in this study the following logarithmic profile is used for the expression of the speed of sound:

$$c(z)=c_0+b \cdot \ln\left(1+\frac{z}{z_0}\right), \tag{2.49}$$

where c_0 is the nominal speed of sound, b is the refraction factor, describing the cases of downward, upward or non-refracting atmosphere and z_0 is the roughness length of the ground.

iii. Atmospheric absorption and other propagation losses

Atmospheric absorption causes an exponential decrease of the amplitude of the complex pressure, which can be taken into account by adding a small imaginary term, $i \cdot k_i$, to the wave number, thus replacing k with $k+i \cdot k_i$. This term is calculated as follows:

$$k_i = \frac{\alpha}{20 \cdot \log e}, \tag{2.50}$$

where α is the absorbing coefficient, determined by the following relationship:

$$\alpha = 8.686 \cdot f^2 \cdot \sqrt{\tau_r} \cdot \left(\frac{1.84}{10^{11} \cdot \rho_r} + \frac{b_1 + b_2}{\tau_r^3} \right), \tag{2.51}$$

where $\tau_r = \frac{T}{T_{20}}$, T_{20}=293.15 K and $\rho_r = \frac{p_a}{p_r}$, p_r= 101 325 Pa. The quantities b_1 and b_2 are calculated from the expressions:

$$b_1 = 0.1068 \cdot \frac{e^{-\frac{3352}{T}}}{f_{r,N} + \frac{f^2}{f_{r,N}}} \tag{2.52}$$

and

$$b_2 = 0.01275 \cdot \frac{e^{-\frac{2239.1}{T}}}{f_{r,O} + \frac{f^2}{f_{r,O}}} \tag{2.53}$$

$f_{r,N}$ and $f_{r,O}$ are the relaxation frequencies of nitrogen and oxygen, respectively, calculated from the relationships:

$$f_{r,N} = \frac{\rho_r}{\sqrt{\tau_r}} \cdot \left[9 + 280 \cdot h \cdot e^{-4.17 \cdot \left(\frac{1}{\sqrt[3]{\tau_r}} - 1 \right)} \right] \tag{2.54}$$

$$f_{r,O} = \rho_r \cdot \left(24 + 40400 \cdot h \cdot \frac{0.02 + h}{0.0391 + h} \right) \tag{2.55}$$

In the above equations, h is the percentage of molar water vapor concentration in the atmosphere and is a function of the relative humidity, r_h, i.e. the percentage of the water vapor pressure in the atmosphere over the saturation vapor pressure, p_{sat}:

$$h = \frac{r_h \cdot \rho_{sat}}{\rho_r}, \tag{2.56}$$

where $\rho_{sat} = \frac{p_{sat}}{p_r}$, by definition. However, ρ_{sat} is calculated as:

$$\rho_{sat}=10^{C_{sat}}, \tag{2.57}$$

with

$$C_{sat}=-6.8346\cdot\left(\frac{T_{01}}{T}\right)^{1.261}+4.6151, \tag{2.58}$$

where T_{01}=273.16 K is the triple-point temperature of water.

It is important to note here that the factors of propagation losses mentioned above are not the only ones to occur. Indeed, ground absorption is also a significant parameter and is taken under consideration through the boundary condition **(2.45)**, that includes the ground impedance. The losses due to spherical spreading contribute significantly to the complex pressure field values as well. Nevertheless, they are, by default, encompassed in the calculations for the solution of the PE.

iv. Simulation of acoustic source

In order for the computations to begin, a starting field is required, which should represent a monopole source. The exact expression for the field q(r,z) of a monopole source in an unbounded, non-refracting atmosphere is:

$$q(r,z)=\frac{e^{i\cdot k\cdot R}}{R}\cdot\sqrt{r}, \quad \textbf{(2.59)}$$

where R is the radial distance from the source.

However, this expression cannot be used here, since it produces sound waves with elevation angles so large, that the PE method is no longer valid. It is also obvious that this formula diverges at the source, positioned at r=0. Instead, the following starting field will be used:

$$q(0,z)=q_0(z-z_s)+C\cdot q_0(z+z_s), \quad \textbf{(2.60)}$$

under the assumption that the ground surface is of a finite impedance and that the source is positioned at $(r,z)=(0,z_s)$.

In eq.**(2.60)**, the reflection coefficient, C, is attained by the expression:

$$C=\frac{Z-1}{Z+1}, \quad \textbf{(2.61)}$$

where Z is the normalized ground impedance.

The function $q_0(z)$ is defined as the starting field for a source at position (r, z)=(0, 0) in an unbounded atmosphere and it satisfies the following relationships:

- $q_0(0,z)=\sqrt{i\cdot k_0}\cdot e^{-\frac{1}{2}k_0^2z^2}$ **(2.62)**, for the case of a narrow-angle propagation and
- $q_0(0,z)=\sqrt{i\cdot k_0}\cdot(1.3717-0.3701\cdot k_a^2z^2)\cdot e^{-\frac{k_a^2z^2}{3}}$ **(2.63)**, for the case of a wide-angle propagation.

Equations **(2.60)**, **(2.62)** and **(2.63)** can be written, replacing every q or q_0 with ψ, according to equation **(2.3)**, since the source is always positioned at r=0.

It is interesting to point out, that the first term of the right-hand side of **(2.60)** represents the direct field of the source, while the second term stands for the field that is reflected by the ground surface.

2.3 Numerical Parameters Study

i. Grid Density

The grid independency of the numerical solution is investigated using a case that corresponds to short range noise propagation and resembles the noise immission from a wind turbine. The following parameters were used for the setup:

- Source position: $(r_s, z_s) = (0, 80)$ [m]
- Receiver position: $(r_r, z_r) = (500, 1.36)$ [m]
- Refraction factor of eq. **(2.49)**: b=0 m/s (non-refracting atmosphere)
- Roughness length: z_0=0.1 m
- Maximum grid height: z^{max}=2000 m for the low frequency and 500 m for the medium and the high frequency.
- Absorbing layer thickness: $50 \cdot \lambda = 50 \cdot \frac{c_0}{f}$, with λ being the wavelength
- Reference speed of sound: c_0=340 m/s
- Absolute temperature: T=293,15 K
- Relative humidity: r_h=70%

The numerical grid is considered uniform and equidistant in the r,z directions ($\Delta r=\Delta z$). To check the grid independency, the relative sound pressure level is plotted against the r-range for different values of the Δr and Δz intervals. Simulations are performed for a low (50 Hz), medium (500 Hz) and high (5000 Hz) frequency. The relative sound pressure level is defined as:

$$\Delta L=10 \cdot \log\left(\frac{|p_c|^2}{|p_{free}|^2}\right), \quad \textbf{(2.64)}$$

where $|p_c|$ is the amplitude of the complex pressure and $|p_{free}|$ is the amplitude of the complex free field pressure.

The free field is the sound field of the source in an unbounded, homogenous atmosphere and can be calculated from the relationship:

$$p_{free}=S \cdot \frac{e^{i \cdot k_0 \cdot R_1}}{R_1}, \quad \textbf{(2.65)}$$

with R_1 being the radial distance from the source and S a constant, equal to 1.

The wide-angle approximation will be considered, along with second-order initial conditions. Unless differently stated, this will hold for the rest of the study as well.

The resulting graphs for the frequencies of 50, 500 and 5000 Hz are presented in Figures 2.3, 2.4 and 2.5 respectively:

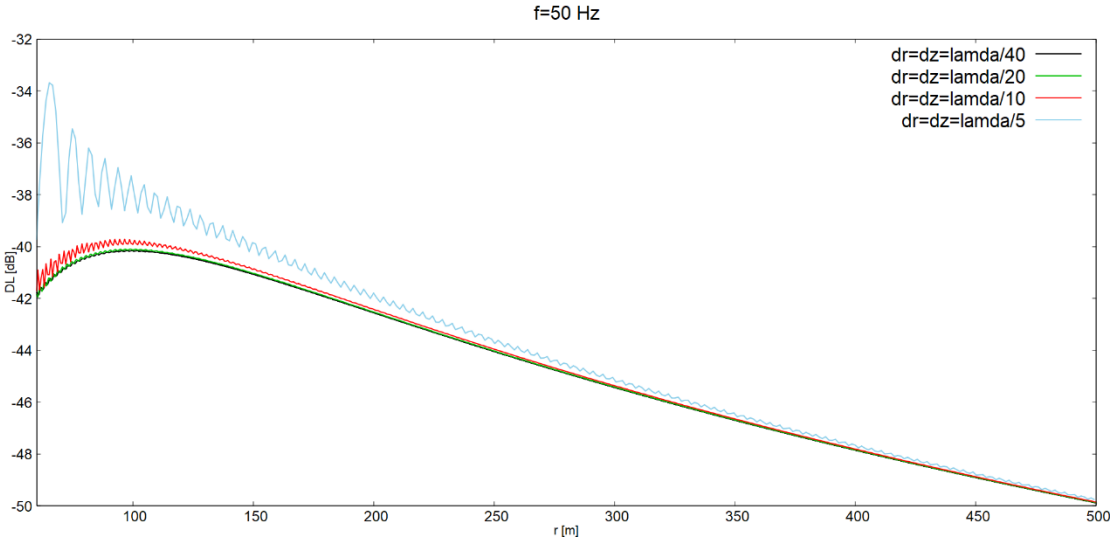

Fig.2.3: The relative sound pressure level along the r-range, for different values of Δr=Δz and for f=50 Hz, as calculated from the developed model.

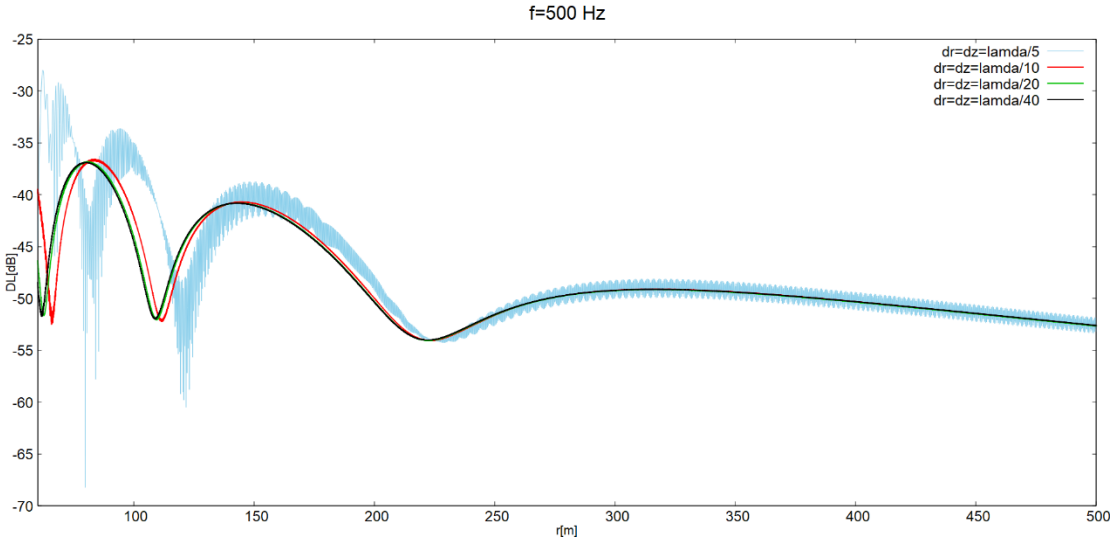

Fig.2.4: The relative sound pressure level along the r-range, for different values of Δr=Δz and for f=500 Hz, as calculated from the developed model.

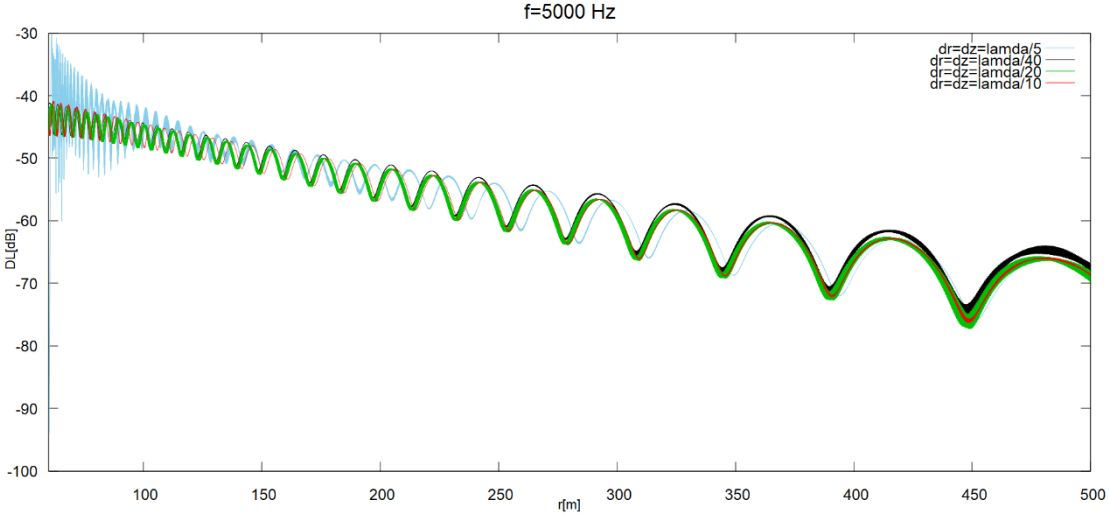

Fig.2.5: The relative sound pressure level along the r-range, for different values of Δr=Δz and for f=5000 Hz, as calculated from the developed model.

It is evident that solution convergence can be achieved for Δr=Δz=λ/20, proving that the developed model is indeed grid-density independent. Yet, for distances far from the source (i.e., for r > 230 m), solution independence can also be acquired for Δr=Δz=λ/10. The rest of the study concerns noise levels at points of long distances from the source, therefore the value Δr=Δz=λ/10 can henceforth be employed.

A closer look in Fig.2.5 (see Fig.2.6) reveals the existence of secondary oscillations in the curves of Δr=Δz=λ/20 or Δr=Δz=λ/40. This reflects the presence of instabilities during the calculations for small interval spacing values, a defect of the developed model. However, for the adopted value Δr=Δz=λ/10, which has proved to be of sufficient accuracy, such instabilities do not occur and this is another reason for choosing this value for future calculations.

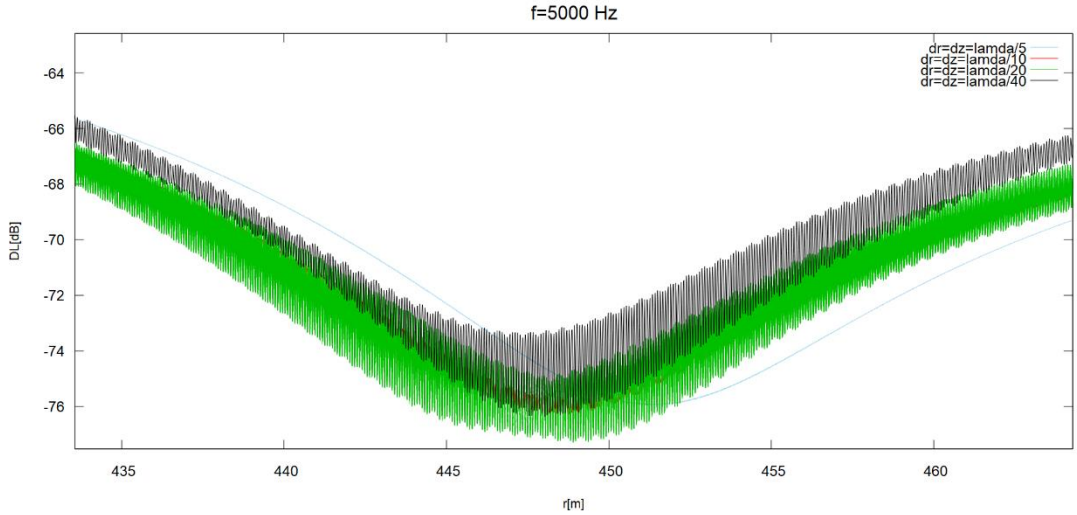

Fig.2.6: The effect of small Δz intervals on the solution stability.

ii. Top grid surface height and absorbing layer thickness

The case of noise propagation in an atmosphere without an absorbing layer is initially examined for a better understanding of its effect on the pressure field. Use of the same parameter values as in the previous section but with the maximum grid height this time varying, results in Fig.2.7 below:

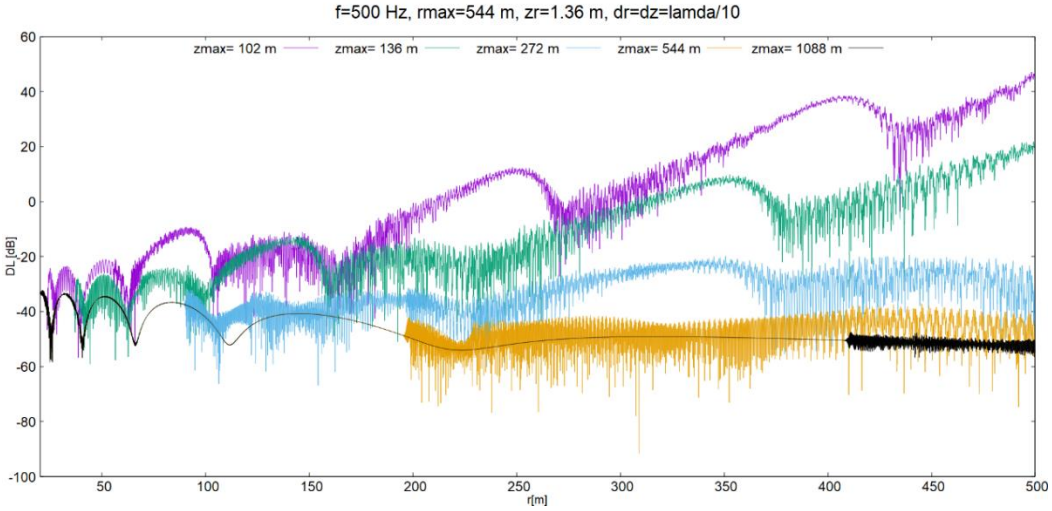

Fig. 2.7: The relative sound pressure level against the r-range for different values of the maximum grid height, z^{max}. The receiver is placed at 1.36 m from the ground.

The lack of an absorbing layer leads to sound wave back-scattering that disturbs the pressure field, especially when the top surface height is low. As can be seen from Fig.2.7, acceptable results were received only for the cases with a grid of a relatively high top surface, namely for z^{max}=544 and 1088 m. Nevertheless, for a source-receiver distance greater than 200 m and 400 m respectively, the pressure field is in those cases influenced as well.

Although placing the receiver about up to 1.5 m above the ground for sound pressure level measurements is common practice, the case of z_r=15×1.36=20.4 m was investigated here as well, representing the possible existence of a tall building in the vicinity of the wind turbine. Studying Fig.2.8 leads to conclusions similar to the previous ones: the sound pressure level is significantly disturbed if the absorbing layer is not considered.

A second remark may also be added: the back-scattering, caused by omitting the absorbing layer at the top grid surface is more intense on the higher grid levels. This accounts for the secondary oscillations, present only in Fig.2.8, where the receiver height is fifteen times the one considered for Fig.2.7, where such disturbances do not seem to appear.

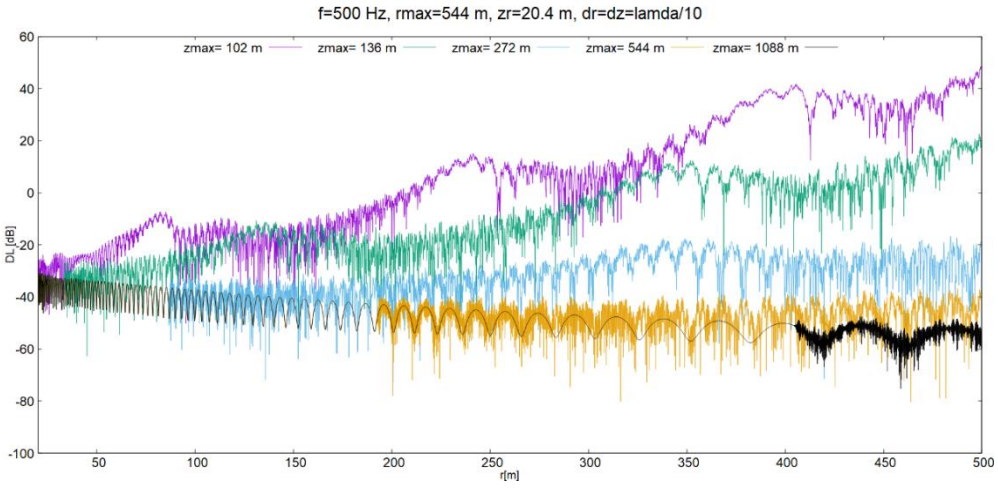

Fig. 2.8: The relative sound pressure level against the r-range for different values of the maximum grid height, z^{max}. The receiver is placed at 20.4 m from the ground.

The above results make clear that the presence of an absorbing layer at the top surface of the grid is necessary for acquiring realistic results. In this paragraph, the values of 10·λ, 20·λ and 50·λ are given to the absorbing layer thickness, along with a gradually decreasing maximum grid height (z^{max} = 136, 272 and 544 m), in order to find the right combination under which the pressure field is unaffected. The rest of the parameters remain the same as in the previous paragraphs. The results are shown in Figures 2.9 up to 2.11:

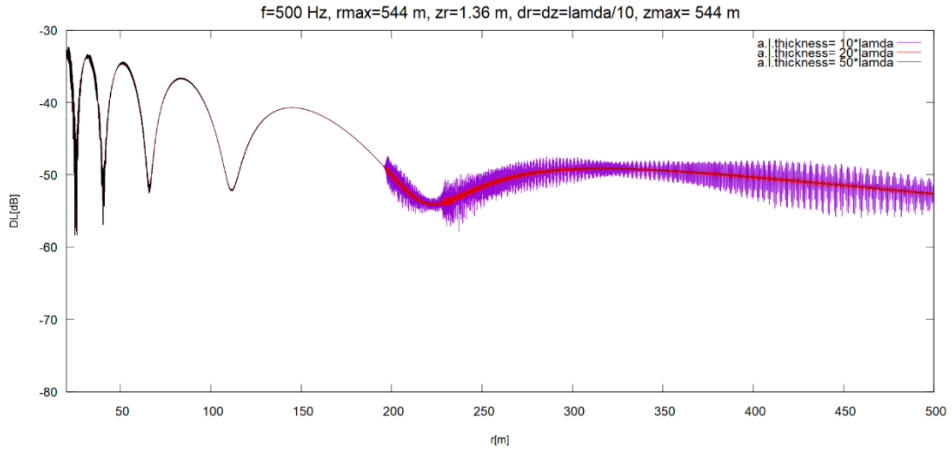

Fig.2.9: The relative sound pressure level against the r-range for maximum grid height, z^{max}=544 m and a varying absorbing layer thickness. The receiver was placed 1.36 m above the ground.

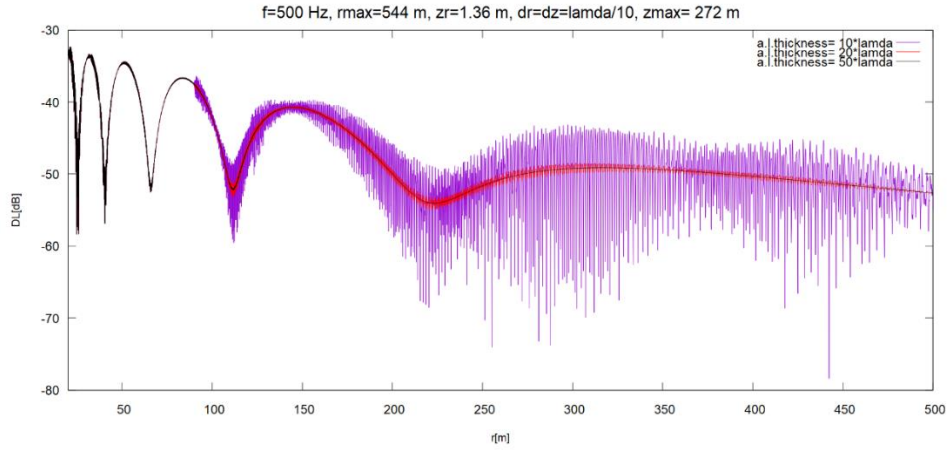

Fig.2.10: The relative sound pressure level against the r-range for maximum grid height, z^{max}=272 m and a varying absorbing layer thickness. The receiver was placed 1.36 m above the ground.

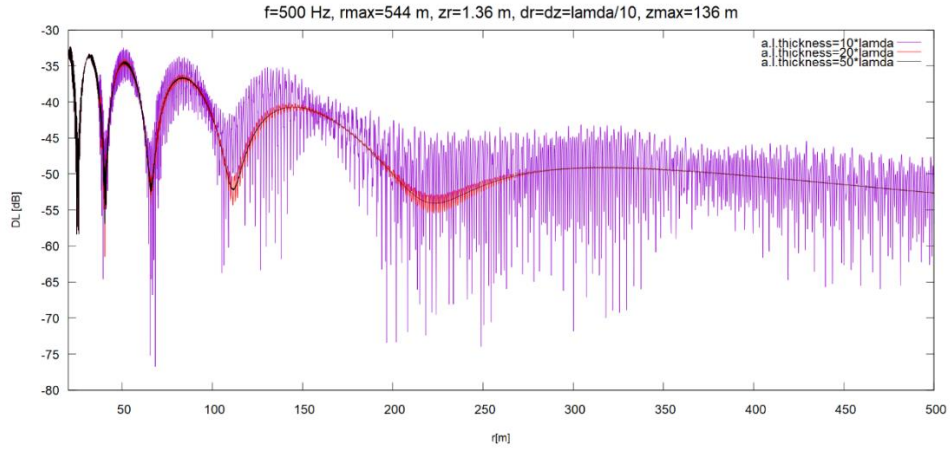

Fig.2.11: The relative sound pressure level against the r-range for maximum grid height, z^{max}=136 m and a varying absorbing layer thickness. The receiver was placed 1.36 m above the ground.

As was expected, although the disturbances are less prominent for grid height equal to 544 m, where the solution converges even for an absorbing layer thickness of 20·λ, they are still distinct in the lower grid heights, if the absorbing layer is not thick enough. Moreover, from Figures 2.9 and 2.10 it is evident that a low maximum grid height can actually be selected with the right choice of an absorbing layer thickness. For example, in Fig.2.11 the intense disturbances caused by the thin absorbing layer of 10·λ completely disappear if the thickness is raised to 50·λ. Therefore, a relatively low, hence computationally less demanding, height can be chosen for the top grid surface, as long as it is combined with an absorbing layer of a suitable thickness.

Another important remark is that, comparing Figures 2.9 up to 2.11 with Fig. 2.7 one realizes that the shape of the resulting curves is completely different. This is attributed to the presence of the absorbing layer that, even for the case where its thickness equals to 10·λ, mitigates sound wave reflection from the top surface of the grid.

The same conclusions can be drawn for the case, where the receiver is placed at z_r=20.4 m from the ground (Figures 2.12-2.14). Although, in a higher receiver position, sound pressure level disturbances are more intense, it is clear from the following plots that the right absorbing layer thickness (generally 50·λ but also 20·λ for the case of z^{max}=544 m) can tone them down considerably.

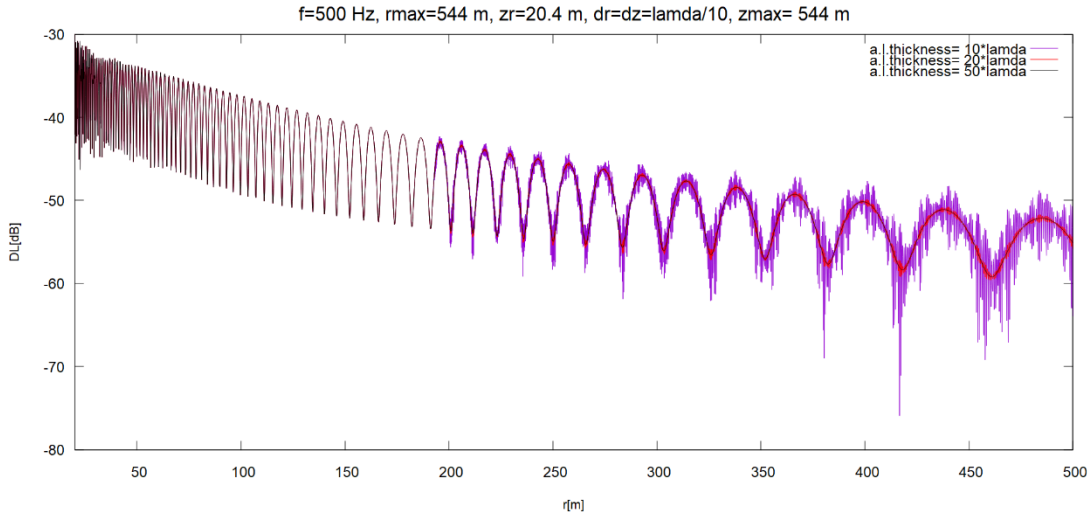

Fig.2.12: The relative sound pressure level against the r-range for maximum grid height, z^{max}=544 m and a varying absorbing layer thickness. The receiver was placed 20.4 m above the ground.

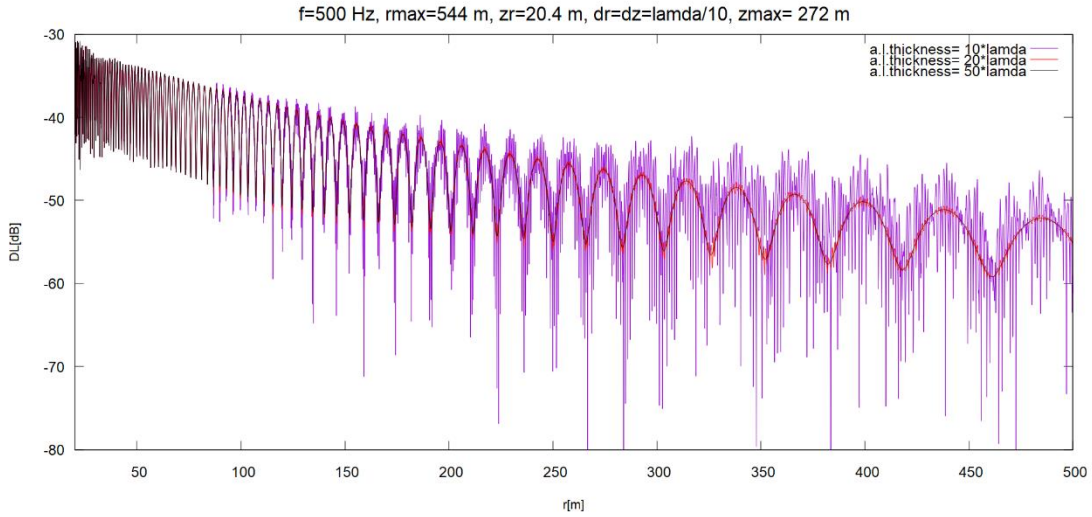

Fig.2.13: The relative sound pressure level against the r-range for maximum grid height, z^{max}=272 m and a varying absorbing layer thickness. The receiver was placed 20.4 m above the ground.

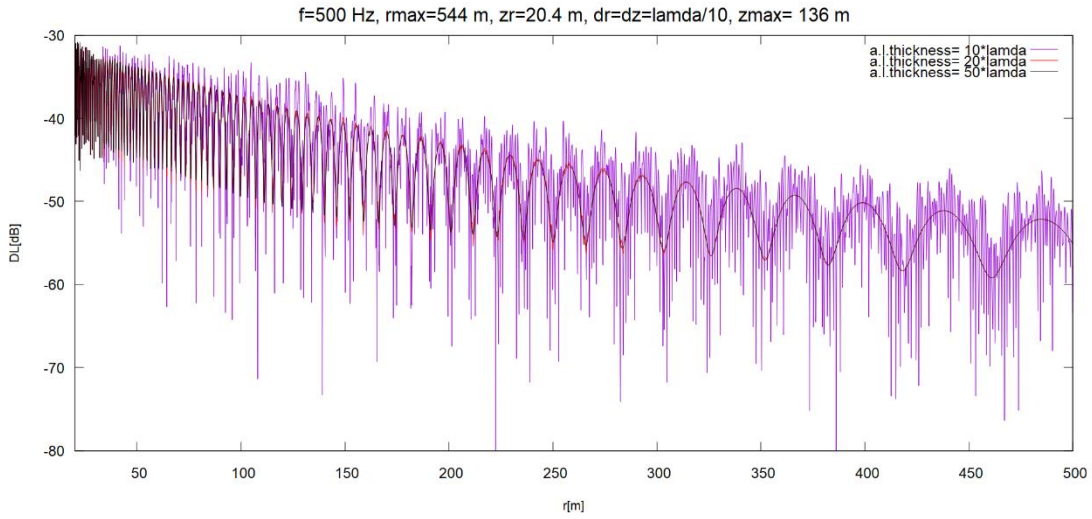

Fig.2.14: The relative sound pressure level against the r-range for maximum grid height, z^{max}=136 m and a varying absorbing layer thickness. The receiver was placed 20.4 m above the ground.

The effect of the absence or presence of an absorbing layer on the top grid surface can be better visualized on a contour plot. For this, the case of z^{max}=272 m was chosen, since, in such a medium height, sound wave reflections are still of significant intensity, hence prominent on these diagrams.

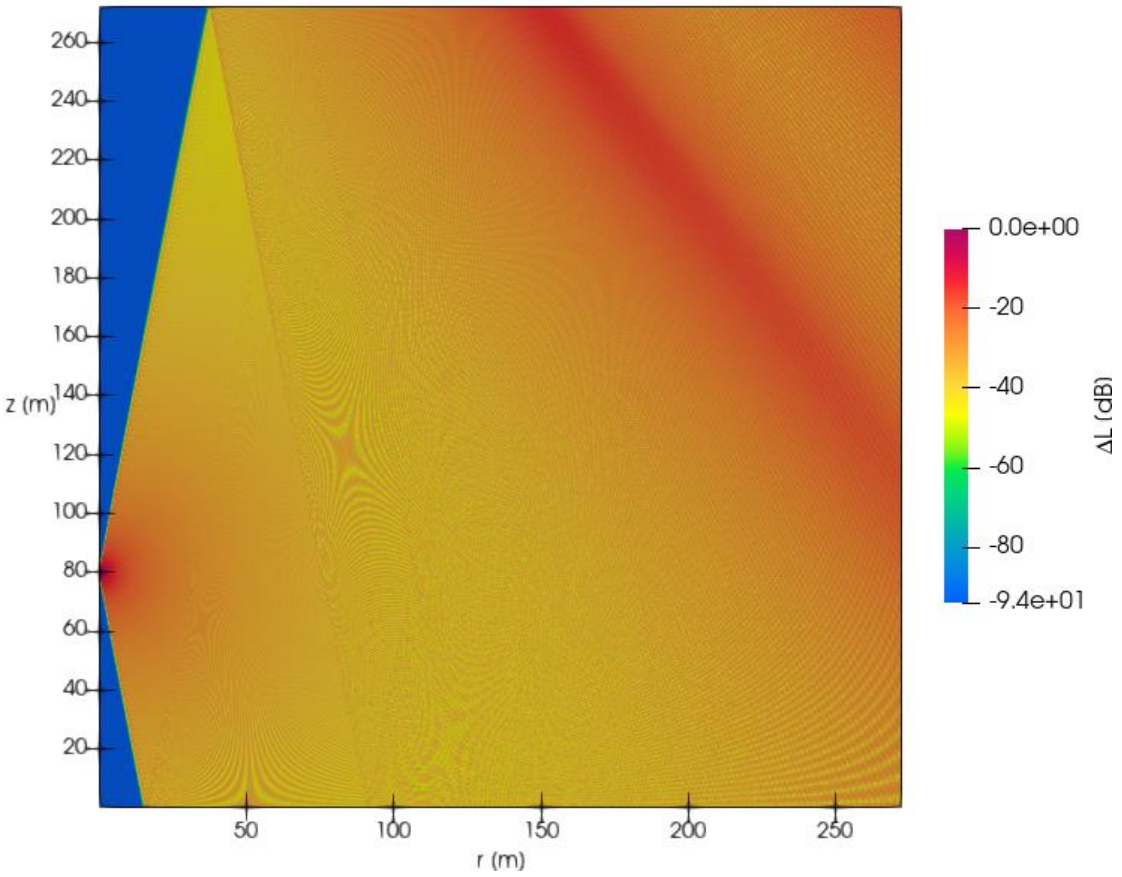

Fig.2.15: The contour diagram for the case of no absorbing layer. The top grid surface is at 272 m from the ground.

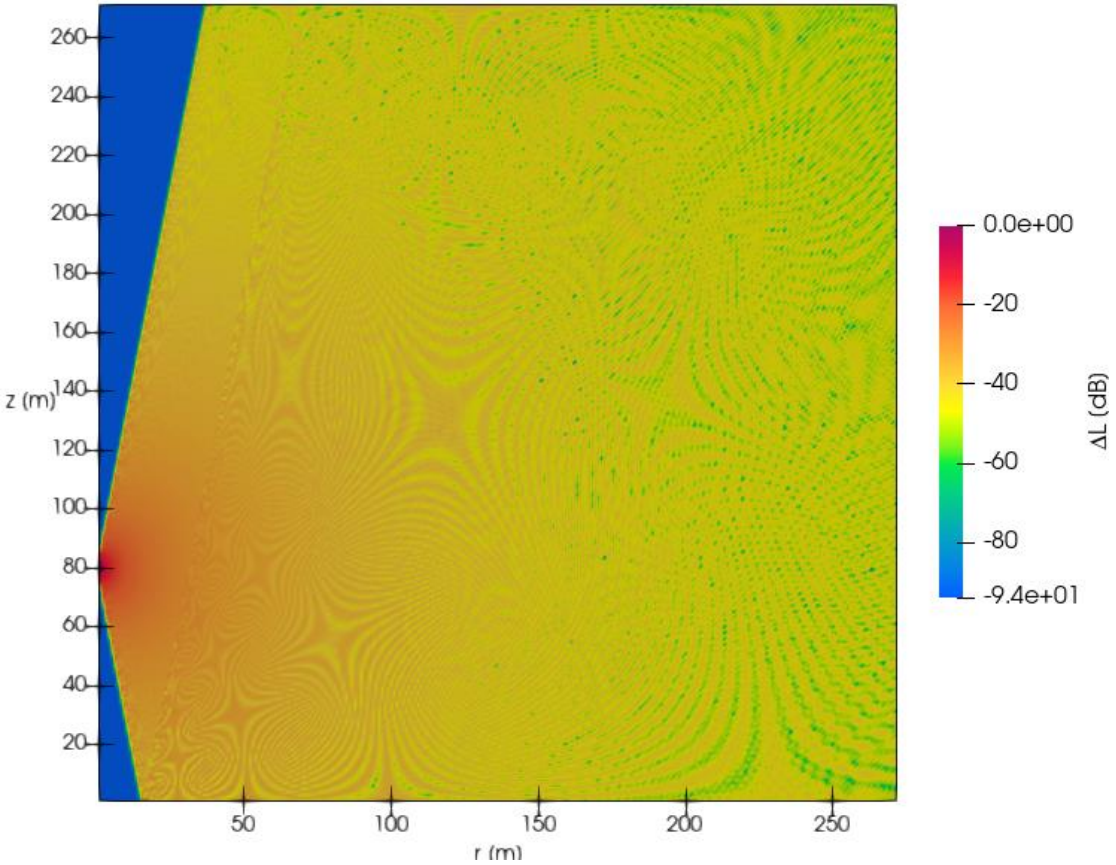

Fig.2.16: The contour diagram for the case of an absorbing layer thickness equal to 10·λ. The top grid surface is at 272 m from the ground.

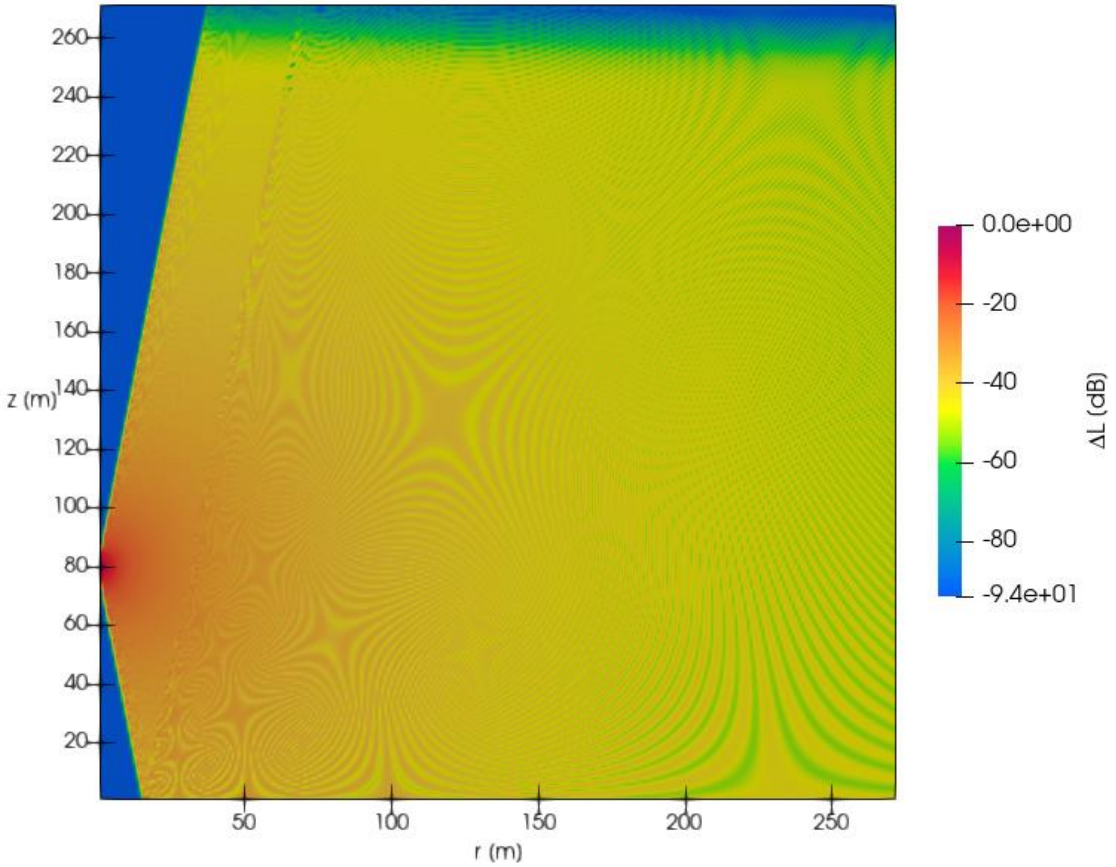

Fig.2.17: The contour diagram for the case of an absorbing layer thickness equal to 50·λ. The top grid surface is at 272 m from the ground.

Comparison between Fig.2.15 and Fig.2.16 or 2.17 shows that even the relatively thin absorbing layer of 10·λ can minimize sound wave reflections. However, since they cannot be completely eliminated, they still affect the sound pressure levels perceived by the receiver. That does not appear clearly on the contour plots but rather on Figures 2.10 and 2.13.

From Figures 2.9 up to 2.14 it is clear that solution convergence is achieved chiefly for absorbing layer thickness equal to 50·λ, a value suggested by Salomons [15, Par.G.9] as well. It would, therefore, be useful to create plots where z^{max} is varying, as in Figures 2.7 or 2.8, but this time with an absorbing layer thickness of this constant value. The results are shown in Figures 2.18 and 2.19 below:

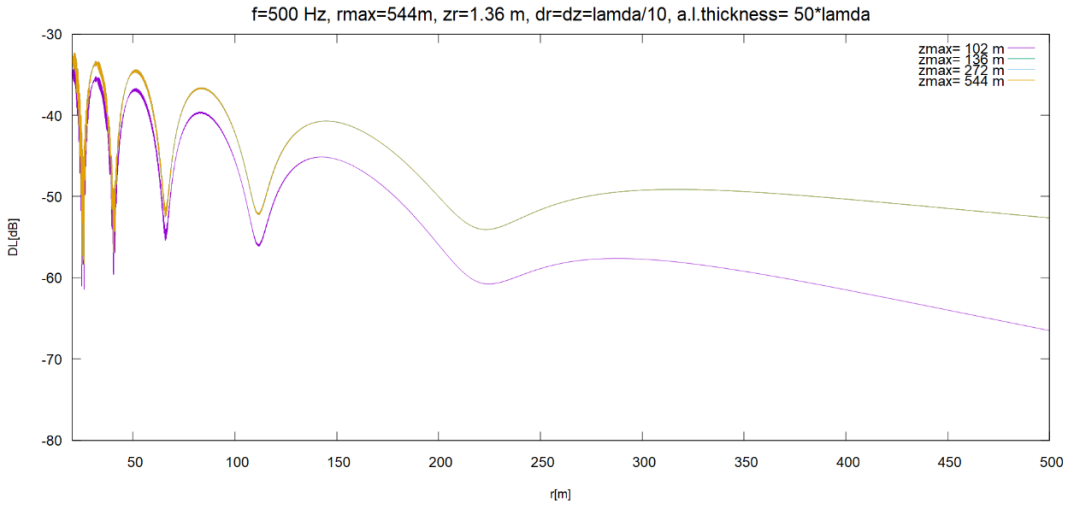

Fig.2.18: The effect of the maximum grid height on relative pressure level for a constant absorbing layer thickness. The receiver was placed 1.36 m above the ground.

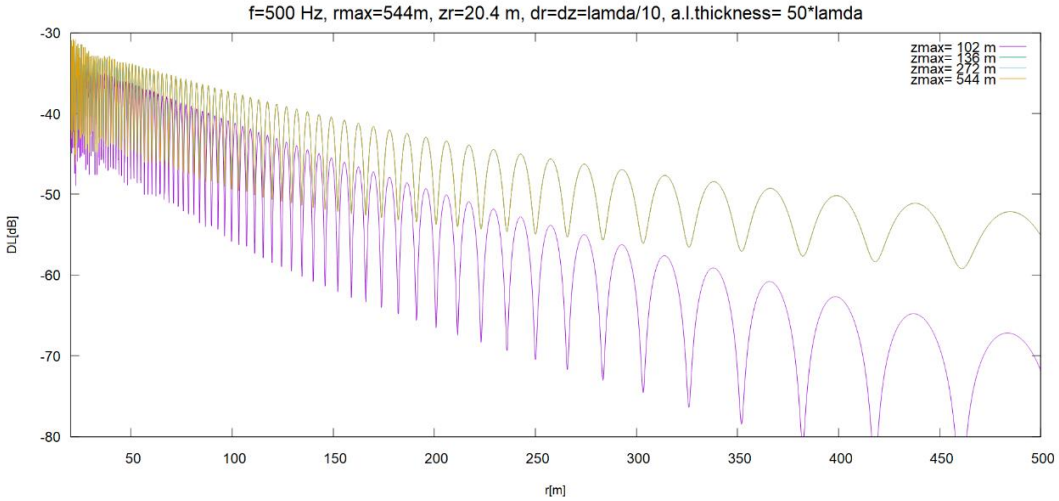

Fig.2.19: The effect of the maximum grid height on relative pressure level for a constant absorbing layer thickness. The receiver was placed 20.4 m above the ground.

It can be seen from both of the above plots that the curves acquired for a top layer height greater than or equal to 136 m are identical. The only case that deviates from the rest is the one where z^{max} is equal to 102 m. This happens because the absorbing layer, beginning from such a low z^{max} and having the thickness of 50·λ=34 m, reaches well below the source height (equal to 80 m), thus interfering with the starting field. Nevertheless, since this is not the case for the value of 136 m, which is still relatively low, even lower than twice the source height, top surface heights as low as this can be trusted to yield reliable results on future calculations, given that they are combined with an adequately thick absorbing layer.

iii. Comparison to narrow-angle approximation results

The values of grid density, maximum grid height and absorbing layer thickness that were selected in the previous paragraphs are now applied to the case in which the narrow-angle approximation is used for calculations. The same parameter values as before are used here as well.

The range diagrams of both approximations in Figures 2.20 and 2.21 appear close to one another but only for long source-receiver distances. A coincidence between the curves was, of course, expected, since a grid specifically chosen for the computationally more demanding wide-angle approximation is bound to apply to the narrow-angle case as well. Nevertheless, for the case in which the receiver is placed higher than usual, as in Fig.2.21, an agreement between results seems to happen a lot further that 500 m. This is unsurprising, since the sound waves that propagate in a narrow angle need a longer horizontal distance to reach a highly-placed receiver. The narrow propagation cone, clearly visible from the contour plot on Fig.2.22, is also responsible for the low-quality results yielded for distances lower than 70 m from the source, since, in this approximation, the calculations begin further from the source.

All in all, for long source-receiver distances and short receiver heights, the narrow angle approximation could provide accurate results and this, thanks to the simpler formulas it is mathematically expressed with, quite efficiently. However, the target of this study is the noise prediction around a wind turbine, a case of short-range propagation while, a restriction to the receiver height is not desired. For these reasons, the more general wide-angle approximation will be applied to all future calculations.

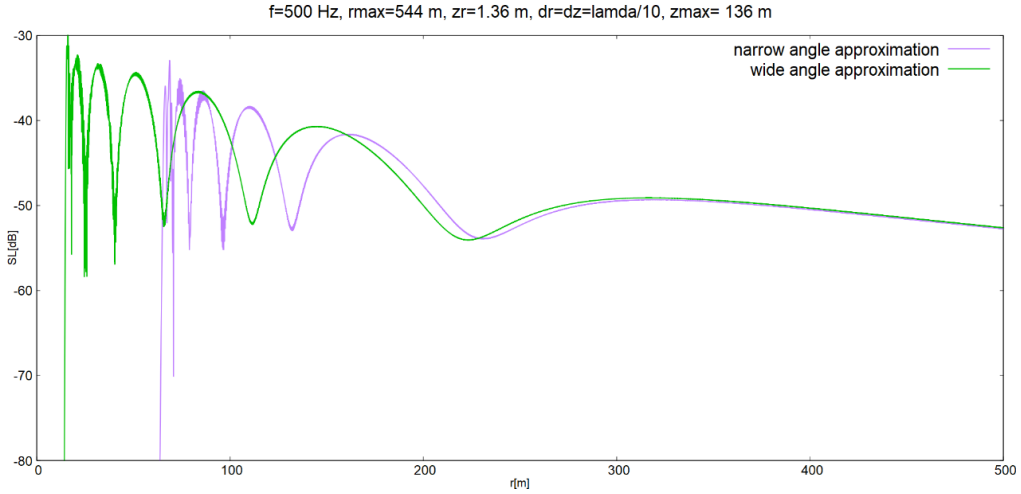

Fig.2.20: Comparison between the relative sound pressure level against the r- range for the narrow and wide-angle approximations. The receiver is placed at a height of 1.36 m from the ground.

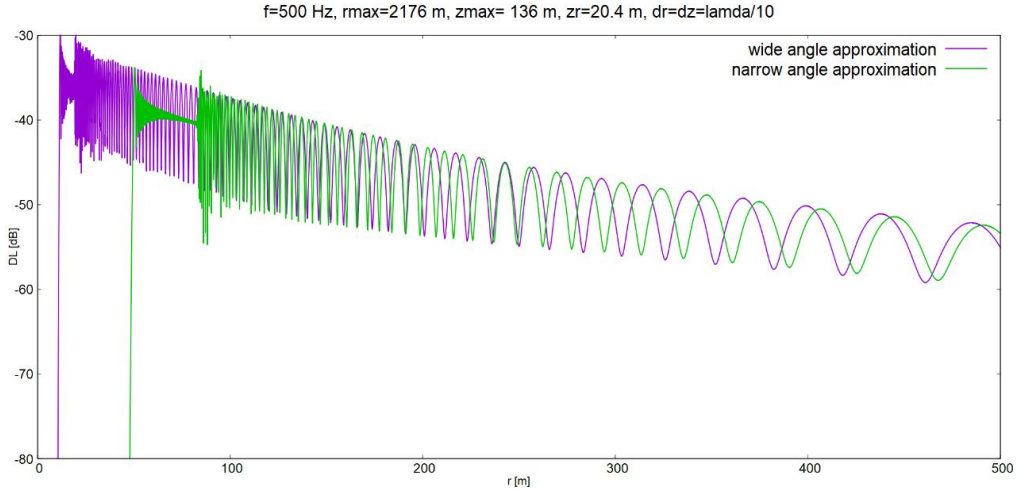

Fig.2.21: Comparison between the relative sound pressure level against the r- range for the narrow and wide-angle approximations. The receiver is placed at a height of 20.4 m from the ground.

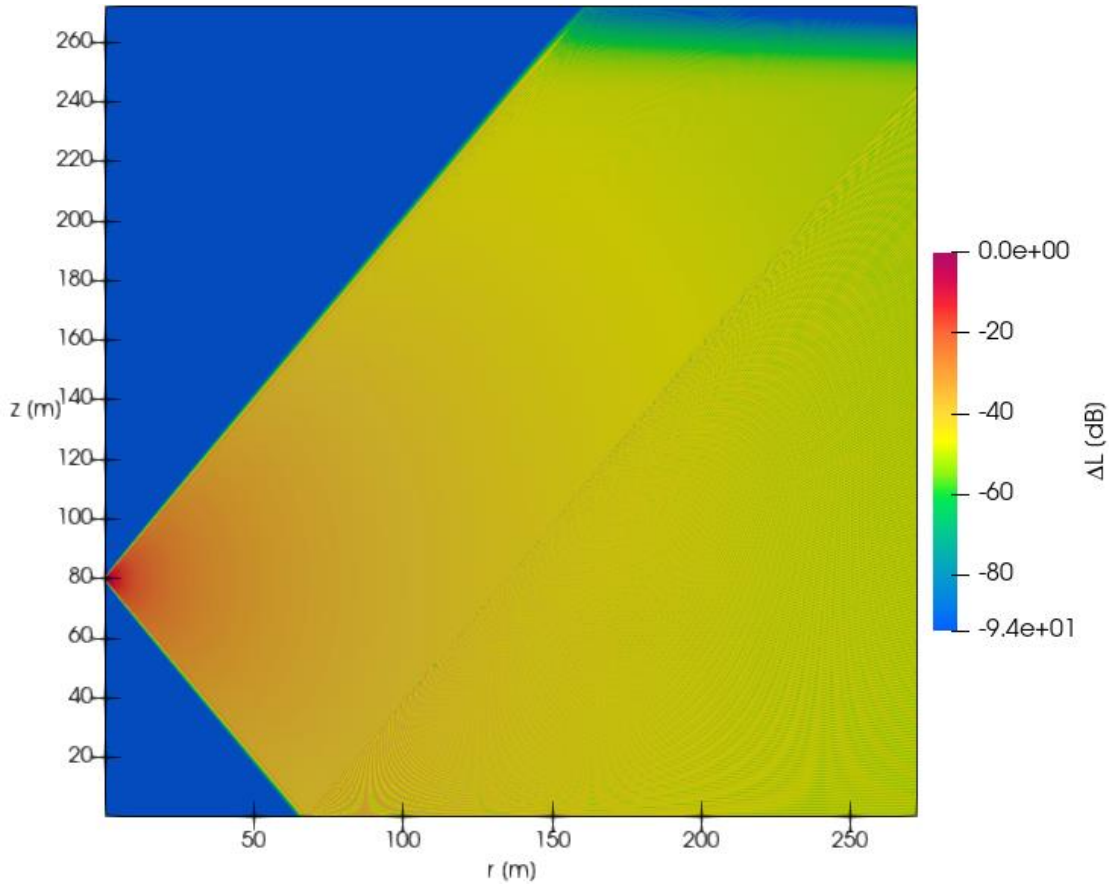

Fig.2.22: The contour plot for the narrow-angle approximation. The absorbing layer thickness is 50·λ and the top grid surface is at z^{max}=272 m from the ground.

3. Results

The present chapter is divided in two sections. In the first one, the developed model is validated by comparing results with the analytical solution and predictions of other methods for a theoretical benchmark case, where the sound speed profile is constant or linear, as well as with experimental data from systematic measurement campaigns. In the second section, the code is applied to real wind turbine cases, using available on-site experimental data.

3.1. Method validation

i. Comparison with the analytical solution and with predictions of other methods

The benchmark cases, studied by Attenborough et al. [44] were determined by the following parameter values:

- Source position: $(r_s, z_s) = (0,5)$ [m]
- Receiver position: $(r_r, z_r) = (200,1)$ [m]
- Absorbing layer thickness: $50 \cdot \lambda = 50 \cdot \frac{c_0}{f}$
- Absolute temperature: T=293,15 K
- Relative humidity: r_h=70%
- Reference speed of sound: c_0=343 m/s

A flat terrain was considered for the calculations, with the normalized impedance expressed, this time, by the following relationship:

$$Z=\frac{\omega \cdot \rho_b(\omega)}{k_b \cdot \rho_0 \cdot c_0}, \tag{3.1}$$

where ω is the angular frequency, ρ_0=1,205 kg/m^3 is the air density at 20°C and $\rho_b(\omega)$ and k_b are parameters that depend on frequency and ground characteristics. For the frequencies of 10, 100 and 1000 Hz that will be dealt with here, Z takes the complex values of 38.79+38.41·i, 12.81+11.62·i and 5.96+2.46·i, respectively.

A linear sound speed profile was employed, as it permits the analytical solution of the wave equation. Its expression is as follows:

$$c(z)=c_0+b \cdot z \tag{3.2}$$

The refraction factor b takes the values of 0 for the case of a wind speed equal to zero, +0.1 m/s for downwind propagation conditions and -0.1 m/s for upwind propagation conditions.

The above parameters were applied to the model in order to compare its results with the ones of the analytical solution and the Fast Field Program model (FFP), presented by Attenborough et al. [44], as well as with the predictions of a ray tracing model, developed by Prospathopoulos and Voutsinas [14]. The quantity used for these comparisons was the Transmission Loss (TL), given by:

$$TL=20 \cdot \log\left[\frac{|p_c(r,z)|}{|p_0|}\right] \tag{3.3}$$

The above relationship is similar to **(2.64)**, with $|p_c|$ being the amplitude of the complex pressure and $|p_0|$ the amplitude of the sound pressure in a free field of radial distance around the source equal to 1 m.

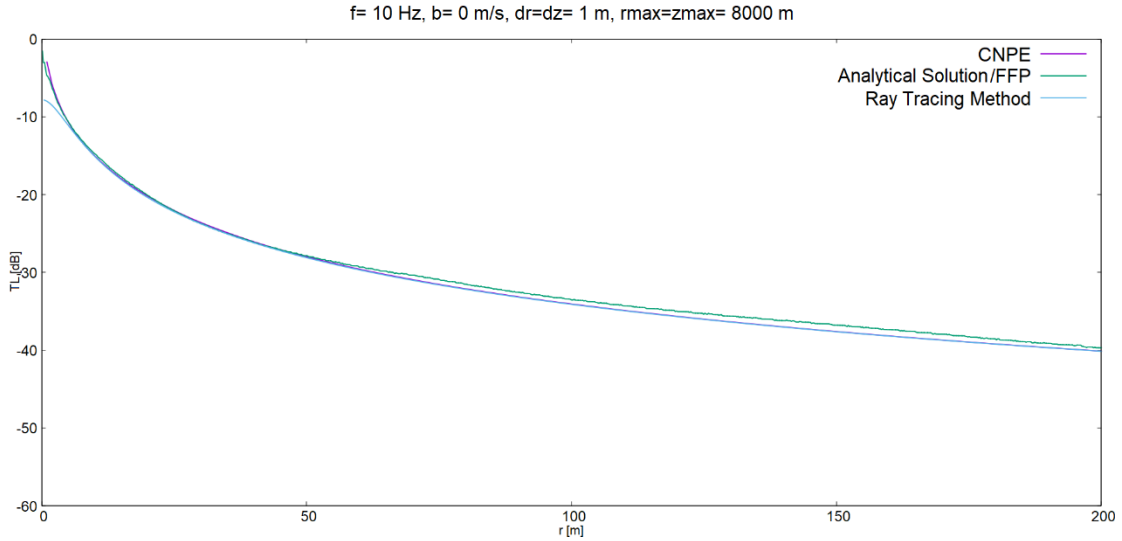

Fig.3.1: Transmission loss against the r-range for the frequency of 10 Hz and a wind speed equal to zero. The solution of the developed CNPE model is compared to the ones of the analytical solution, the FFP method and the ray tracing method.

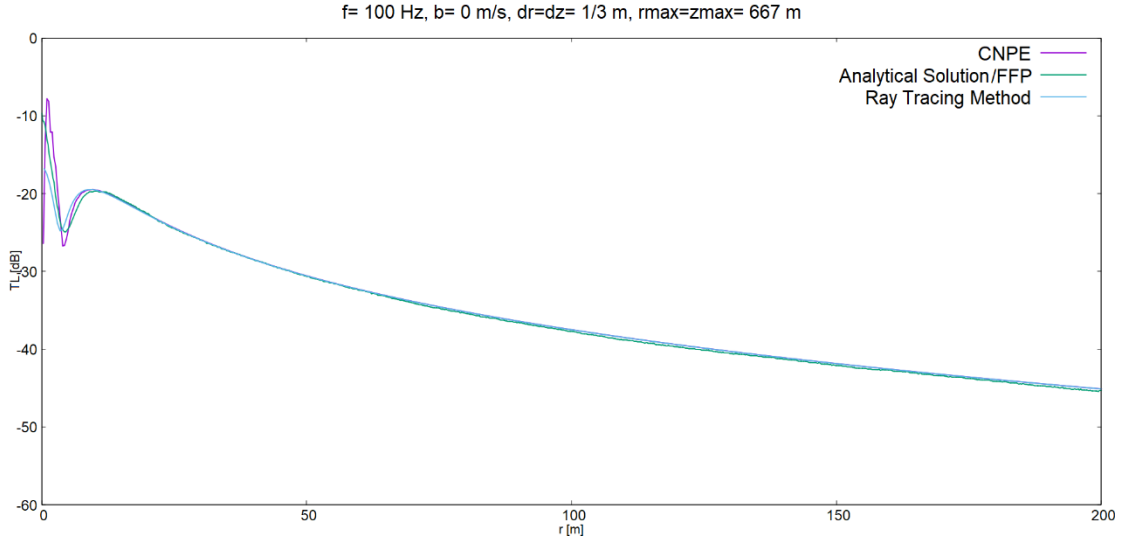

Fig.3.2: Transmission loss against the r-range for the frequency of 100 Hz and a wind speed equal to zero. The solution of the developed CNPE model is compared to the ones of the analytical solution, the FFP method and the ray tracing method.

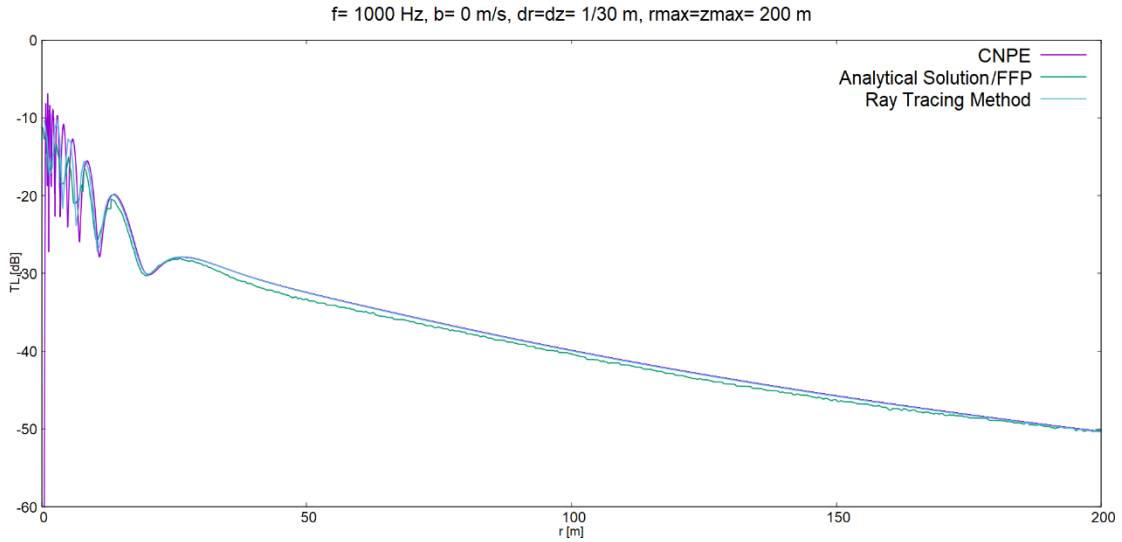

Fig.3.3: Transmission loss against the r-range for the frequency of 1000 Hz and a wind speed equal to zero. The solution of the developed CNPE model is compared to the ones of the analytical solution, the FFP method and the ray tracing method.

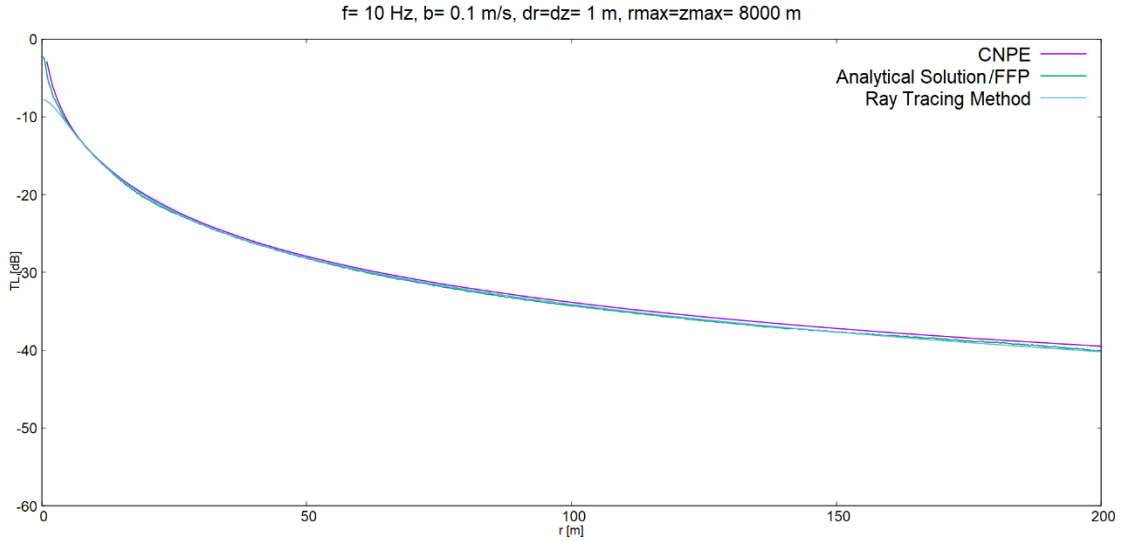

Fig.3.4: Transmission loss against the r-range for the frequency of 10 Hz and downwind propagation conditions. The solution of the developed CNPE model is compared to the ones of the analytical solution, the FFP method and the ray tracing method.

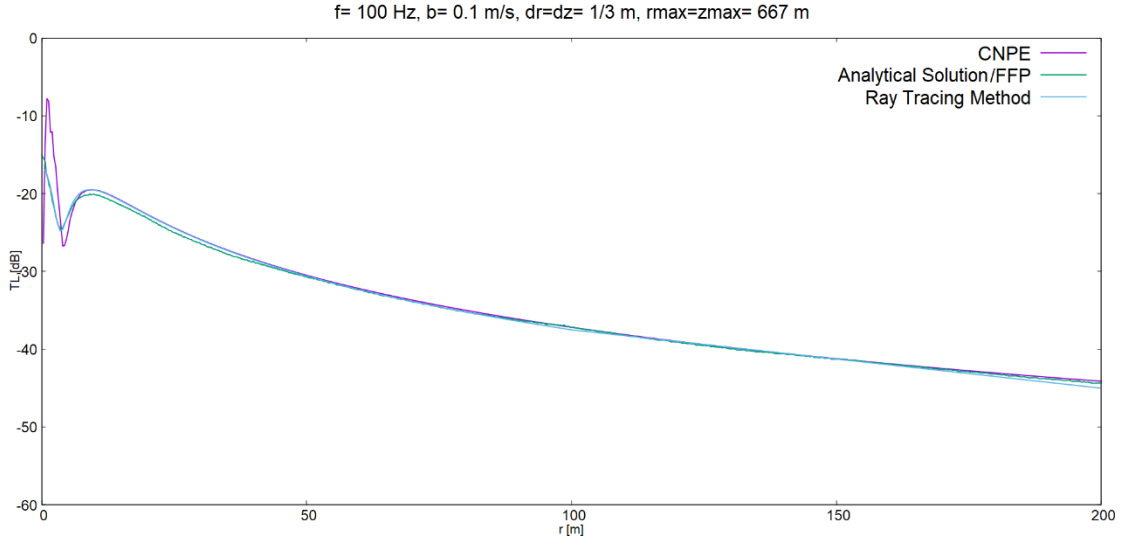

Fig.3.5: Transmission loss against the r-range for the frequency of 100 Hz and downwind propagation conditions. The solution of the developed CNPE model is compared to the ones of the analytical solution, the FFP method and the ray tracing method.

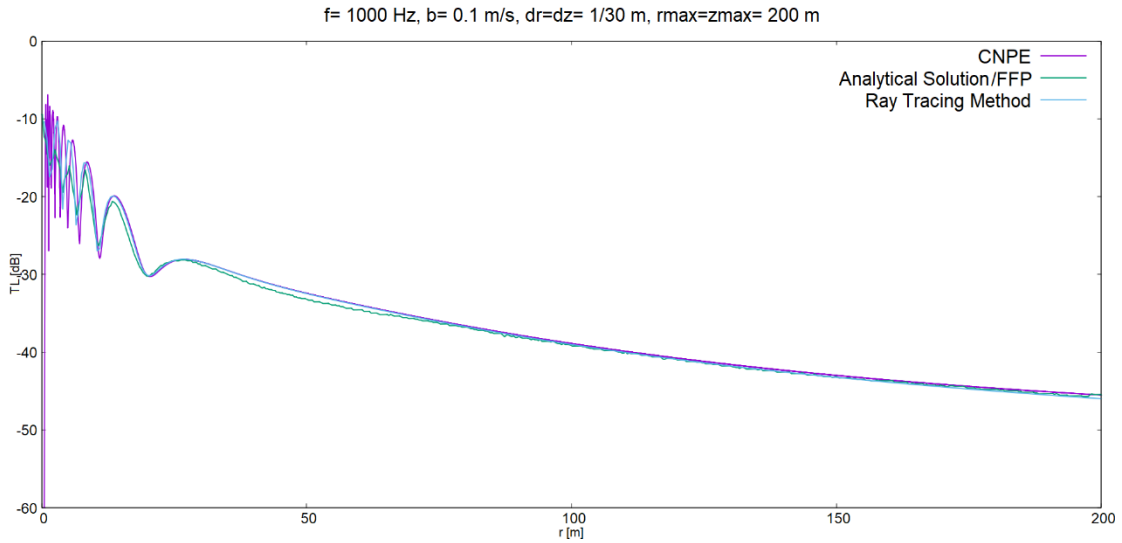

Fig.3.6: Transmission loss against the r-range for the frequency of 1000 Hz and downwind propagation conditions. The solution of the developed CNPE model is compared to the ones of the analytical solution, the FFP method and the ray tracing method.

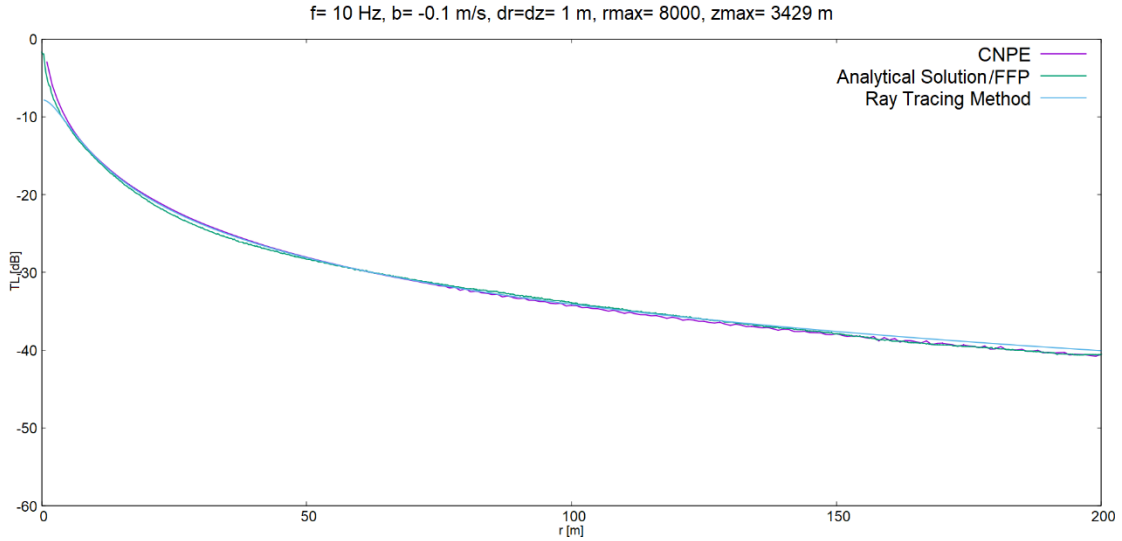

Fig.3.7: Transmission loss against the r-range for the frequency of 10 Hz and upwind propagation conditions. The solution of the developed CNPE model is compared to the ones of the analytical solution, the FFP method and the ray tracing method.

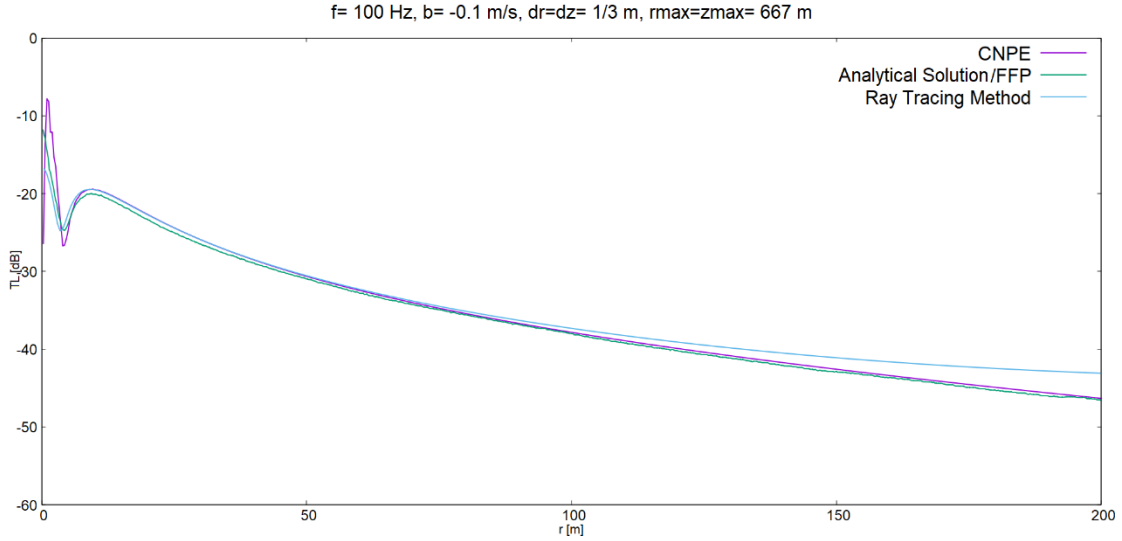

Fig.3.8: Transmission loss against the r-range for the frequency of 100 Hz and upwind propagation conditions. The solution of the developed CNPE model is compared to the ones of the analytical solution, the FFP model and the ray tracing model.

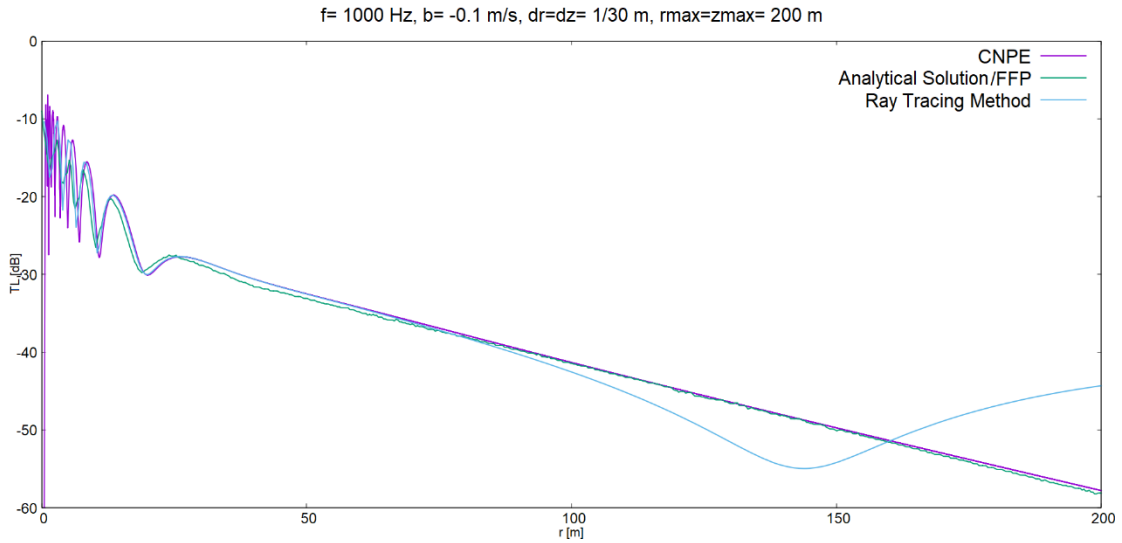

Fig.3.9: Transmission Loss against the r-range for the frequency of 1000 Hz and upwind propagation conditions. The solution of the developed CNPE model is compared to the ones of the analytical solution, the FFP model and the ray tracing model.

For each case of wind propagation condition (zero wind speed, downwind and upwind propagation) and for a low (10Hz), medium (100 Hz) and high (1000 Hz) frequency, the Transmission Loss was plotted against the r-range, creating the Figures 3.1 up to 3.9.

As a general remark on these graphs, one could point out that, for the cases of zero wind speed and downwind propagation, the predictions of the CNPE model, the analytical solution, the FFP model and the ray tracing model are very close to one another. Nevertheless, during upwind propagation, the results from the ray tracing method deviate from the rest, especially as the frequency and the source-receiver distance increase. This divergence is an inherent defect of the ray tracing model, due to the reduced reliability of the geometrical approximation as the receiver approaches the shadow zone [14]. It can be, then, concluded that the results of the CNPE model are reliable and in fair agreement with the ones of Attenborough et al.

ii. Comparison with predictions for the Rock Springs experiment

On July 7th 1990, L'Espérance et al. [45] conducted a series of meteorological and acoustical measurements in a farm field near Rock Springs, Pennsylvania. The frequency range of interest was from 160 up to 3000 Hz, while the measurements were taken for six different source-receiver distances, during six different times of the day, each one of a different wind speed direction.

In this section, the source-receiver distances of 62, 125, 250 and 350 m will be used in the calculations for the cases of slightly upwind (Case 1), essentially upwind (Case 2) and essentially downwind (Case 3) wind propagation conditions. The relative sound pressure level is calculated with the aid of eq. **(3.3)** of Attenborough et al., but this time the reference distance from the source is equal to 4 m. Additionally, applying the same assumptions as L'Espérance et al. for comparison accuracy, the spherical spreading and atmospheric absorption losses were subtracted from the final relative sound pressure level, leaving only the ground effect. While the atmospheric absorption losses can be controlled by changing the input of the model, the spherical spreading losses had to be mathematically removed, as described in the next paragraph.

Spherical spreading losses are expressed as: $A_{s.s.}=10\cdot\log(4\pi r^2)$. In order to cancel their effect on the relative sound pressure level, they must be added to the sound pressure level of both the complex pressure and the pressure of the free field with the following calculations:

- The relative sound pressure level can be written as:

$$\Delta L=10\cdot\log\left(\frac{|p|^2}{|p_{free}|^2}\right)=10\cdot\log|p|^2-10\cdot\log|p_{free}|^2 \qquad \textbf{(3.4)}$$

- The relative sound pressure level without any spherical spreading is related to the one of eq.**(3.4)** as follows:

$$\Delta L_{no\ s.s}=\left[10\cdot\log|p|^2+10\cdot\log(4\pi r^2)\right]-\left[10\cdot\log|p_{free}|^2+10\cdot\log(4\pi\cdot4^2)\right]=\Delta L+10\cdot\log\left(\frac{r^2}{4^2}\right)$$

or else:

$$\Delta L_{no\ s.s}=\Delta L+20\cdot\log\left(\frac{r}{4}\right) \qquad \textbf{(3.5)}$$

The following parameter values were used during calculations, applying the assumptions of L'Espérance et al.:

- Source position: $(r_s, z_s) = (0,1.8)$ [m]
- Receiver height position, r_r: 62, 125, 250 or 350 m
- Receiver range, z_r: 1.75 m
- Absorbing layer thickness: $50\cdot\lambda = 50\cdot\frac{c_0}{f}$
- Reference speed of sound: c_0=343 m/s
- Flow resistivity: $\sigma=15\cdot10^4$ Rayl mks
- Roughness length: z_0=0.01 m
- Relative humidity: r_h=50%
- Ground impedance, Z, from eq. **(2.46)** of Delany and Bazley

Wind speed measurements were conducted at 10 m above the ground, while the temperature was measured at 2 and 10 m above the ground. Table 3.1 contains the measured wind speed (u_0) and temperature differences [T(10 m)-T(2 m)], along with the angle between the wind and the propagation path (θ_w), the Monin-Obukhov length (L) and the temperature at the ground surface (T_0) for each one of the three cases that were dealt with here. These data were used to determine the logarithmic wind speed and temperature profiles by applying the similarity theory [46]. The estimation of T_* and u_*, required for these logarithmic relationships, is achieved through the iterative process, explained by L'Espérance et al. The variation of temperature affects the sound speed, c_0, and, in turn, the effective sound speed profile, computed by eq. **(2.49)**.

Case	**Conditions**	$\mathbf{u_0(10\ m)[\frac{m}{s}]}$	$\mathbf{\theta_w}$ **[°]**	**T(10 m)-T(2 m) [°C]**	**L [m]**	$\mathbf{T_0}$**[°C]**
1	Slightly upwind	1.34	180	-0.10	-150	14.06
2	Essentially upwind	1.47	175	-0.41	-18	17.75
3	Essentially downwind	2.47	-60	1.11	11	19.85

Table 3.1: The meteorological conditions for three of the Rock Springs experiment cases.

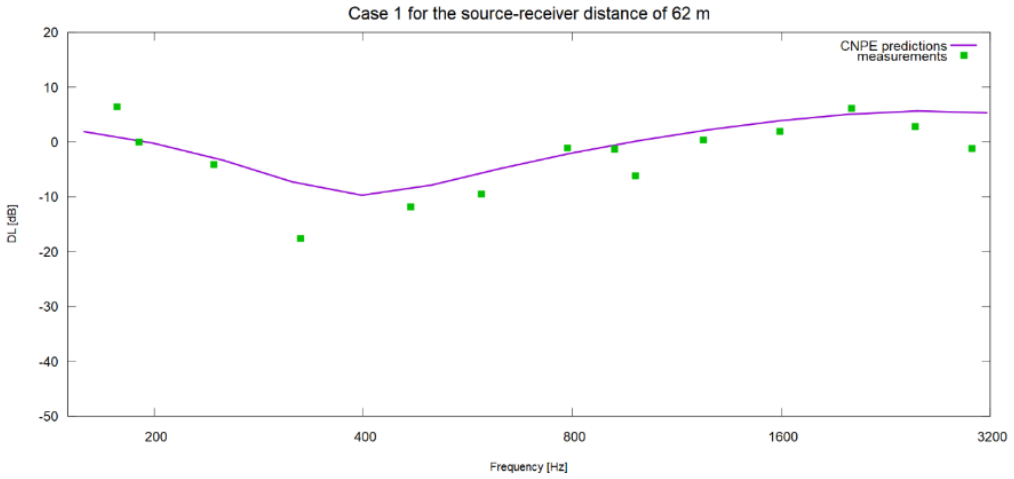

Fig.3.10: The Relative Sound Pressure Lever against a frequency range, as predicted from the CNPE model and measured experimentally for the case of slightly upwind conditions. The source-receiver distance was set to 62 m.

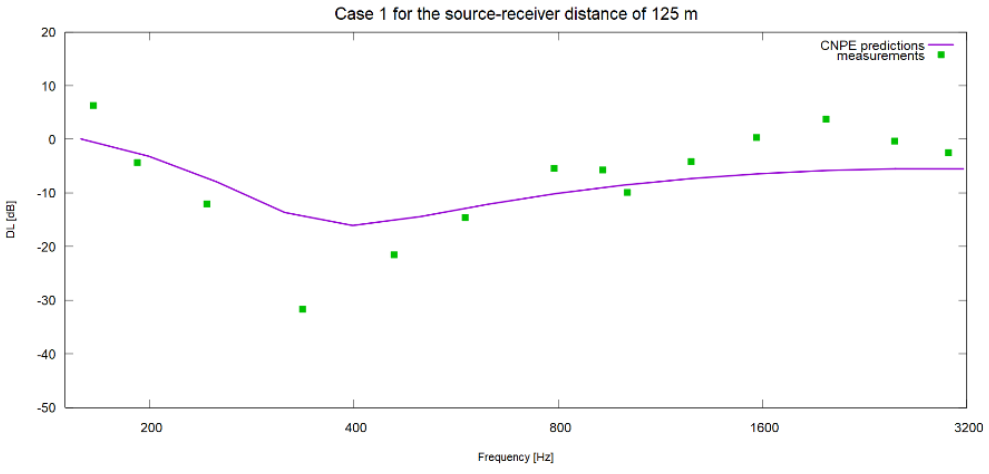

Fig.3.11: The Relative Sound Pressure Lever against a frequency range, as predicted from the CNPE model and measured experimentally for the case of slightly upwind conditions. The source-receiver distance was set to 125 m.

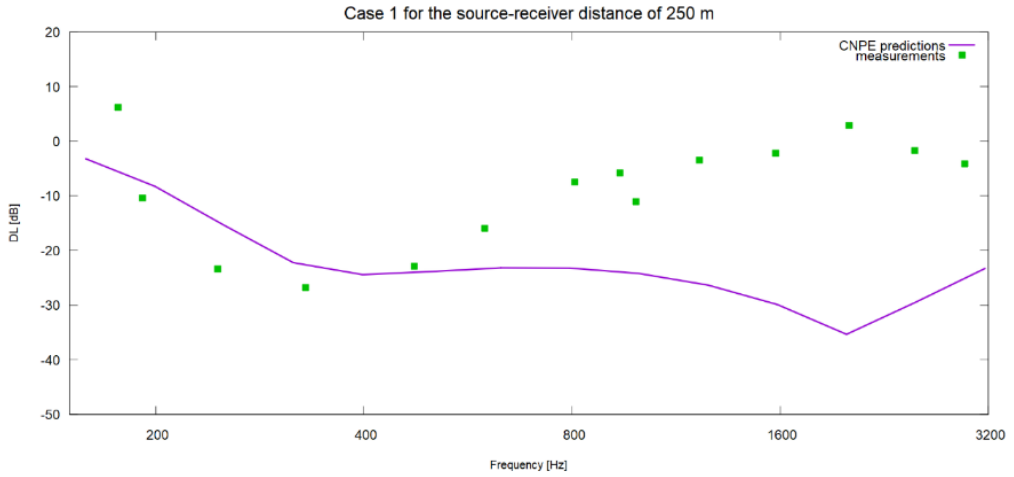

Fig.3.12: The Relative Sound Pressure Lever against a frequency range, as predicted from the CNPE model and measured experimentally for the case of slightly upwind conditions. The source-receiver distance was set to 250 m.

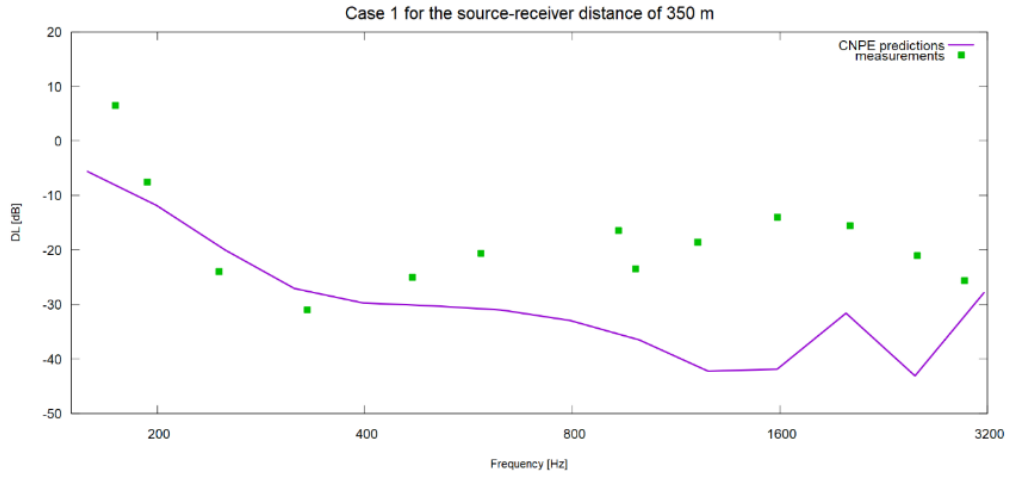

Fig.3.13: The Relative Sound Pressure Lever against a frequency range, as predicted from the CNPE model and measured experimentally for the case of slightly upwind conditions. The source-receiver distance was set to 350 m.

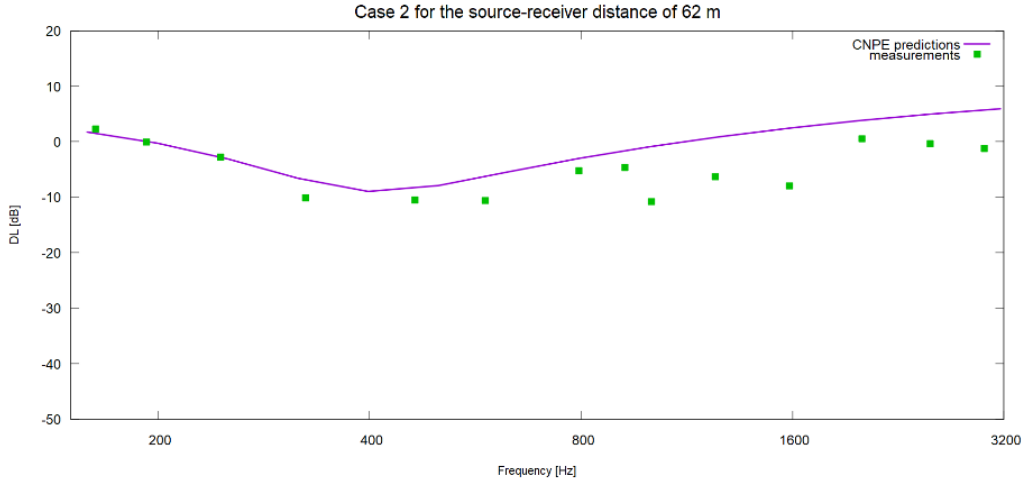

Fig.3.14: The Relative Sound Pressure Lever against a frequency range, as predicted from the CNPE model and measured experimentally for the case of essentially upwind conditions. The source-receiver distance was set to 62 m.

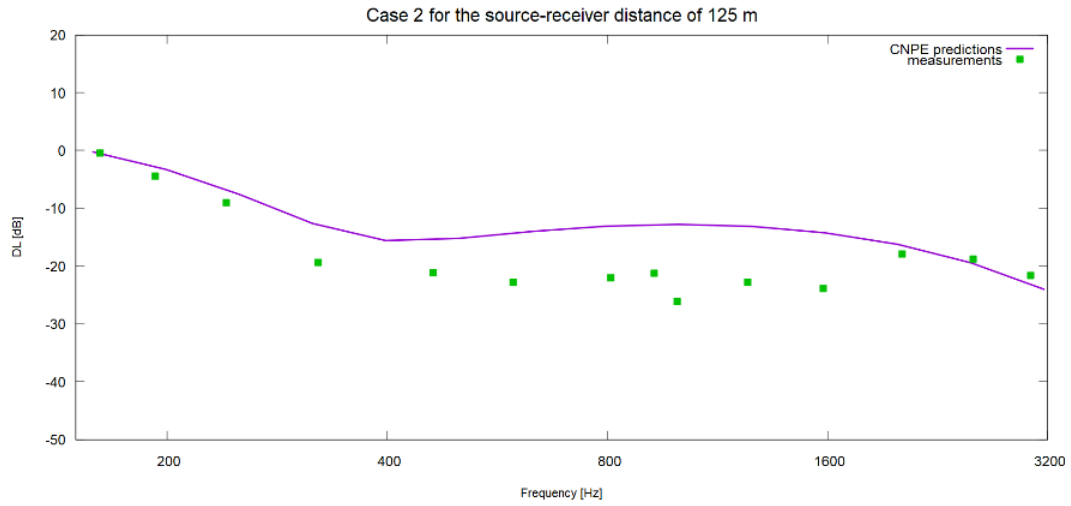

Fig.3.15: The Relative Sound Pressure Lever against a frequency range, as predicted from the CNPE model and measured experimentally for the case of essentially upwind conditions. The source-receiver distance was set to 125 m.

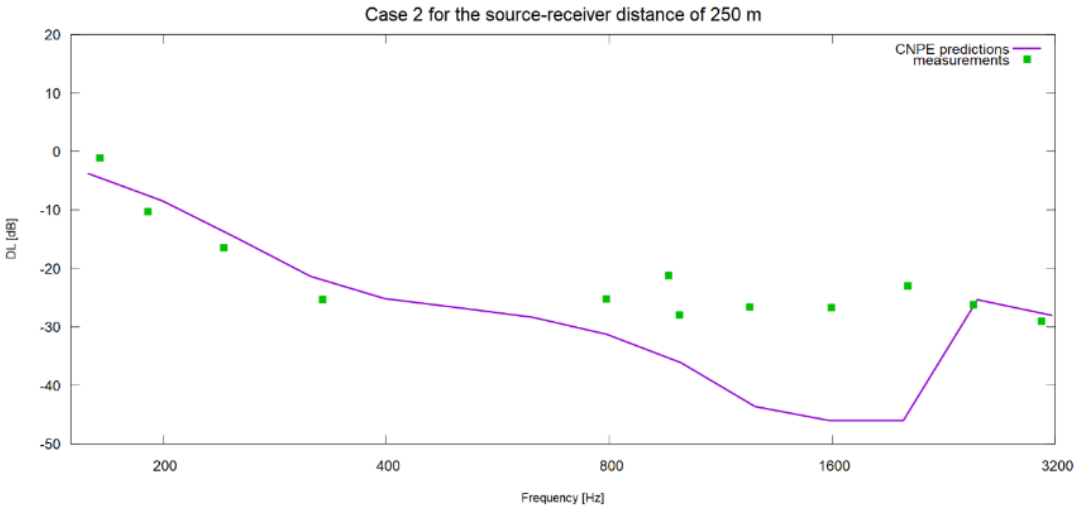

Fig.3.16: The Relative Sound Pressure Lever against a frequency range, as predicted from the CNPE model and measured experimentally for the case of essentially upwind conditions. The source-receiver distance was set to 250 m.

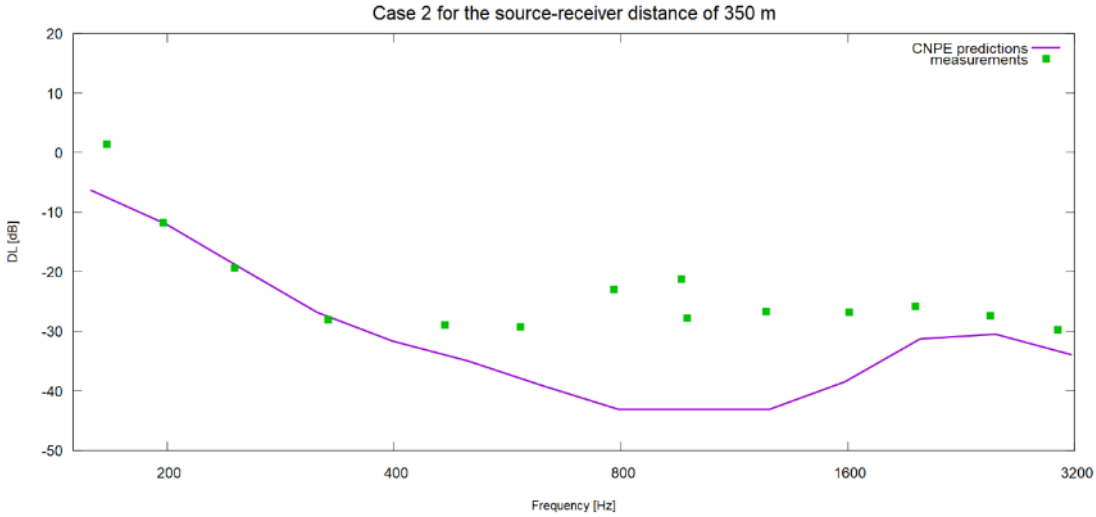

Fig.3.17: The Relative Sound Pressure Lever against a frequency range, as predicted from the CNPE model and measured experimentally for the case of essentially upwind conditions. The source-receiver distance was set to 350 m.

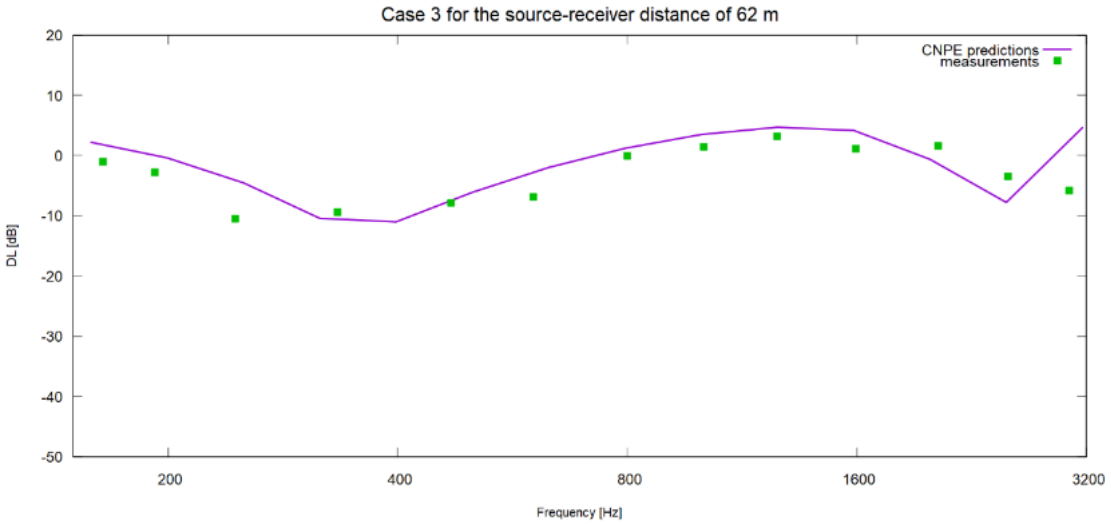

Fig.3.18: The Relative Sound Pressure Lever against a frequency range, as predicted from the CNPE model and measured experimentally for the case of essentially downwind conditions. The source-receiver distance was set to 62 m.

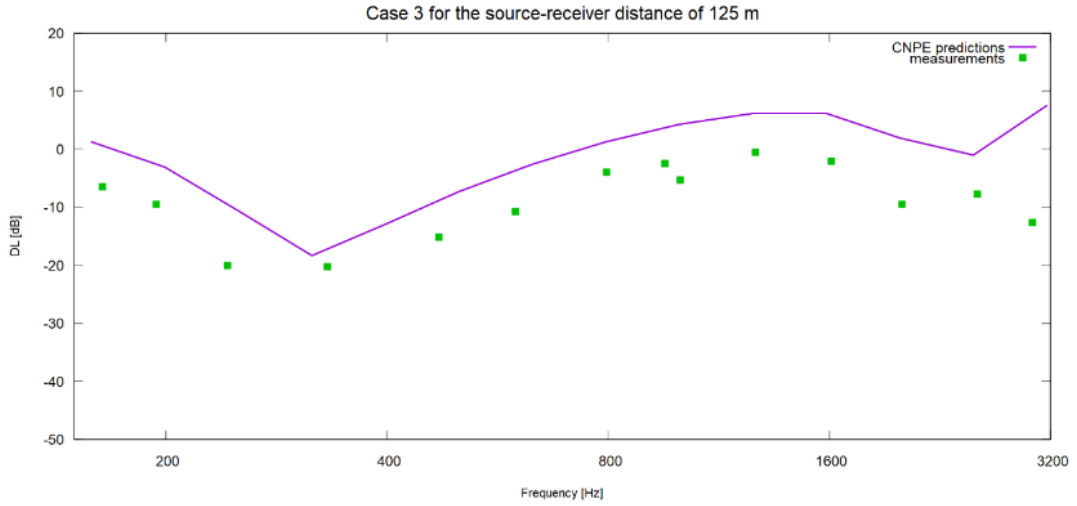

Fig.3.19: The Relative Sound Pressure Lever against a frequency range, as predicted from the CNPE model and measured experimentally for the case of essentially downwind conditions. The source-receiver distance was set to 125 m.

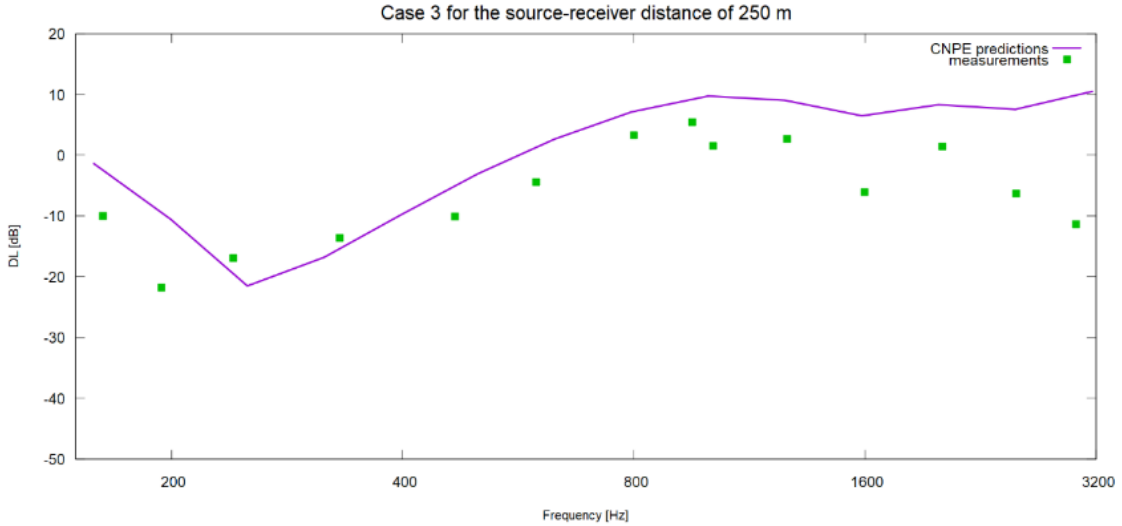

Fig.3.20: The Relative Sound Pressure Lever against a frequency range, as predicted from the CNPE model and measured experimentally for the case of essentially downwind conditions. The source-receiver distance was set to 250 m.

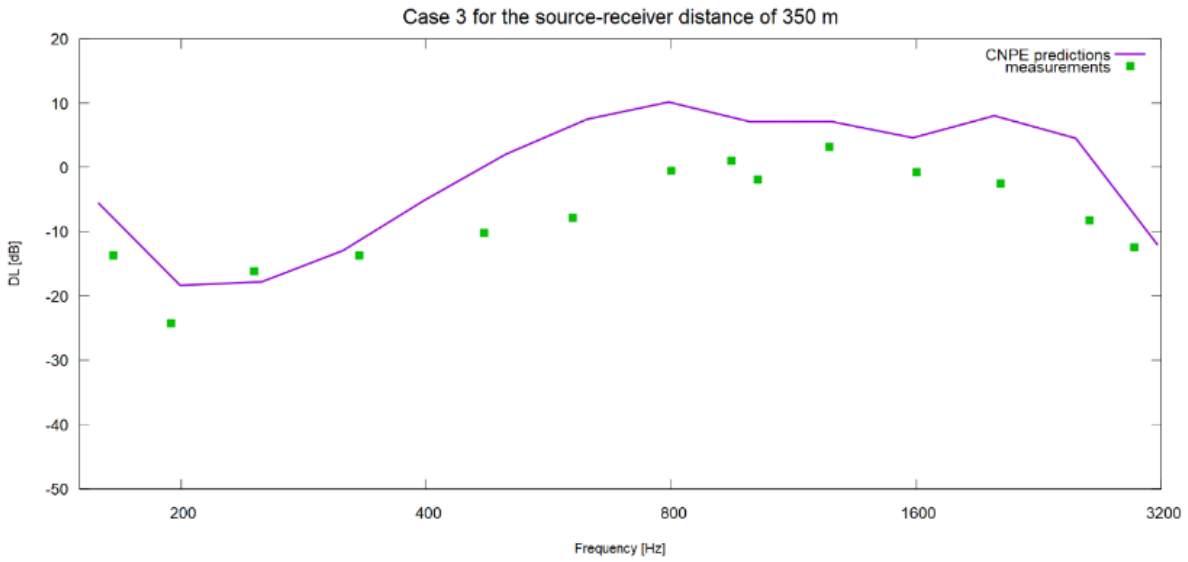

Fig.3.21: The Relative Sound Pressure Lever against a frequency range, as predicted from the CNPE model and measured experimentally for the case of essentially downwind conditions. The source-receiver distance was set to 350 m.

Running each one of the three cases (slightly upwind, essentially upwind and essentially downwind) resulted in Figures 3.10-3.13, 3.14-3.17 and 3.18-3.21 respectively. Studying the plots of Case 1, one can't fail to notice that, although there is a satisfying agreement between the model curves and the measured points for the short distances of 62 and 125 m, this does not happen for the longer distances of 250 and 350 m, especially for frequencies higher than 400 Hz. The same curve-from-point deviation is present in the respective plots of Case 2, this time for frequencies over 800 Hz. The upwind conditions are known to be the most difficult to model, hence the above-mentioned result disagreements. This point can be better understood by studying Figures 3.22 and 3.23, where the most demanding Case 2 (of essentially upwind conditions) is reproduced by the CNPE model, but also by the FFP model and the geometric ray theory model. It is obvious that the FFP and the ray theory models underestimate the final sound pressure levels, especially for high frequencies and long source-receiver distances, despite the linear sound speed profile they employ, which produces smaller sound speed gradients close to the ground. Thus, although all three solutions deviate from the measurement points, the one of the CNPE model seems to be the most accurate.

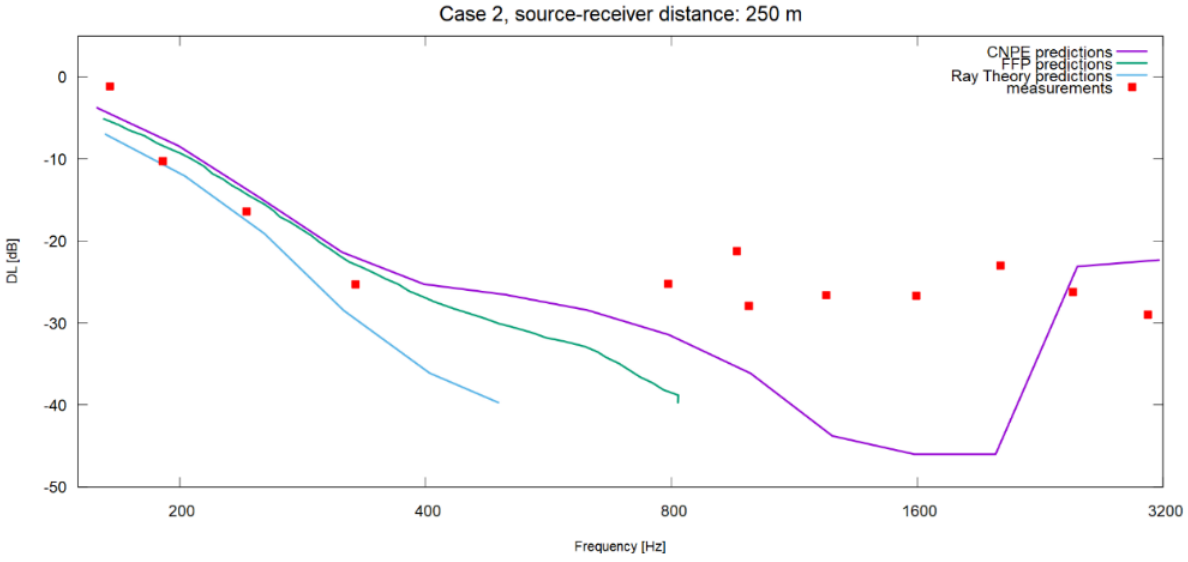

Fig. 3.22: Comparison between the results of the CNPE, FFP and Ray Theory models for Case 2 (essentially upwind conditions) and a source-receiver distance of 250 m.

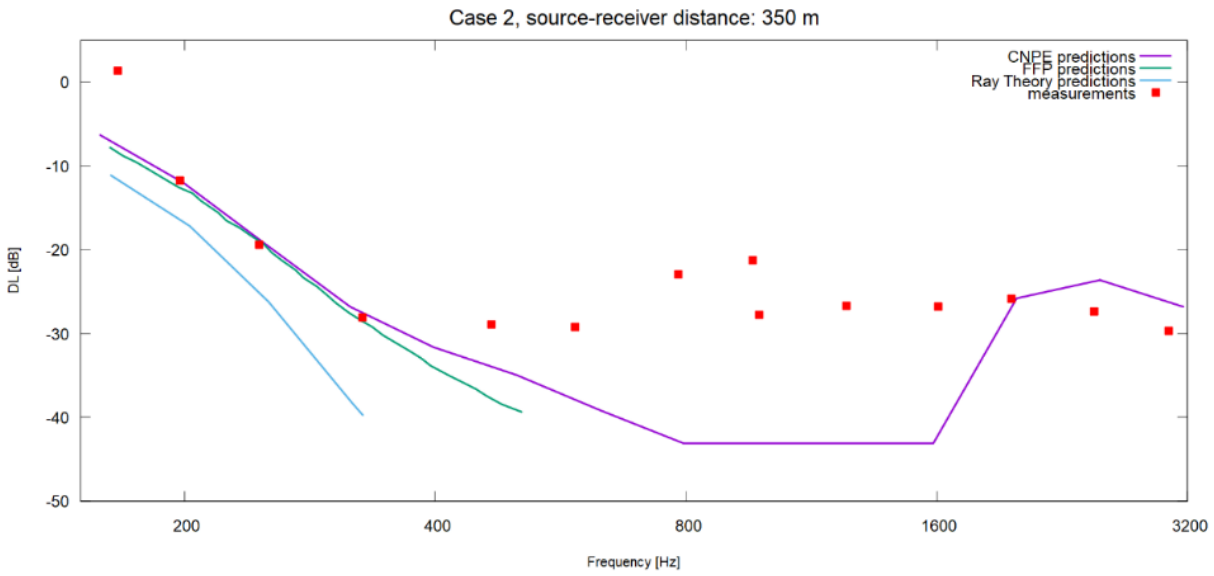

Fig. 3.23: Comparison between the results of the CNPE, FFP and Ray Theory models for Case 2 (essentially upwind conditions) and a source-receiver distance of 350 m.

For the case of essentially upwind conditions, the absorption of sound wave reflections must be checked for the top surface layer of the grid, due to the occurrence of upwards refraction. Studying the respective contour plot (See Fig.3.24), one deduces that the predictions of the CNPE model are reliable.

However, the downwind conditions, here represented by Case 3, favor noise propagation and are, therefore, the ones of interest. The results for this case appear to be in agreement with the measurements for every source-receiver distance and along the entire frequency range (See Figs. 3.18-3.21).

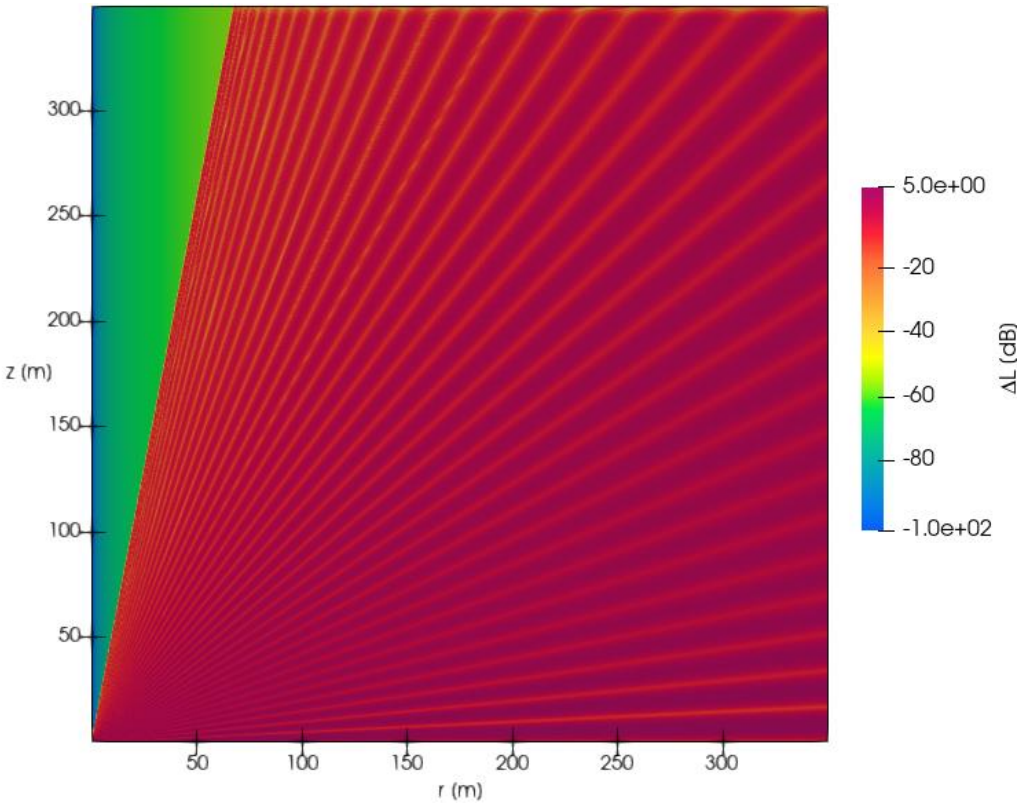

Fig.3.24: The contour plot of Case 2 (essentially upwind conditions) for the frequency of 1995.26 Hz. The absorbing layer thickness is 50·λ and the top grid surface is at z^{max}=350 m from the ground.

iii. Comparison with predictions for the Radlett experiment

Parkin and Scholes [47] conducted a series of measurements of near-ground horizontal sound propagation over a grassland at Radlett, Hertfordshire. The experiments took place during the summer (July to October and mid-April to July) and winter (November to mid-April) of 1964. The following parameter values were considered:

- Source position: $(r_s, z_s) = (0,1.83)$ [m]
- Receiver height, r_r: 19.5, 35, 62, 110, 195, 347, 616 or 1097 m
- Receiver range, z_r: 1.52 m
- Absorbing layer thickness: $50 \cdot \lambda = 50 \cdot \frac{c_0}{f}$
- Roughness length: z_0=0.02 m
- Relative humidity: r_h=30%
- Frequency range of calculations: [50, 4000] Hz
  Especially for the summer measurements
- Absolute temperature: T=303,15 K
- Reference speed of sound: c_0=349.9 m/s
- Flow resistivity: $\sigma=10^5$ Rayl mks
- Especially for the winter measurements
- Absolute temperature: T=278,15 K
- Reference speed of sound: c_0=335 m/s
- Flow resistivity: $\sigma=2 \cdot 10^5$ Rayl mks

While for the summer experiments the eq. **(2.46)** of Delany and Bazley was used for the calculation of ground impedance, the slightly more complex eq. **(3.6)** was employed for the modeling of the ground effect during wintertime:

$$Z=Z_c \cdot \coth(-i \cdot k_b \cdot d), \quad \textbf{(3.6)}$$

thus simulating the ground as a thin layer of thickness d=0.03 m, over a semi-infinite hard material. In eq. **(3.6)**, Z_c is the complex normalized ground impedance, from eq. **(2.46)**, and k_b the propagation wave number, given by:

$$k_b=\alpha+i \cdot \beta, \quad \textbf{(3.7)}$$

with α and β being functions of the wave number at the ground surface, k_0, as follows:

$$\alpha=k_0 \cdot \left[1+10.8 \cdot \left(\frac{1}{1000} \cdot \frac{f}{\sigma}\right)^{-0.7}\right], \quad \textbf{(3.8)}$$

and

$$\beta=k_0 \cdot \left[10.3 \cdot \left(\frac{1}{1000} \cdot \frac{f}{\sigma}\right)^{-0.59}\right], \quad \textbf{(3.9)}$$

For all calculations, the logarithmic sound speed profile, described in eq. **(2.49)** was considered. For the case of downwind propagation conditions, the refraction factor, b, was calculated assuming a wind speed equal to 4.5 m/s at z=10 m, namely:

$$u=b \cdot \ln\left(1+\frac{z}{z_0}\right) \Rightarrow 4.5=b \cdot \ln\left(1+\frac{10}{0.02}\right) \Rightarrow b=0.72 \text{ m/s} \quad \textbf{(3.10)}$$

In the case of a zero wind speed, b was, of course, considered equal to zero.

The quantity used for results comparison is the "Sound Pressure Level Attenuation", defined as the measured sound pressure level, reduced by the sound pressure level of the first receiver (19.5 m away from the source). Atmospheric absorption and spherical spreading losses were removed from the final results in the same way as described in Sec.3.1.ii. Therefore, the following equation was used for the calculation of the sound pressure level attenuation:

$$\Delta L = 10 \cdot \log\left(\frac{|p|^2}{|p_{19.5}|^2}\right) + 20 \cdot \log\left(\frac{r}{19.5}\right), \qquad \textbf{(3.11)}$$

where $|p_{19.5}|^2$ is the complex pressure amplitude at 19.5 m from the source.

The cases of a source-receiver distance equal to 62, 110, 195 and 347 m were reproduced here with the aid of the CNPE model, using both winter and summer data. The final results, presented in Figures 3.27 up to 3.32 for the summer cases and 3.33 up to 3.40 for the winter cases are in fair agreement with the site measurements.

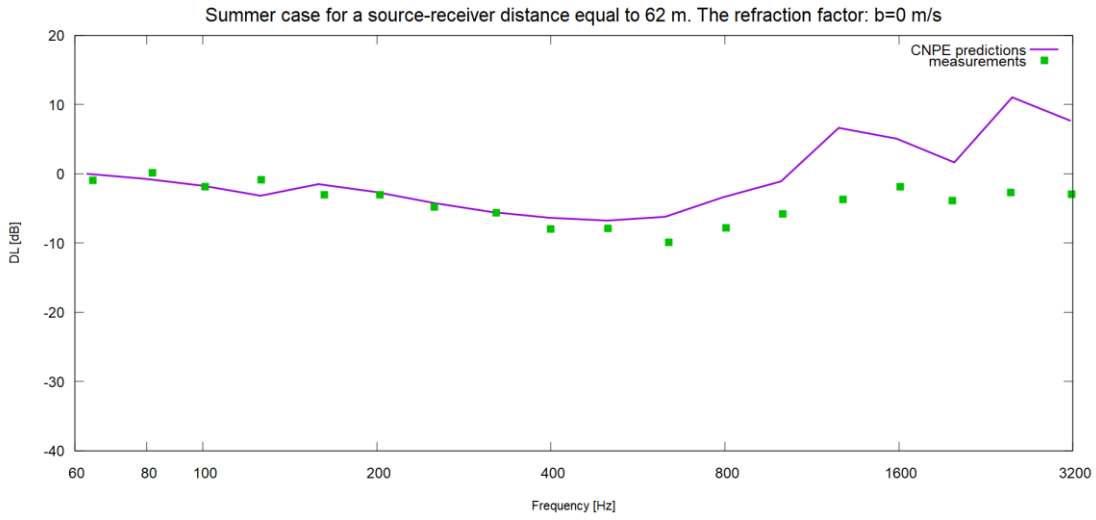

3.25: The Sound Pressure Level Attenuation, calculated from the CNPE model for the summer case. The source-receiver distance is equal to 62 m and the wind speed is equal to zero.

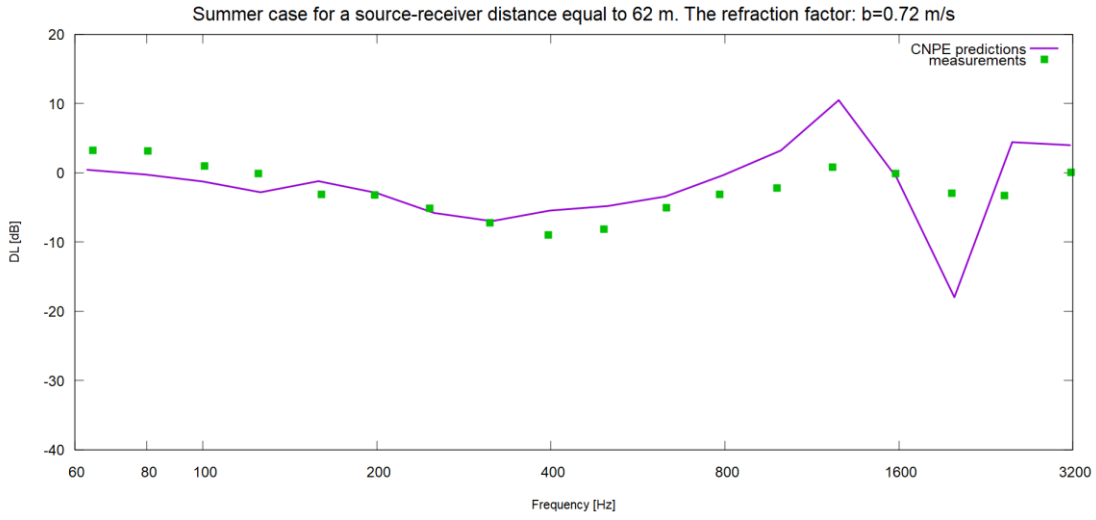

3.26: The Sound Pressure Level Attenuation, calculated from the CNPE model for the summer case. The source-receiver distance is equal to 62 m and the wind direction is downwind.

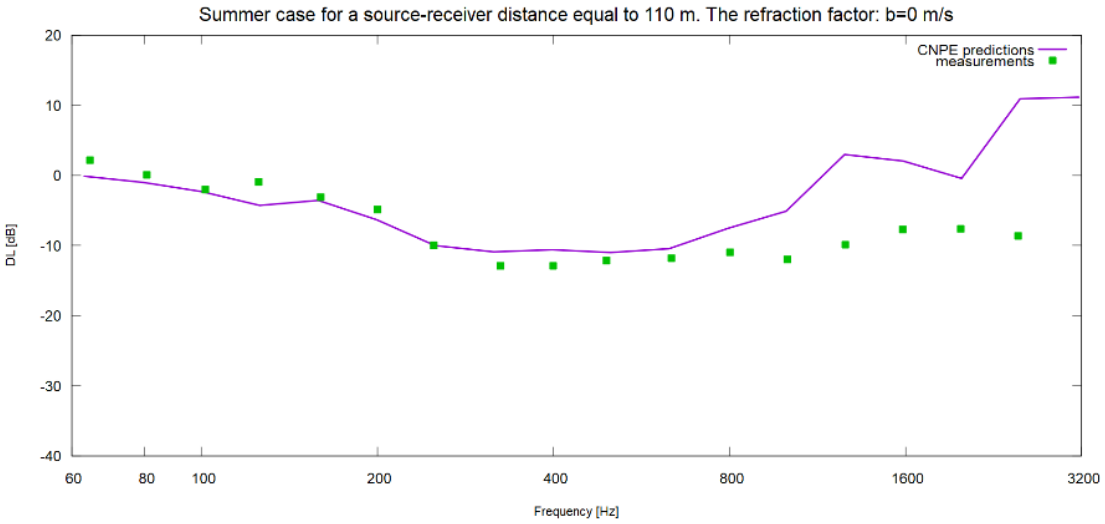

3.27: The Sound Pressure Level Attenuation, calculated from the CNPE model for the summer case. The source-receiver distance is equal to 110 m and the wind speed is equal to zero.

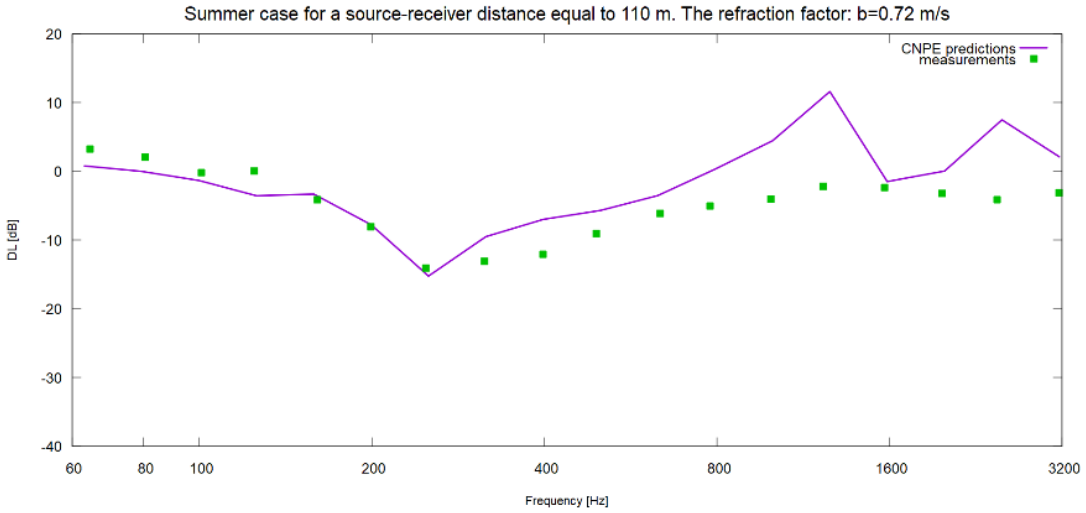

3.28: The Sound Pressure Level Attenuation, calculated from the CNPE model for the summer case. The source-receiver distance is equal to 110 m and the wind direction is downwind.

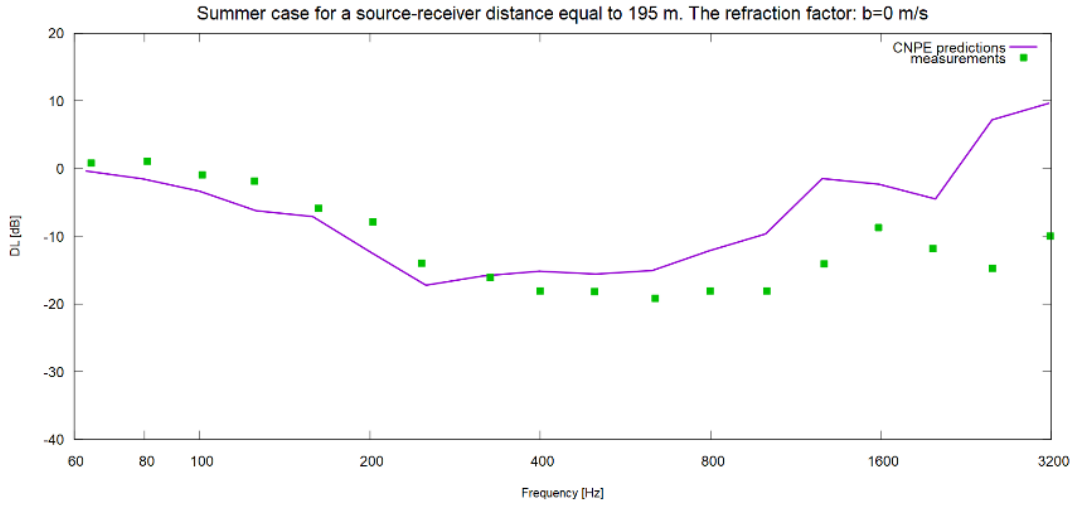

3.29: The Sound Pressure Level Attenuation, calculated from the CNPE model for the summer case. The source-receiver distance is equal to 195 m and the wind speed is equal to zero.

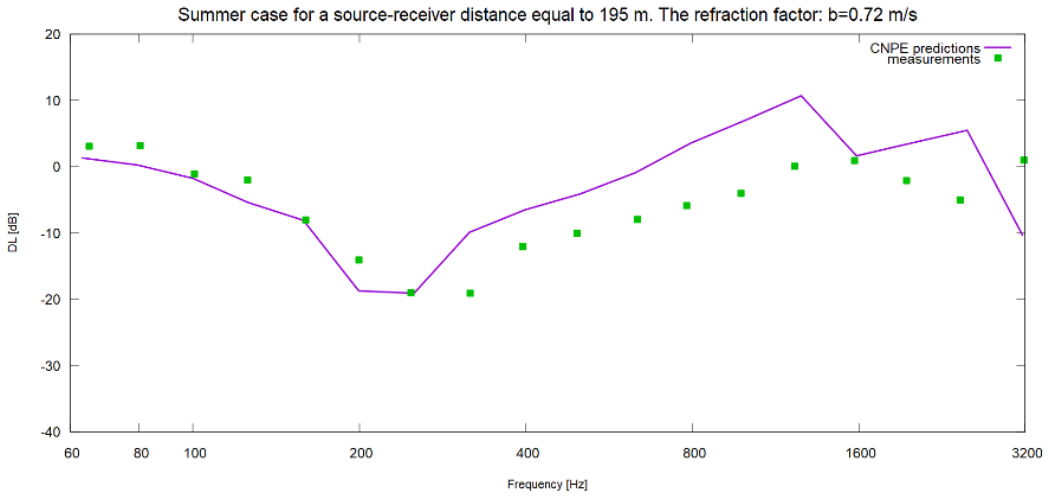

3.30: The Sound Pressure Level Attenuation, calculated from the CNPE model for the summer case. The source-receiver distance is equal to 195 m and the wind direction is downwind.

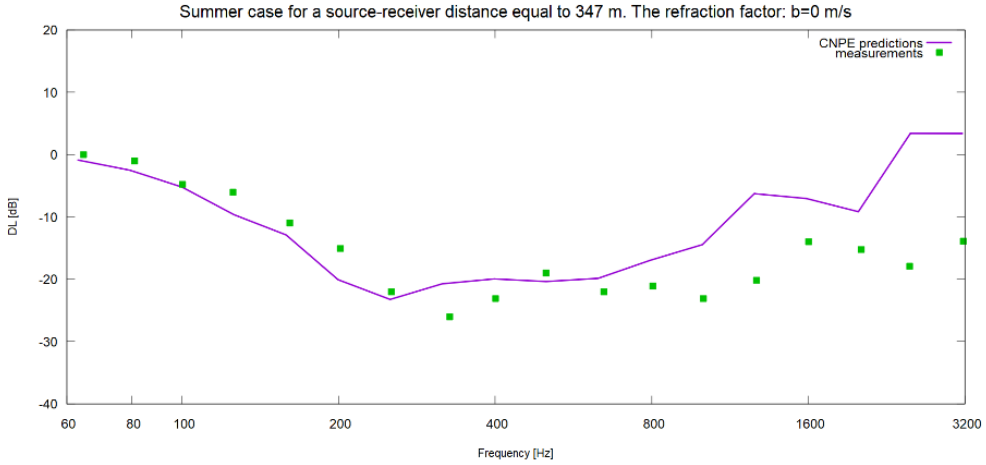

3.31: The Sound Pressure Level Attenuation, calculated from the CNPE model for the summer case. The source-receiver distance is equal to 347 m and the wind speed is equal to zero.

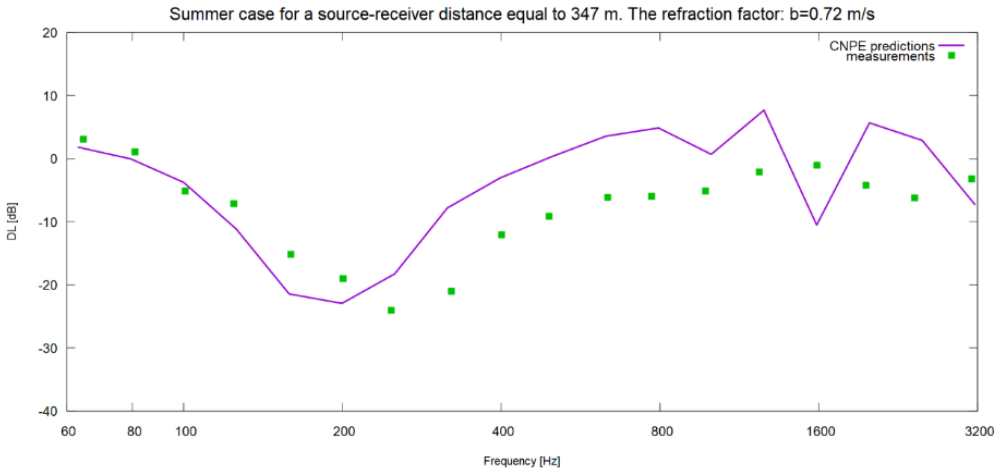

3.32: The Sound Pressure Level Attenuation, calculated from the CNPE model for the summer case. The source-receiver distance is equal to 347 m and the wind direction is downwind.

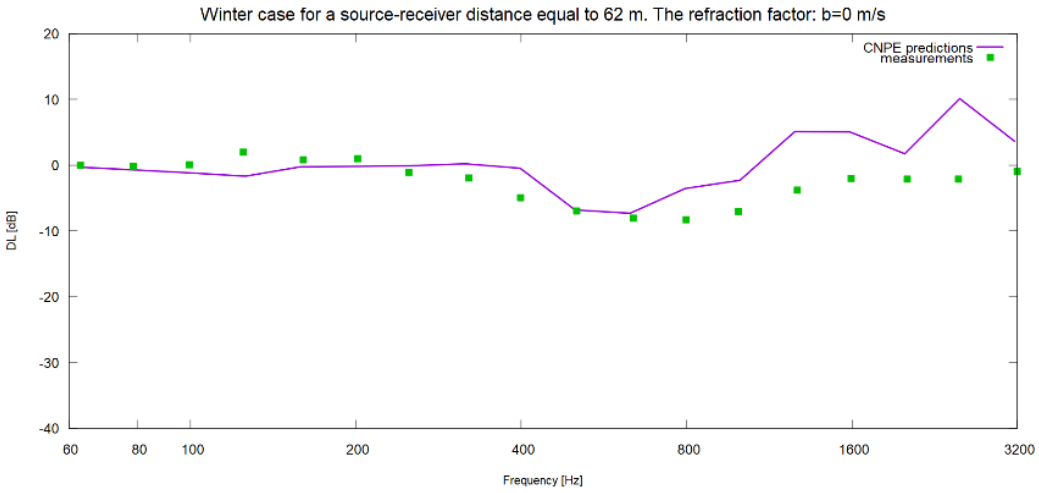

3.33: The Sound Pressure Level Attenuation, calculated from the CNPE model for the winter case. The source-receiver distance is equal to 62 m and the wind speed is equal to zero.

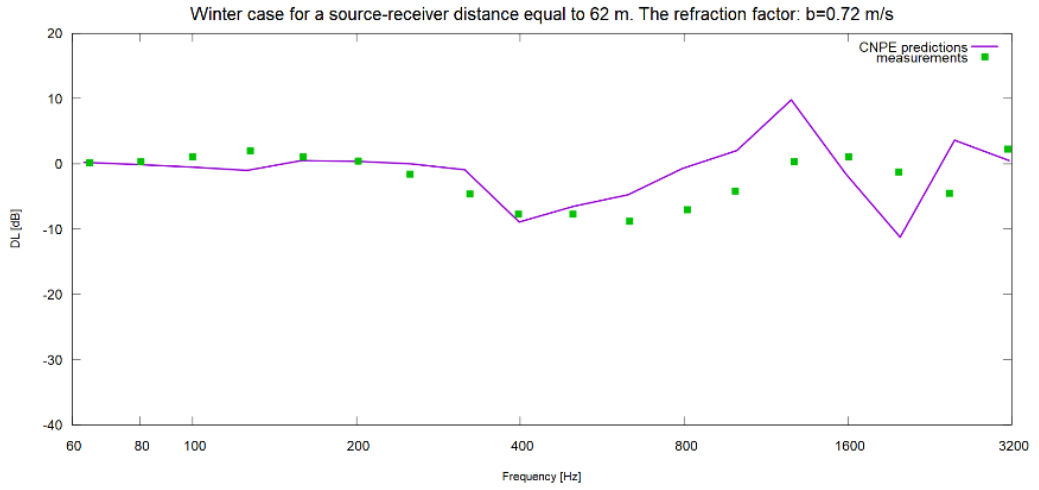

3.34: The Sound Pressure Level Attenuation, calculated from the CNPE model for the winter case. The source-receiver distance is equal to 62 m and the wind direction is downwind.

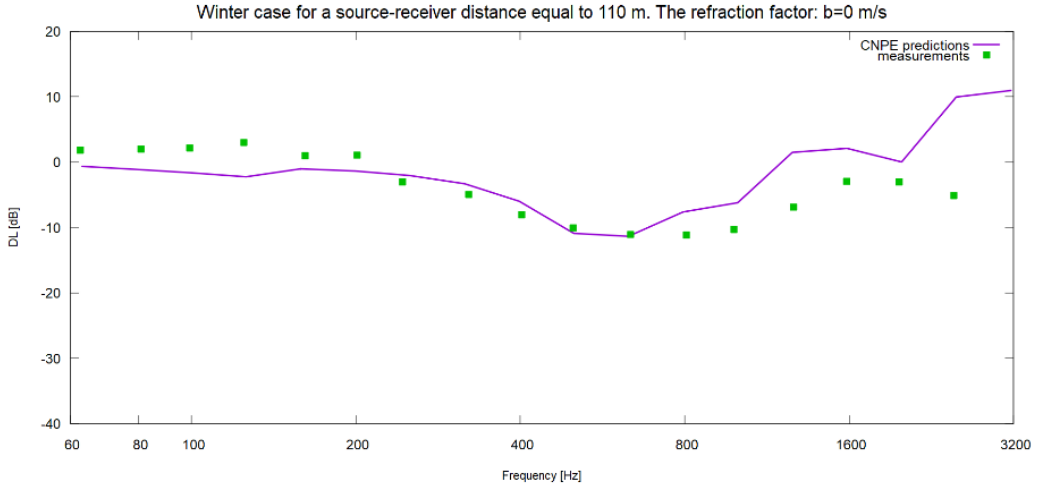

3.35: The Sound Pressure Level Attenuation, calculated from the CNPE model for the winter case. The source-receiver distance is equal to 110 m and the wind speed is equal to zero.

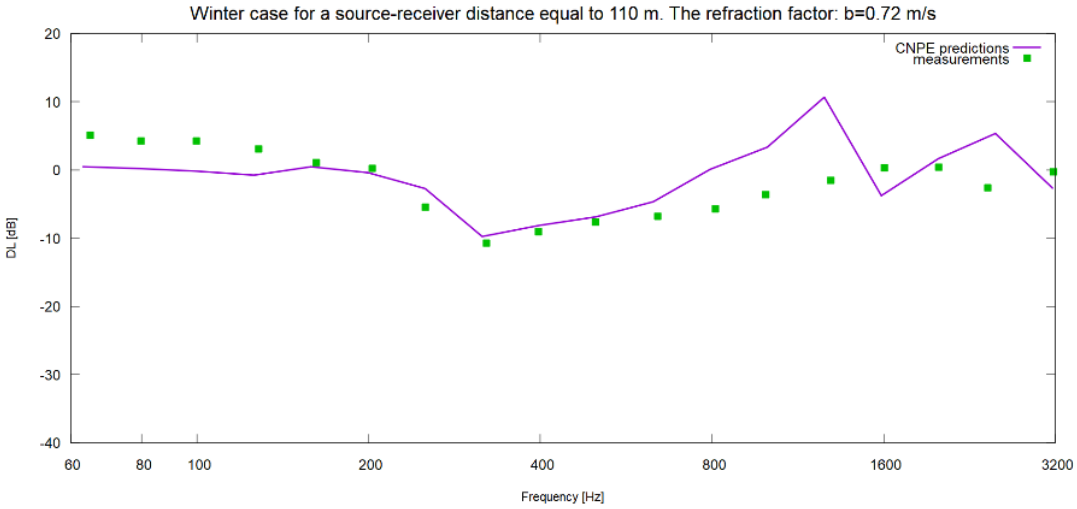

3.36: The Sound Pressure Level Attenuation, calculated from the CNPE model for the winter case. The source-receiver distance is equal to 110 m and the wind direction is downwind.

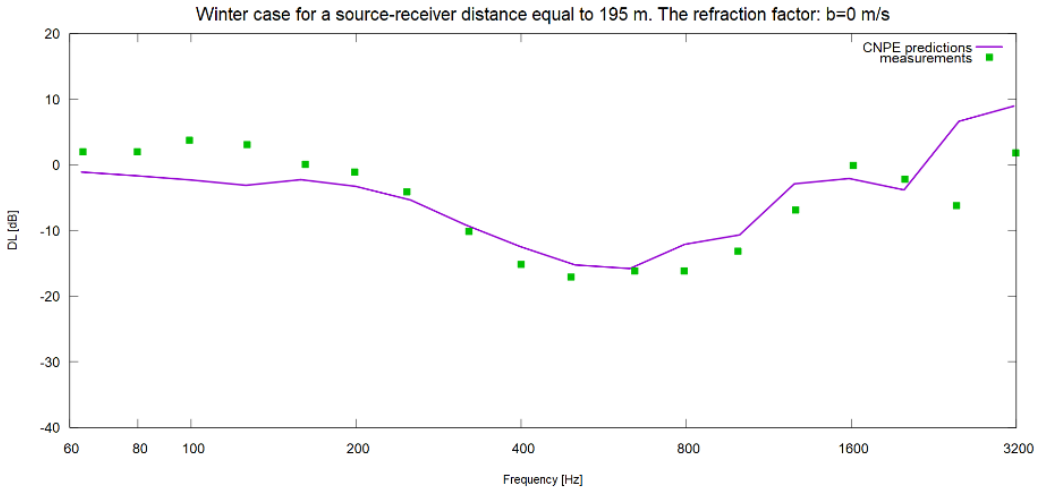

3.37: The Sound Pressure Level Attenuation, calculated from the CNPE model for the winter case. The source-receiver distance is equal to 195 m and the wind speed is equal to zero.

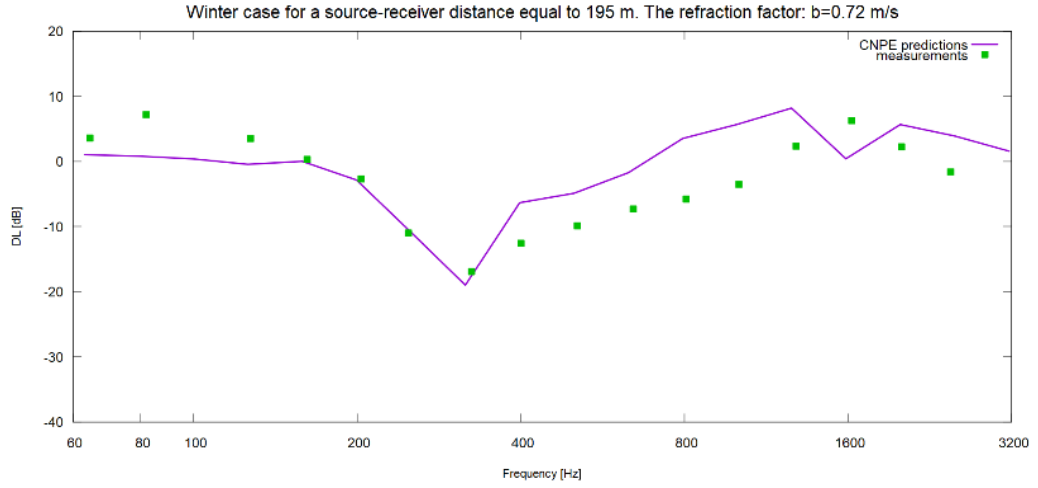

3.38: The Sound Pressure Level Attenuation, calculated from the CNPE model for the winter case. The source-receiver distance is equal to 195 m and the wind direction is downwind.

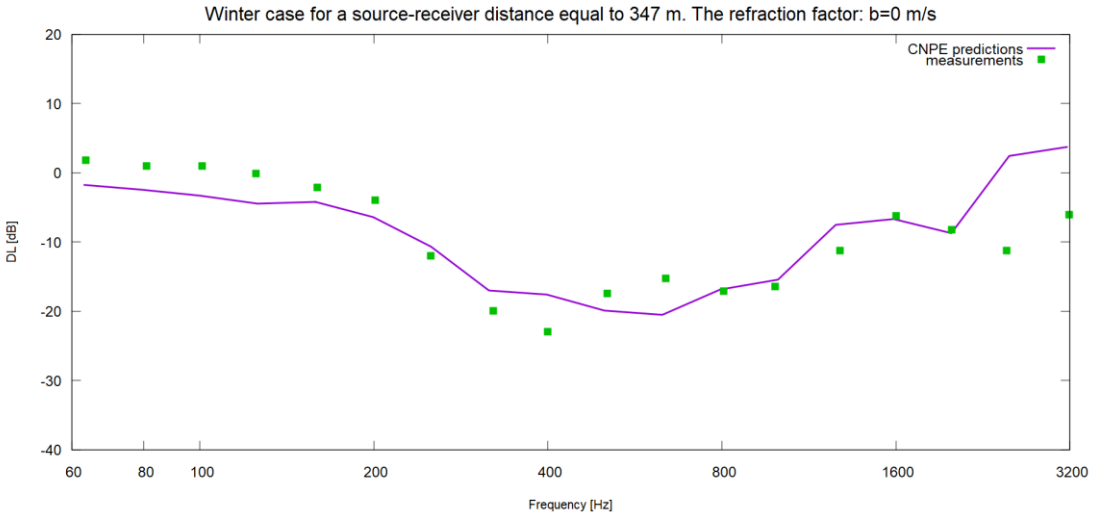

3.39: The Sound Pressure Level Attenuation, calculated from the CNPE model for the winter case. The source-receiver distance is equal to 347 m and the wind speed is equal to zero.

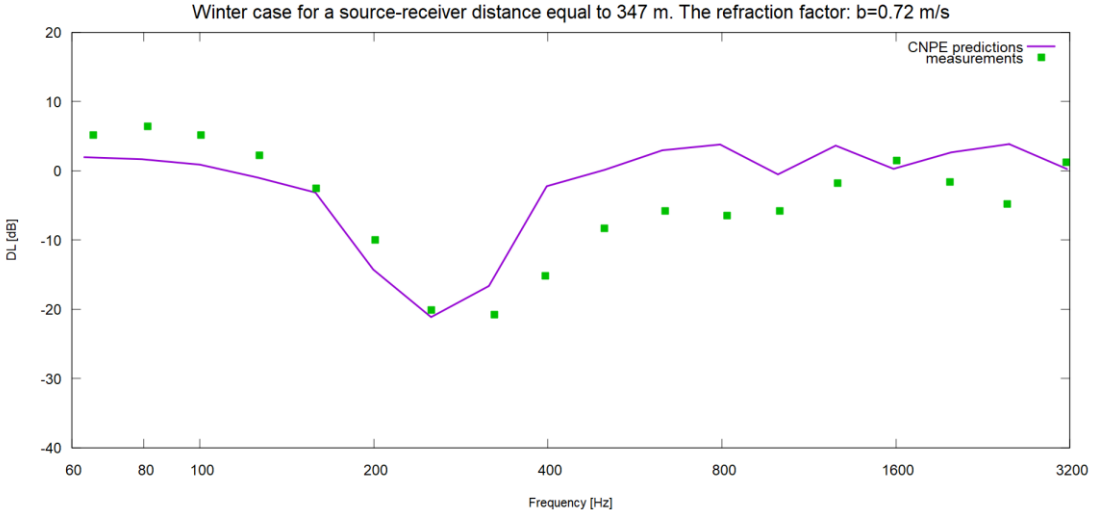

3.40: The Sound Pressure Level Attenuation, calculated from the CNPE model for the winter case. The source-receiver distance is equal to 347 m and the wind direction is downwind.

3.2. Application on the prediction of wind turbine noise immission

The general agreement, achieved between the CNPE model results and the experimental data and theoretical predictions in Sec.3.1., qualifies the code as well-developed and reliable. Therefore, it can be trusted to simulate realistic wind turbine noise propagation cases, which was the aim of this study in the first place. This section is dedicated to the comparison of model results with in-situ measurements of the sound pressure levels produced by actual wind turbines.

i. The Tammhausen experiment

In the framework of the "Noise Immission from Wind Turbines" (JOR3-CT95-0065) project, Osten and Klug [48] conducted a series of measurements in Tammhausen of Lower Saxony, in order to estimate the noise emitted by a MONOPTEROS 50- type wind turbine. For this, the "Excess Attenuation" was calculated, a quantity that represents the sound pressure level attenuation, compared to unbounded spherical propagation.

The sound pressure level of a point, distanced about one wind turbine diameter away from the source, called "emission point", is defined as:

$$SPL_e=L_W-10\cdot\log\left(4\cdot\pi\cdot r_e^2\right), \tag{3.12}$$

with L_W being the sound power level of the source and r_e the source-emission point distance (See Fig.3.41). It is important to point out here that a pure spherical propagation was assumed for the emission point, ignoring the ground and air effects.

Similarly, the sound pressure level of a point distanced far away from the source, called "immission point", is defined as:

$$SPL_i=L_W-10\cdot\log\left(4\cdot\pi\cdot r_i^2\right)-A_{e,i}, \tag{3.13}$$

with r_i being the source-immission point distance (See Fig.3.41) and $A_{e,i}$ the excess attenuation.

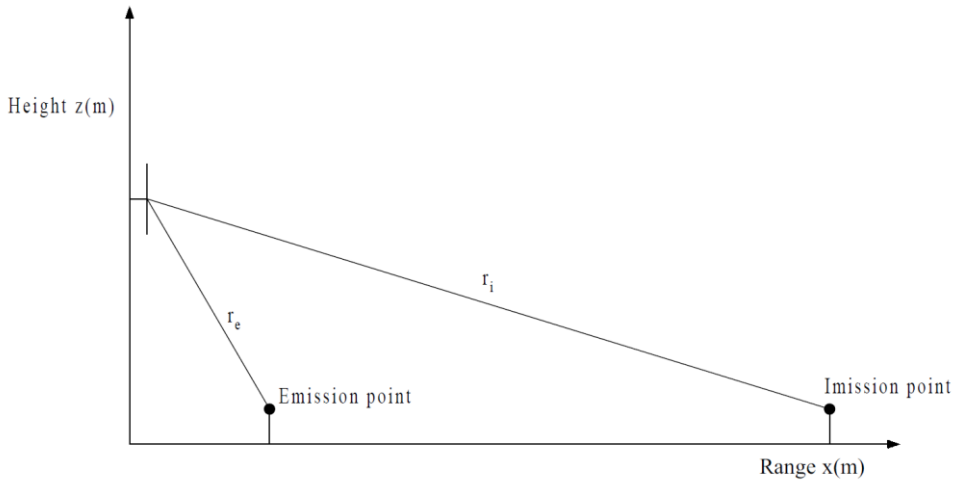

Fig.3.41: The emission and immission points with relation to the source.

A relationship for the excess attenuation can be attained by subtracting **(3.13)** from **(3.12)**:

$$A_{e,i}=SPL_e-SPL_i-20\cdot\log\left(\frac{r_i}{r_e}\right), \tag{3.14}$$

Equation **(3.14)** can be written as:

$$A_{e,i}=(SPL_e-SPL_0)-(SPL_i-SPL_0)-20\cdot\log\left(\frac{r_i}{r_e}\right)\overset{eq.(3.3)}{\Longrightarrow}A_{e,i}=\Delta L_e-\Delta L_i-20\cdot\log\left(\frac{r_i}{r_e}\right) \quad \textbf{(3.15)}$$

In eq. **(3.15)**, SPL_0 is the sound pressure level of a free field of radial distance around the source equal to 1 m. However, any sound pressure level could be used as a reference, since it will, eventually, be eliminated.

For the calculation of the excess attenuation, the following parameter values were applied:

- Source position: $(r_s, z_s) = (0, 60)$ [m]
- Emission point position: $(r_e, z_e) = (80, 0)$ [m]
- Immission point position: $(r_i, z_i) = (445, 1.5)$ or $(533, 1.5)$ [m]
- Absorbing layer thickness: $50\cdot\lambda = 50\cdot\frac{c_0}{f}$
- Flow resistivity: $\sigma=3\cdot10^5$ Rayl mks
- Roughness length: $z_0=0.02$ m
- Absolute temperature: T=282,65 K
- Relative humidity: $r_h=84\%$
- Reference speed of sound: $c_0=337.684$ m/s
- Ground impedance, Z, from eq. **(2.46)** of Delany and Bazley
- Frequency range of calculations: [160, 5000] Hz

The wind speed was calculated in the same fashion as in the Rock Springs experiment, using wind speed measurements from five different heights above the ground, along with temperature measurements from two different heights above the ground. Pressure and relative humidity were measured as well and were taken into account in the calculation of the atmospheric absorption coefficient, α(f) [See eq. **(2.51)**].

Two important points, considering the calculations on the emission point are the following:

- A closer look to the above parameter values informs the reader that the emission point is placed on the ground surface. Therefore, the boundary condition, expressed by eq. **(2.45)** was used exclusively for the calculation of the complex pressure in that particular point. Placing the receiver on the ground also means that the ground effect losses are non-existent, leaving only the spherical spreading and atmospheric absorption losses to affect the sound pressure level.
  The excess attenuation calculated by the CNPE model against a frequency range is shown in Figures 3.42 and 3.43 for a source- immission point distance of 445 and 533 m respectively. A good agreement can be observed between the measurements and the results.

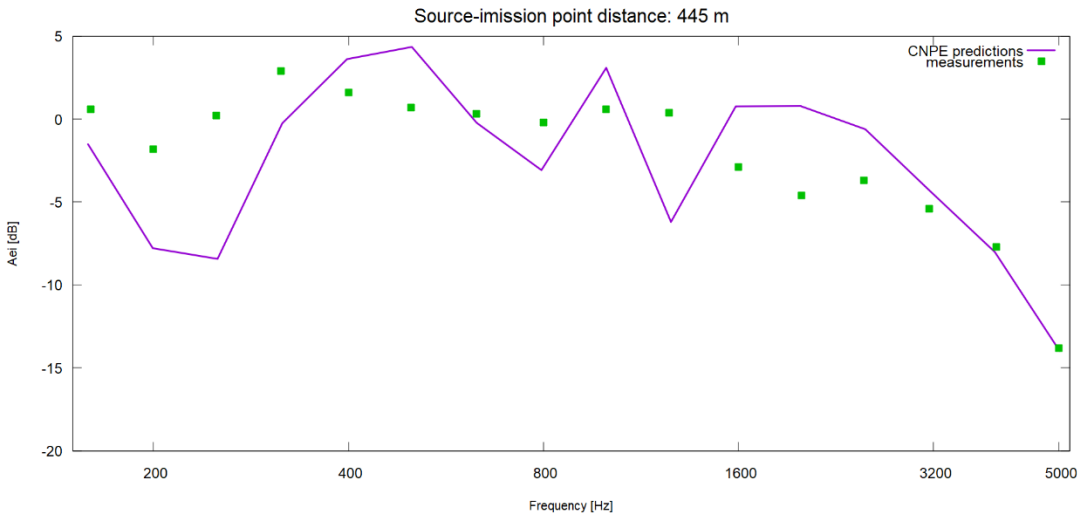

3.42: Comparison of the excess attenuation values, predicted by the CNPE model with the on-site measurements for the case of a source-immission point distance equal to 445 m.

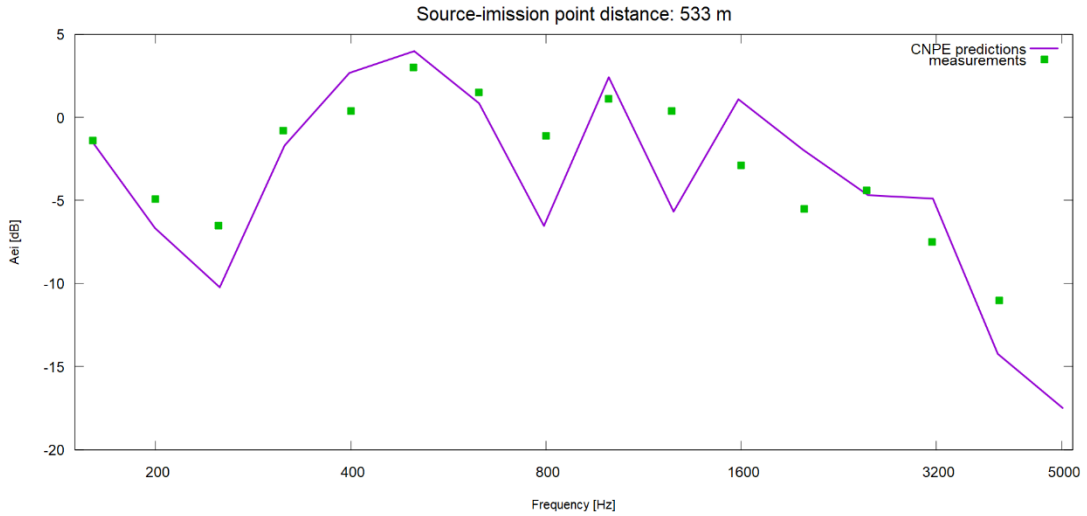

3.43: Comparison of the excess attenuation values, predicted by the CNPE model with the on-site measurements for the case of a source-immission point distance equal to 533 m.

- Although, in theory, the ground effects can be ignored in the SPL calculation of the emission point, Fig. 3.44 shows that the value of the flow resistivity affects significantly the CNPE predictions. This is a result of the fact that the acoustic pressure on the ground is calculated from the boundary condition in eq. **(2.45)**, where the σ-dependent normalized ground impedance, Z, is involved.
  For the code simulations, the flow resistivity of the emission point was given the value of 0 Rayl mks, so as to be in agreement with the experiments, during which the emission point receivers were placed on a board, made of an absorbing material, in order to cancel any interaction with the ground [48]. This elimination of the ground effects was modelled by setting σ=0 Rayl mks.

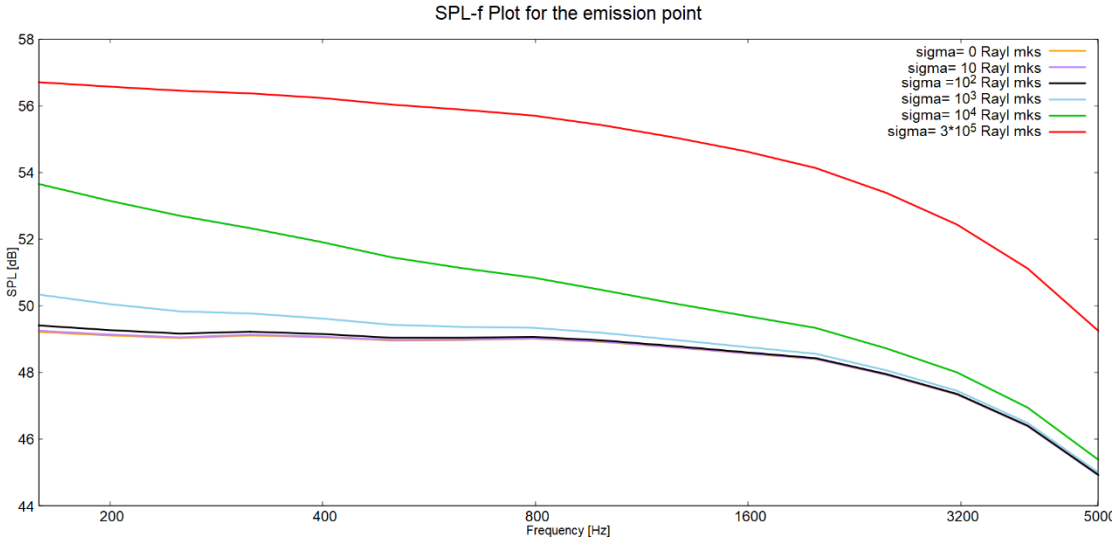

Fig.3.44: The effect of flow resistivity on the SPL of the emission point.

ii. The Lyse experiment

During the experiment in Lyse, Sweden, a series of measurements was conducted around an NWP 400-type wind turbine. For the evaluation of the sound pressure levels in this area, the quantity of excess attenuation was used, in the same manner as in the Tammhausen experiment (See Sec.3.2.i).

The following parameter values were assumed:

- Source position: $(r_s, z_s) = (0, 40)$ [m]
- Roughness length: z_0=0.001 m
- Absorbing layer thickness: $50 \cdot \lambda = 50 \cdot \frac{c_0}{f}$
- Frequency range of calculations: [40, 5000] Hz
- Ground impedance, Z, from eq. **(2.46)** of Delany and Bazley
- Wind speed profile, calculated using wind speed and temperature measurements, in the manner described in Sec.3.1.ii.

Four combinations of emission and immission point positions were examined. This study focuses on cases 3 and 4, defined by the conditions shown on Table 3.2.

Case	Position (r, z) [m]	Flow Resistivity, σ [Rayl mks]	Absolute Temperature [K]	Relative Humidity [%]	Reference Speed of Sound [m/s]	Wind direction-propagation path angle, θ_w [°]
Emission Point 3	(0, 85)	0	283.15	70	341	9
Immission Point 3	(1.35, 350)	10^6	288.15	80	341	9
Emission Point 4	(0, 85)	0	283.15	70	340	7
Immission Point 4	(1.6, 250)	$5 \cdot 10^5$	288.15	80	340	7

Table 3.2: Data from the measurements around the emission and immission points of cases 3 and 4.

It has to be mentioned here that for both Cases 3 and 4 the value of 10^5 was originally given to the emission point flow resistivity; however, in this study, σ was assumed equal to zero (See Table 3.2) for the same reasons, described in Sec.3.2.1.

The results of the excess attenuation predictions of the CNPE model are compared with the actual on-site measurements in Figures 3.45 and 3.46 for Case 3 and Case 4 respectively. A general agreement between predictions and measurements can be observed for Case 3. In Case 4, predictions do reproduce the maximum dip at the frequency of 250 Hz, yet they do not follow neither the dip at the low frequency of 63 Hz nor the increase of excess attenuation at the high frequencies. This, however, was expected; the resulting curve is similar to the one of Case 3, since there is no qualitative difference between the two cases.

The dip at the frequency of 63 Hz is probably the result of local air and ground effects or of erroneous measurements. Indeed, one should not forget that the measurements were taken for both the emission and the immission points; collecting the wrong data from either point, would affect significantly the final excess attenuation values. The steep decline of $A_{e,i}$ in the high frequency range cannot represent an actual propagation case, under the given conditions; for a source-receiver distance of 250 m (Case 4), a higher value of excess

attenuation is expected, due to the increased atmospheric absorption losses, as is reasonably reproduced by the model (See Fig. 3.46).

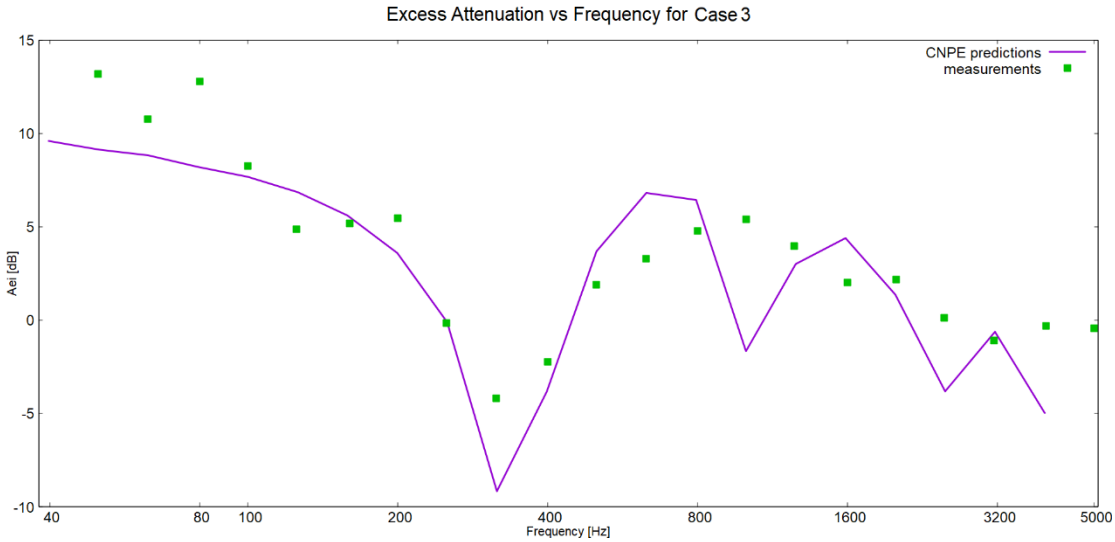

Fig.3.45: Comparison between the CNPE model predictions and the actual measurements of the excess attenuation for the emission-immission point combination No.3.

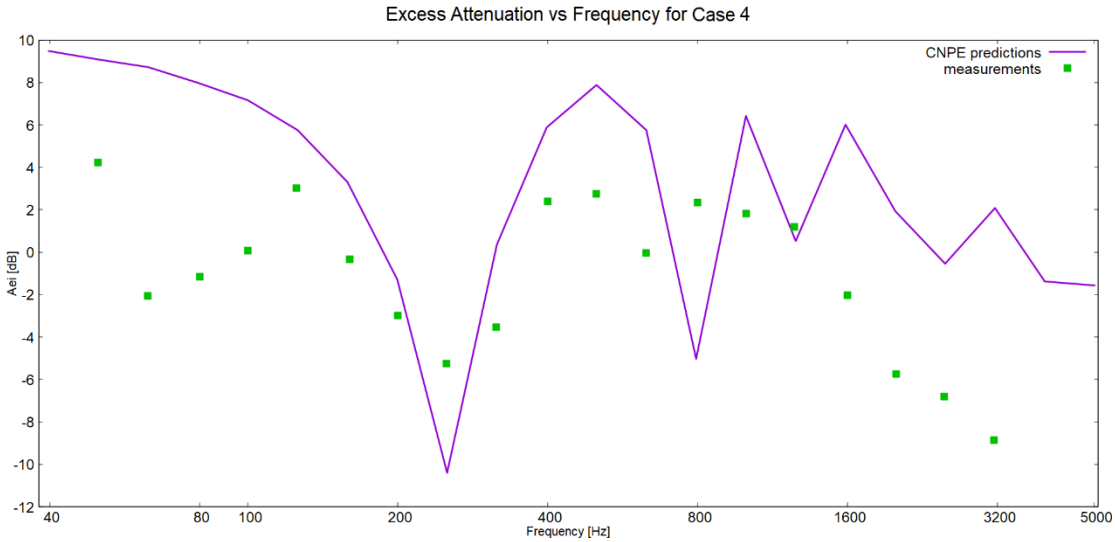

Fig.3.46: Comparison between the CNPE model predictions and the actual measurements of the excess attenuation for the emission-immission point combination No.4.

iii. The Høvsøre experiment

Søndergaard and Plovsing [50, 51] measured the sound propagation over a flat terrain, at Høvsøre, Denmark, from a loudspeaker, placed at wind turbine's height. The cases reproduced by the CNPE model had the following parameter values:

- Source position: $(r_s, z_s) = (0,50)$ [m]
- Receiver height, r_r: 2 or 5 m
- Receiver range, z_r: 500 m
- Absorbing layer thickness: $50 \cdot \lambda = 50 \cdot \frac{c_0}{f}$
- Roughness length: z_0=0.05 m
- Relative humidity: r_h=81% (typical for the month of July, when the experiments were conducted, for the nearby area of Fjaltring, [52])
- Reference speed of sound: c_0=334.83 m/s
- Frequency range of calculations: [100, 2500] Hz
- Ground impedance, Z, from eq. **(2.46)** of Delany and Bazley

An average absolute temperature was considered for the calculations that resulted from Fig. 3. 47, in which the difference between the predicted absolute temperature at any height z and the respective at a height of 2 m above the ground is plotted against the z-range. The absolute temperature at z=2 m was acquired from eq. **(3.16)** of the effective sound speed:

$$c(z)=u(z)\cdot \cos(\theta_w) +20.05\cdot\sqrt{T(z)+273.15}, \qquad \textbf{(3.16)}$$

where u(z) is the wind speed profile, plotted in Fig. 3.48 and θ_w is the angle between the wind direction and the direction of propagation, equal to 0° here, since the case of downwind propagation is examined. The effective sound speed profile is depicted in Fig.3.49 and is calculated by the logarithmic-linear equation **(3.17)**:

$$c(z)=A\cdot \ln\left(1+\frac{z}{0.05}\right)+B\cdot z+ C, \qquad \textbf{(3.17)}$$

with A=0.6082, B=0.0173 and C=334.754 being constants, calculated from the measured values of the effective sound speed.

For the height of z=2 m, Figures 3.48 and 3.49 read respectively: u(2m)=2.43 m/s and c(2m)=337.08 m/s. Therefore, from eq. **(3.16)**, it follows that T(2 m)= 278.58 K. Taking, now, the values of Fig.3.47 into account, one calculates the average absolute temperature, T=278.178 K.

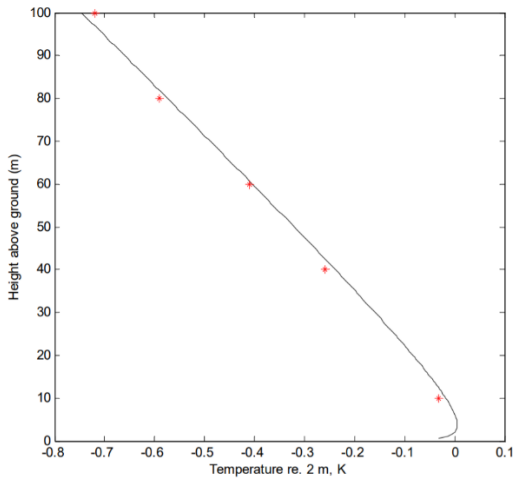

Fig.3.47: The absolute temperature profile, measured and predicted by Søndergaard and Plovsing [50].

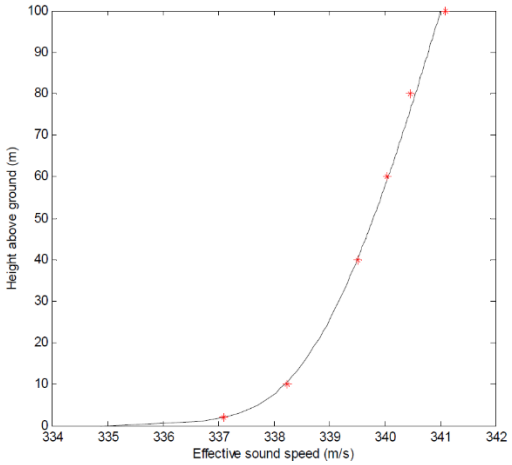

Fig.3.48: The effective sound speed profile, measured and predicted by Søndergaard and Plovsing [50].

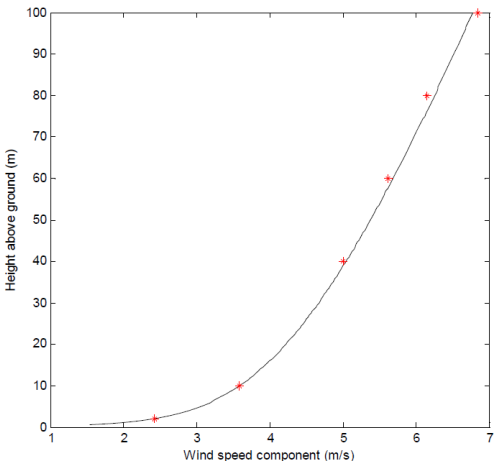

Fig.3.49: The wind speed profile, measured and predicted by Søndergaard and Plovsing [50].

The quantity used here for the evaluation of sound propagation is called "Excess Propagation Effect" and it contains the propagation effect of ground and air absorption. The excess propagation effect is given by eq. **(3.18)**:

$$\Delta L = SPL - SPL_0, \tag{3.18}$$

with SPL being the measured 1/3-octave band sound pressure level, calculated from eq. **(3.19)**:

$$SPL = 10 \cdot \log\left(\frac{\frac{1}{2}\cdot|p_c|^2}{p_{ref}^2}\right), \tag{3.19}$$

where $\frac{1}{2}\cdot|p_c|^2$ is the squared sound pressure, averaged over an integral number of harmonic periods and $p_{ref}=2\cdot10^{-5}$ Pa, is the reference pressure.

In eq. **(3.18)** SPL_0 is the free field sound pressure level, determined by eq. **(3.20)**:

$$SPL_0 = SPL_{1.29\,m} - 20\log\left(\frac{d}{d_0}\right) \tag{3.20}$$

In eq. **(3.20)**, d is the distance from the loudspeaker to the receiver and $d_0=1.29$ m is the distance from the acoustical center of the loudspeaker to the "1 m" microphone, including the correction for the near field effect.

The quantity $SPL_{1.29\,m}$ is the sound pressure level at a distance of d_0 from the source. For short distances from the source, the pressure field, calculated by the developed CNPE model was proven to almost coincide with the one that would result from the complex free field pressure, $p_{free} = \frac{e^{i\cdot k\cdot r}}{r}$, [See eq. **(2.65)**]. Therefore, in this case, $SPL_{1.29\,m}$ can be calculated from eq. **(3.19)**, with $|p_c| = \left|\frac{e^{i\cdot k\cdot 1.29}}{1.29}\right| = \frac{1}{1.29} = 0.775$ dB.

Since there was no reference regarding the value of the flow resistivity, σ, it was studied here as a variable within the range of [10^5, 10^6] Rayl mks for the calculation of the excess propagation effect, as can be seen from Figures 3.50 and 3.51. For the first case ($z_r=2$ m), the value of $\sigma=10^5$ Rayl mks seems to produce the closest results to the measurements, whereas for the second ($z_r=5$ m), the value of $\sigma=5\cdot10^5$ Rayl mks seems the more adequate.

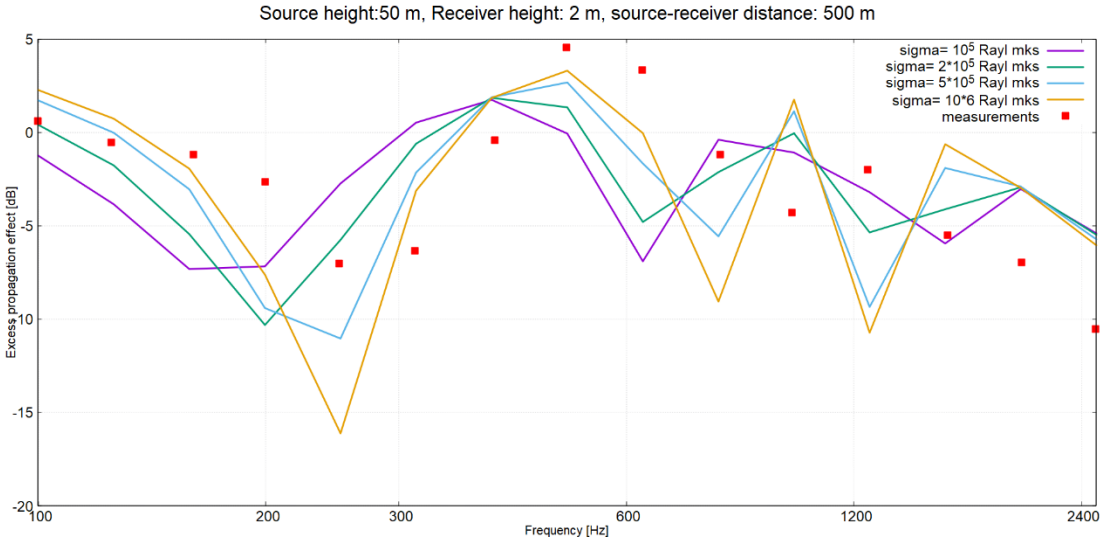

Fig.3.50: The CNPE model results against a frequency range for a varying flow resistivity, compared to the on-site measurements for a receiver height of 2 m. Downwind conditions were considered.

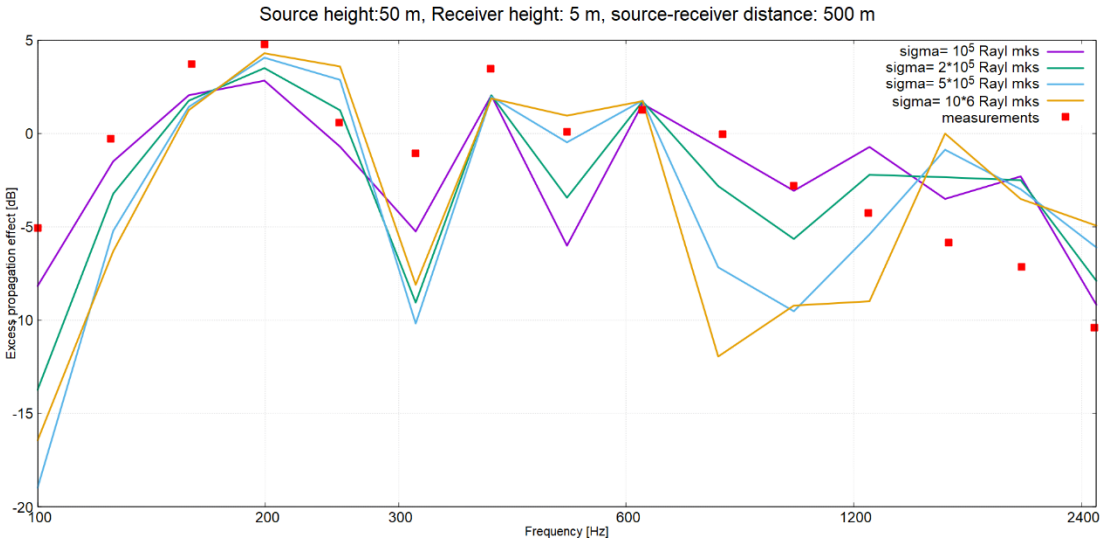

Fig.3.51: The CNPE model results against a frequency range for a varying flow resistivity, compared to the on-site measurements for a receiver height of 2 m. Downwind conditions were considered.

4. Conclusions and future work

4.1 Conclusions

The aim of the present study was the development of a model, able to predict sound propagation in the atmospheric environment and its application on real-life wind turbine cases. The code was programmed to solve the Parabolic Equation, using adequate ground surface and top layer boundary conditions. The sound source was modeled as a Gaussian starting field. Atmospheric, ground and spherical spreading losses were taken into account. A top surface absorbing layer was added for the elimination of the effect of sound wave reflections on the predicted sound pressure levels.

An investigation of the grid density independence of the solution proved the grid spacing value of $\Delta r=\Delta z= \lambda/10$ to be a cost-efficient choice, that causes no instabilities during calculations and yields reliable results for the source-receiver distances of interest. Tests on various combinations of absorbing layer thickness and top grid surface height showed that accurate results can be collected, even for a relatively low upper boundary (of approximately twice the height of a wind turbine), as long as the absorbing layer has a thickness of at least $50\cdot\lambda$, a value adopted in the rest of the calculations. This investigation was conducted for both low (1.36 m A.G.L) and high (20.4 m A.G.L) receiver heights, leading to the same conclusions.

The developed CNPE model was first validated against the analytical solution and the predictions of the FFP and the Ray Theory methods for typical benchmark cases. Next, the predictions of the model were compared against systematic experimental data for downwind and upwind propagation conditions. In the case of downwind conditions, which favor noise propagation, hence are the ones of interest for the wind turbine applications, the model results were in fair agreement with the on-site measurements. In the case of upwind propagation conditions, all methods overestimate the attenuation losses at long distances. However, the CNPE predictions present less deviation from the measurements, suggesting that the parabolic equation method is more suitable for the simulation of such cases.

Having been validated, the code was applied to the estimation of wind turbine noise propagation, producing results fairly close to the measurements. During these simulations, it became evident that the ground and wind speed modeling affect the results significantly. Especially during measurements on the emission point, when the receiver is usually placed on a board of an absorbing material, the value of zero for the flow resistivity proved to provide better results since it better simulates the material of the board. A detailed knowledge of both ground material and the atmospheric conditions (temperature, humidity, wind speed) is, therefore, essential, since it provides the means for a more accurate simulation of noise immission from wind turbines.

4.2 Suggestions for future work

Future research on sound propagation could focus on the amelioration of the CNPE model or the development of other, more complex numerical methods. More specifically, the effects of atmospheric turbulence and the irregularity of the terrain could be added to the simulation. Thus, the CNPE model could be applied to a relatively smooth terrain, as long as the crosswind effect and the back-scattering are not significant, ensuring that the assumptions of the axisymmetric and parabolic approximation remain valid. Following another direction, a model for solving the three-dimensional Green Function Parabolic Equation (GFPE) or a more advanced CFD method of solving the Linearized Euler Equations (LEEs) could be developed. In this respect, technical knowledge, acquired from the development of the CNPE model, such as the addition of a top surface absorbing layer, the choice of a Gaussian starting field and the boundary conditions could be proven useful.

References

[1] GWEC global wind report 2021.

[2] Jan Olof Helldin, Jens Jung, Wiebke Neumann, Mattias Olsson, Anna Skarin, Fredrik Widemo: "The impacts of wind power on terrestrial mammals. A synthesis". Report 6510. August 2012. Ch.4.

[3] S. Wagner, R. Bareiss, G. Guidati: "Wind Turbine Noise". 1996. Par.1.3.

[4] Vermont Department of Health: "Wind Turbine Noise & Human Health: A Review of the Scientific Literature". May 2017. Pg.2.

[5] Jens M. Hovem: "Ray Trace Modeling of Underwater Sound Propagation". August 2013. Ch.23.

[6] Jensen, F. B., Kuperman, W. A., Porter, M. B., & Schmidt, H.: "Computational Ocean Acoustics" (2011).

[7] Alain Berry & G. A. Daigle: "Controlled experiments of the diffraction of sound by a curved surface". J. Acoust. Soc. Am., Vol. 83, No. 6, June 1988.

[8] A. L'Espérance, P. Herzog, G. A. Daigle & J. R. Nicolas: "Heuristic Model for Outdoor Sound Propagation Based on an Extension of the Geometrical Ray Theory in the Case of a Linear Sound Speed Profile". Applied Acoustics 37 (1992) 111-139.

[9] Takayuki Hidaka, Kenji Kageyama, and Sadahiro Masuda: "Sound propagation in the rest atmosphere with linear sound velocity profile". J. Acoust. Soc. Jpn. (E) 6, 2 (1985).

[10] Richard Raspet, Andr L'Espérance & Gilles A. Daigle: "The effect of realistic ground impedance on the accuracy of ray tracing". J. Acoust. Soc. Am., Vol. 97, No. 1, January 1995.

[11] Brekhovskikh: "Waves in layered media". Academic Press, New York, 1980. Sec.45.3.

[12] John M. Prospathopoulos & Spyros G. Voutsinas: "Application of a Ray Theory Model to

the Prediction of Noise Emissions from Isolated Wind Turbines and Wind Parks". Wind Energ. 2007. 10:103–119.

[13] John M. Prospathopoulos & Spyros G. Voutsinas: "Noise Propagation Issues in Wind

Energy Applications". Journal of Solar Energy Engineering. May 2005, Vol. 127.

[14] John M. Prospathopoulos & Spyros G. Voutsinas: "Determination of equivalent sound speed profiles for ray tracing in near-ground sound propagation". J. Acoust. Soc. Am., Vol. 122, No. 3, September 2007.

[15] Erik M. Salomons: "Computational atmospheric acoustics". Springer Science and Business Media Dordrecht, 2001.

[16] Kenneth E. Gilbert & Michael J. White: "Application of the parabolic equation to sound propagation in a refracting atmosphere". J. Acoust. Soc. Am., Vol 85, No. 2, pg. 630-637. February 1989.

[17] Kenneth E. Gilbert & Michael J. White: "Application of the Parabolic Equation to the Outdoor Propagation of Sound". Applied Acoustics 27 (1989) 227-238.

[18] X. Di and K.E. Gilbert: "Wave propagation in a 3-D turbulent atmosphere: horizontal coherence," Proc. Eighth Symposium on Long-Range Sound Propagation, The Pennsylvania State University, Pennsylvania, 169-180 (1998).

[19] Emre Barlas, Wei Jun Zhu, Wen Zhong Shen, Kaya O. Dag, and Patrick Moriarty: "Consistent modelling of wind turbine noise propagation from source to receiver". The Journal of the Acoustical Society of America 142, 3297 (2017).

[20] Emre Barlas , Wei Jun Zhu, Wen Zhong Shen, Mark Kelly, Søren Juhl Andersen: "Effects of wind turbine wake on atmospheric sound propagation". Applied Acoustics 122 (2017), pg. 51–61.

[21] Seongkyu Lee, Dongjai Lee & Saskia Honhoff: "Prediction of far-field wind turbine noise propagation with parabolic equation". The Journal of the Acoustical Society of America 140, 767 (2016); doi: 10.1121/1.4958996.

[22] C.L. Pekeris, Theory of propagation of explosive sound in shallow water. Geol. Soc. Am. Mem. Vol. 27 (1948).

[23] W.S. Jardetzky, Period equation for an N-layered halfspace and some related questions. Tech. Rep. Seism. No. 29. Lamont-Doherty Geological Observatory, Columbia University, New York, 1953.

[24] W.M. Ewing, W.S. Jardetzky, F. Press, Elastic Waves in Layered Media (McGraw-Hill, New York, 1957).

[25] R. Raspet, S.W. Lee, E. Kuester and D.C. Chang, W.F. Richards, R. Gilbert and N. Bong: "A fast-field program for sound propagation in a layered atmosphere above an impedance ground". J. Acoust. Soc. Am., Vol. 77, No.2, February 1985.

[26] S.W. Lee and N. Bong, W.F. Richards and Richard Raspet: "Impedance formulation of the fast field program for acoustic wave propagation in the atmosphere". J. Acoust. Soc. Am., Vol. 79, No.3, March 1986.

[27] D. Keith Wilson: "Sound field computations in a stratified, moving medium". J. Acoust. Soc. Am., Vol. 94, No.1, July 1993.

[28] Y. L. Li, Michael J. White and S. J. Franke: "New fast field programs for anisotropic sound propagation through an atmosphere with a wind velocity profile". J. Acoust. Soc. Am., Vol. 95, No.2, February 1994.

[29] L. Nijs & C. P.A. Waponaar "The influence of wind and temperature gradients on sound

propagation, calculated with the two-way wave equation". J. Acoust. Soc. Am., Vol. 87, No.5, May 1990.

[30] Henrik Schmidt & Gerard Tango: "Efficient global matrix approach to the computation of

synthetic seismograms". Geophys J. R. urfr. SOC. (1986) 84,331-3-59.

[31] Richard Raspet, Gordon Baird and Wenliang Wu: "Normal mode solution for low-frequency sound propagation in a downward refracting atmosphere above a complex impedance plane". J. Acoust. Soc. Am., Vol. 91, No.3, May 1992.

[32] Stephen E. Keith, Gilles A. Daigle and Michael R. Stinson: "Wind turbine low frequency and infrasound propagation and sound pressure level calculations at dwellings". J. Acoust. Soc. Am., Vol. 144, No.2, August 2018.

[33] I.M. Prospathopoulos, K.A. Belibassakis & S.G.Voutsinas: "NUMERICAL MODELLING OF PROPAGATION OF NOISE EMITTED FROM WIND PARKS". In Proceedings of the European Wind Energy Conference 1999, Petersen EL, Jensen PH, Rave K, Helm P, Ehmann H. (eds). James & James: London, 1999; 97–100.

[34] Xiaofeng Sun and Xiaoyu Wang: "Fundamentals of Aeroacoustics with Applications to Aeropropulsion Systems", Shanghai Jiao Tong University Press Aerospace Series 2021, Pages 135-205. Ch.4: "Linearized unsteady aerodynamics for aeroacoustic applications", par. 4.3.1.

[35] Viswanathan, K., and Sankar, L. N., "Toward the Direct Calculation of Noise: Fluid/Acoustic Coupled Simulation" AIAA Journal, Vol. 33, No. 12, 1995, pp. 2271–2279.

[36] Timothy Van Renterghem: "Efficient outdoor sound propagation modeling with the finite-difference time-domain (FDTD) method: a review". International Journal of Aeroacoustics, Vol. 13, No. 5 & 6, 2014, pg. 385 – 404.

[37] Timothy Van Renterghem, Erik M. Salomons, Dick Botteldooren: "Efficient FDTD-PE Model for Sound Propagation in Situations with Complex Obstacles and Wind Profiles". ACTA ACUSTICA UNITED WITH ACUSTICA, Vol. 91, (2005), 671–679.

[38] Shiguang Liu and Jin Liu: "Outdoor Sound Propagation Based on Adaptive FDTD-PE".2020 IEEE Conference on Virtual Reality and 3D User Interfaces (VR).

[39] Reinhard Blumrich and Dietrich Heimann: "A linearized Eulerian sound propagation model for studies of complex meteorological effects". J. Acoust. Soc. Am., Vol. 112, No. 2, August 2002.

[40] K.E. Gilbert and X. Di, "A fast Green's function method for one-way sound propagation in the atmosphere," J. Acoust. Soc. Am. 94, 2343- 2352 (1993).

[41] John M. Prospathopoulos and Spyros G. Voutsinas: "Noise Propagation Issues in Wind Energy Applications". Journal of Solar Energy Engineering, May 2005, Vol. 127, pg. 234-241.

[42] M. E. Delany and E. N. Bazley: "ACOUSTICAL PROPERTIES OF FIBROUS ABSORBENT MATERIALS". Applied Acoustics (3) (1970). Elsevier Publishing Company Ltd, England. Printed in Great Britain.

[43] Sultanian, B.: "Gas Turbines: Internal Flow Systems Modeling". Sec.E: "Thomas Algorithm for Solving a Tridiagonal System of Linear Algebraic Equations", Par. E1 (Cambridge Aerospace Series, pp. 337-338). Cambridge University Press. doi:10.1017/9781316755686.012. 2018.

[44] Attenborough et al.: "Benchmark cases for outdoor sound propagation models". J. Acoust. Soc. Am., Vol. 97, No.1, January 1995.

[45] A. L'Espérance et al.: "Sound Propagation in the Atmospheric Surface Layer: Comparison of Experiment with FFP Predictions". Applied Acoustics 40 (1993) 325-346.

[46] Panofsky H. A. and J. A. Dutton, 1984: "Atmospheric turbulence. Models and methods for engineering applications". New York: Wiley-Interscience.

[47] P. H. Parkin and W. E. Scholes: "The horizontal propagation of sound from a jet engine close to the ground, at Radlett".1964. J. Sound Fib. I, 1-13.

[48] Osten, T., and Klug, H., 1997, "Noise Propagation Measurements in the Vicinity of Wind Turbines,". Report No. AS 971214, Deutsches Windenergie, Wilhelmshaven, Germany.

[49] Fegeant O. Noise propagation around wind turbines: second set of measurements at the Lyse wind power station. KTH technical report 1997:6, Dept of Building Sciences, KTH Division of Building Technology, ISSN 0349-6562, Stockholm, 1997.

[50] Bo Søndergaard and Birger Plovsing: Report: "SPO-07 F&U Project No 7389/ Noise and Energy Optimization of Wind Farms/ Validation of the Nord2000 propagation model for use on wind turbine noise". AV 1236/09, Project no.:A580521.

[51] Bo Søndergaard and Birger Plovsing: "Wind turbine noise propagation: Comparison of measurements and predictions by a method based on geometrical ray theory". Noise Control Eng. J. 59 (1), Jan-Feb 2011.

[52] https://www.weather-atlas.com/